Predicting structural behaviour of pressure vessels using large scale meta-modelling applied to plug type heat exchanger header boxes

by

Wilhelm André Beyers

Dissertation presented for the degree of Doctor of Philosophy in the Faculty of Engineering at Stellenbosch University

Supervisor: Prof. G. Venter

December 2017

Declaration

By submitting this dissertation electronically, I declare that the entirety of the work contained therein is my own, original work, that I am the sole author thereof (save to the extent explicitly otherwise stated), that reproduction and publication thereof by Stellenbosch University will not infringe any third party rights and that I have not previously in its entirety or in part submitted it for obtaining any qualification.

Date: December 2017

Abstract

Predicting structural behaviour of pressure vessels using large scale meta-modelling applied to plug type heat exchanger header boxes

W. A. Beyers

Department of Mechanical and Mechatronic Engineering,
University of Stellenbosch,
Private Bag X1, Matieland 7602, South Africa.

Dissertation: PhD (Mech)

December 2017

Plug type header boxes are predominantly designed according to the American Society of Mechanical Engineers' Boiler and Pressure Vessel Code. The two design methods most often employed from this code are 'Design by Rule' from Division 1 of the code and 'Design by Analysis' from Division 2 Part 5. While 'Design by Rule' is relatively simple to implement and relies only on a set of hand calculations which produce immediate results, it is widely known to be conservative. 'Design by Analysis' on the other hand relies on finite element analysis, which yields more accurate results, but is more costly and time consuming.

In this study a new analysis tool was developed in the form of a meta-model, based on finite element results, which predicts the structural behaviour for various plug type header boxes. The purpose of this tool is to provide a designer with real time predictions of the stresses in a header box, as is the case for 'Design by Rule', but with accuracy similar to a finite element analysis.

In order to achieve this goal, a software tool set was developed which automates the process of setting up, simulating and post-processing the results of a finite element analysis. This made it possible to generate numerical results on a large scale, in order to collect enough data to train an accurate meta-model.

Using this tool set, a number of less complex meta-models were initially created to test the approach and refine the procedure employed. These tests were

performed using very large training sets and showed that high (4^{th} and 5^{th}) order response surface models were required to accurately approximate the structural behaviour of plug type header boxes. The challenges associated with fitting such high order response surfaces were addressed and these models were systematically scaled up in complexity until the final meta-model was constructed.

The final meta-model achieved the desired goals of providing accurate stress results, in real time, for a plug type header box. Designers can use this model to search for optimal designs and identify what the structural effects are when individual header box dimensions are changed. This will allow for detailed insight to be gained of the structural behaviour of plug type header boxes in a manner which has been unavailable in the past. The implications of such knowledge will expand the field of knowledge surrounding these pressure vessels and open the door for the implementation of possible new design methods in the future.

Uittreksel

Voorspelling van strukturele gedrag van drukvate deur middel van grootskaalse meta-modellering toegepas op prop-tipe hitteruiler spruitstukhouers

('Predicting structural behaviour of pressure vessels using large scale meta-modelling applied to plug type heat exchanger header boxes')

W. A. Beyers

Departement Meganiese en Megatroniese Ingenieurswese,
Universiteit van Stellenbosch,
Privaatsak X1, Matieland 7602, Suid Afrika.

Proefskrif: PhD (Meg)

Desember 2017

Prop-tipe spruitstukhouers word oorwegend ontwerp volgens die 'American Society of Mechanical Engineers' se Ketel en Drukvat Kode. Die twee ontwerpmetodes van hierdie kode wat meer gereeld gebruik word is 'Ontwerp deurmiddel van Reëls' uit Afdeling 1 van die kode en 'Ontwerp deur middel van Analise' uit Afdeling 2 Deel 5 van die kode. Terwyl 'Ontwerp deur middel van Reëls' relatief eenvoudig is om te implementeer en slegs staatmaak op 'n stel handberekeninge wat onmiddelike resultate verskaf, is dit algemeen bekend om konserwatief te wees. 'Ontwerp deur middel van Analise' maak egter staat op eindige element analise, wat akkurate resultate verskaf, maar duurder is en meer tyd in beslag neem.

In hierdie studie word daar 'n nuwe analise nutsmiddel ontwerp in die vorm van 'n meta-model, wat gebaseer is op eindige element analise resultate, wat die strukturele gedrag van verskeie prop-tipe spruitstukhouers kan voorspel. Die doel van hierdie nutsmiddel is om 'n ontwerper te voorsien van onmiddelike voorspellings van die spannings in 'n spruitstukhouer, soos die geval is met 'Ontwerp deur middel van Reëls', maar met akkuraatheid gelykstaande aan eindige element analise.

Om hierdie doel te bereik is ‘n stel sagteware ontwerp wat die proses outomatiseer waardeur eindige element analise opstelling, analisering en resultaatverwerking plaasvind. Hierdie sagteware maak dit moontlik om grootskaalse numeriese resultate te genereer, om sodoende genoeg data te versamel waarmee akkurate meta-modelle ingestel kan word.

Met behulp van hierdie sagteware is ‘n aantal minder komplekse metamodelle aanvanklik geskep om die beplande benadering te toets en die prosedures wat gebruik word te verfyn. Hierdie toetse is uitgevoer met baie groot opleidingstelle en het gewys dat hoë (4^{de} en 5^{de}) orde polinoom-oppervlakmodelle benodig word om die stukturele gedrag van prop-tipe spruitstukhouers akkuraat te benader. Die uitdagings wat verband hou met die passing van sulke hoë orde polinoom-oppervlakke is aangespreek en hierdie modelle is stelselmatig in verhouding vergroot in kompleksiteit totdat die finale meta-model gebou is.

Die finale meta-model het die gewenste doelwit om onmiddelike, akkurate spanningsresultate vir ‘n prop-tipe spruitstukhouer te voorspel bereik. Ontwerpers kan hierdie model gebruik om te soek vir optimale ontwerpe en om te bepaal wat die strukturele effek is wanneer individuele spruitstukhouer mates verander word. Dit sal toelaat dat gedetailleerde insig opgebou kan word oor die strukturele gedrag van prop-tipe spruitstukhouers op ‘n manier wat nie in die verlede beskikbaar was nie. Die implikasie van sulke kennis sal die veld van kennis rondom hierdie drukvate verbreed en die deur oopmaak vir die toepassing van moonlike nuwe ontwerpmetodes in die toekoms.

Dedication

To my Lord and Saviour Jesus Christ. Thank you for this opportunity and for carrying me through!

Acknowledgements

I would like to express my overflowing gratitude to the following people and organisations:

- My supervisor, Prof Gerhard Venter, for sharing your time, wisdom and experience and guiding me through this process while allowing me to be my unconventional self.

- My family for your constant prayer and support. Words cannot say enough!

- Prof Johan van der Spuy for your advice about so much more than just the work.

- Mike Coats for sharing your bottomless supply of knowledge and insight with me.

- Bennie Buys for sharing your technical experience and understanding with me.

- Kelvion Thermal Solutions for providing the funding for this research.

Contents

List of Figures

List of Tables

Chapter 1

Introduction

1.1 Air-cooled heat exchangers

Heat exchangers are widely used in power generation, petrochemical and other industries where large scale process cooling is required to increase plant efficiency and facilitate chemical processes. In areas with scarce water resources, air-cooled heat exchangers are preferred for process cooling. Compared to shell and tube heat exchangers and wet cooling towers, they provide a more sustainable solution because they do not need any auxiliary water supply.

An air-cooled heat exchanger removes heat from a process fluid by forcing ambient air over a finned tube bundle, through which the fluid is flowing. The fluid is under pressure, but the intensity may vary depending on chemical or other processes it is undergoing. The typical layout of a forced draft air-cooled heat exchanger is shown in Figure 1.1. Hot process fluid is pumped through an inlet header, which splits it into the finned tube bundle. As the fluid moves along the tubes, cool ambient air is blown over the tube bundle by a fan to accelerate the exchange of heat between the air and the fluid in the tubes. Finally the fluid is collected in an outlet header and leaves the heat exchanger.

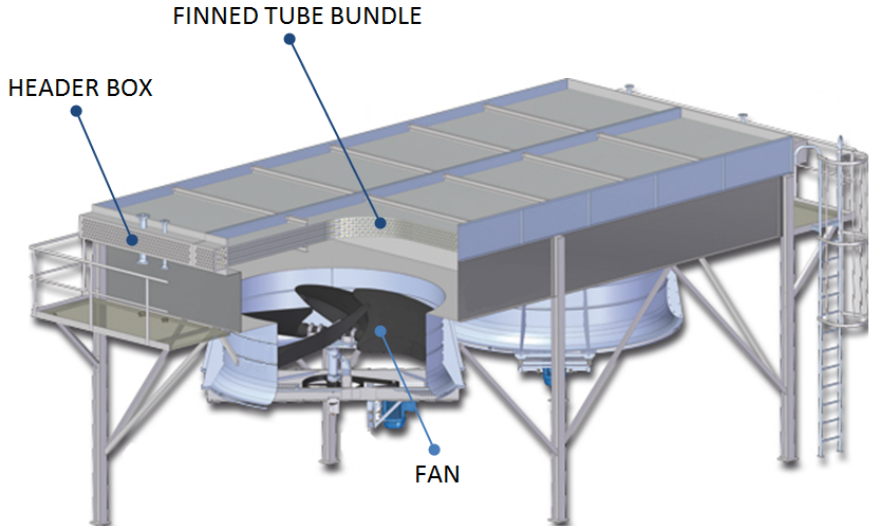

Figure 1.1: Typical forced draft air-cooled heat exchangers configuration, adapted from (Tubetech GmbH)

1.2 Header boxes

A heat exchanger header box is a pressurised manifold. Figure 1.2 shows a typical plug type header box. Process fluid flows through an inlet header box, entering through the nozzles and exiting split into individual tubes attached to the tube sheet. The reverse path is followed for an outlet header box. The two most commonly used header box types are the removable cover and plug type header boxes, whose designs will be discussed next.

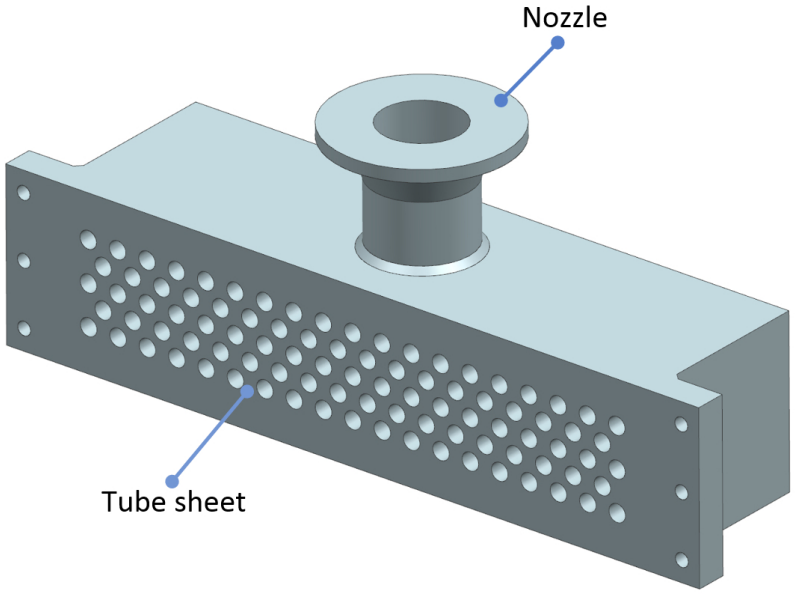

Figure 1.2: Plug type header box

Cover type header box

Figure 1.3 shows two cover type header box configurations. Both configurations consist of five plates welded together to form an open box, to which a free standing cover is bolted by means of a flanged connection, to complete the box. The only difference is that the tube sheet is part of the welded section in the first case and part of the cover in the other.

A benefit of the cover type design is that an entire side of the box can be removed for easy inspection and cleaning of the header box and the heat exchanger tubes. The drawback of this design is that the flanged connection, which forms part of the header box's structure, limits the strength of the joints concerned. This in turn limits the maximum operational pressure of these header boxes to 3 MPa, as recommended in Table A.2 of the American Petroleum Institute (API) standard (API, 2013).

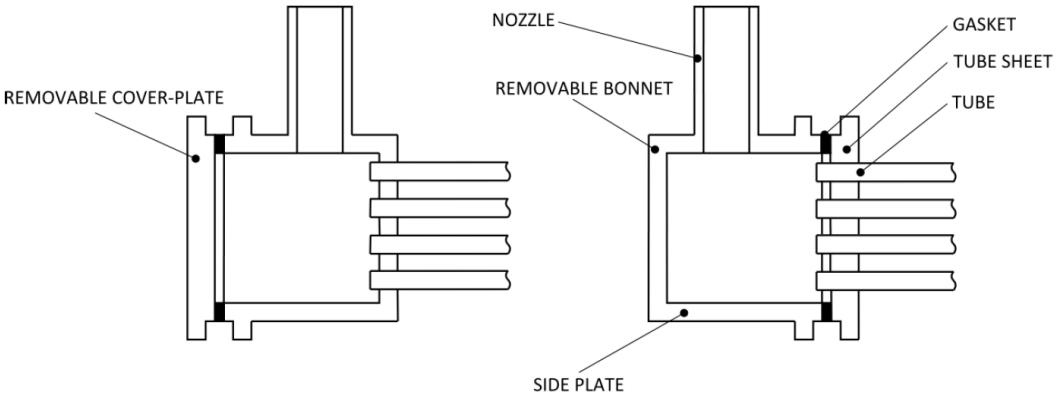

Figure 1.3: Cover type header box, adapted from (Prinsloo, 2011)

Plug type header box

Figure 1.4 shows the schematic layout of a plug type header box. The header box consists of six metal plates welded together on all sides to form an enclosed box. For every tube sheet hole, there is a corresponding hole in the opposite sheet, known as the plug sheet. During operation these holes are sealed by a plug screwed into each hole. During maintenance, the plugs can easily be removed to gain access to the insides of the header box and the finned tubes for inspection and cleaning purposes.

A benefit of a plug type header box is that, because it is welded on all sides, the structure is more rigid than a cover type header box, allowing it to operate at pressure ranges exceeding 3 MPa (API, 2013). A disadvantage of plug type header boxes is that the size of the plug holes complicate inspection

and cleaning of the header box. This is a particular problem if the process fluid in question causes fouling in the system, as cleaning the inside of the box itself is difficult.

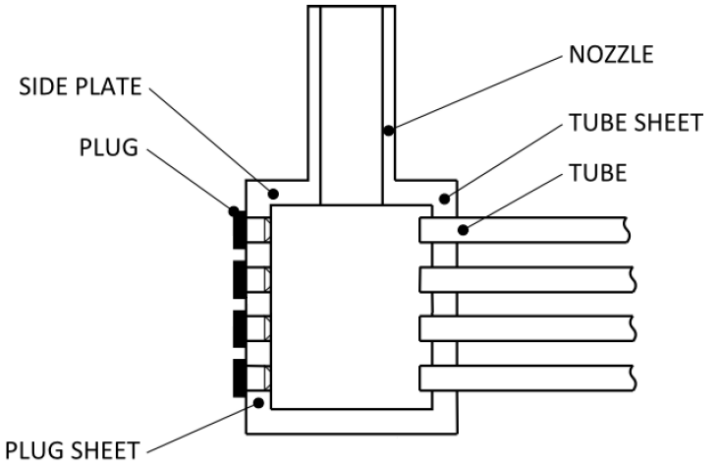

Figure 1.4: Plug type header box, adapted from (Prinsloo, 2011)

1.3 Motivation

Plug type header boxes are predominantly designed according to ASME Section VIII Division 1 (ASME, 2015) (further details will be provided in Section 2.1). This part of the ASME code was originally written to be a set of simple hand equations that can be used to design various rectangular pressure vessels. The simplified nature of this approach led to a set of design rules with a conservative basis and high safety margins (Becker, 2013).

The benefits of this design method are that it has proven to be reliable over many years and that it gives a designer immediate results with which to work. However, in industry, conservative and high safety margins lead to elevated manufacturing cost and unnecessary utilisation of resources.

Currently, the best way to get accurate design results is to perform a finite element (FE) analysis of a pressure vessel under consideration. This method provides the designer with considerably more detailed results, but it is costly and time consuming. While these constraints are not prohibitive they do not favour the use of FE analyses as part of an iterative design process to find optimal designs.

The aim of this study is to find a way to combine the best features of both these design methods by creating an analysis tool that will accurately predict the structural behaviour of a plug type header box in real time. This will allow the designer to study and understand the structural behaviour of these pressure vessels on a much broader scale than a case by case basis and open the door to possible new design methods in the future.

1.4 Objectives

The objective of this study is to develop a predictive tool, in the form of a meta-model based on FE results, which can provide results similar to those of a FE analysis, but in real time and at a fraction of the cost. In order to fulfil this objective, the following will be done:

1. Develop a process for testing large numbers of FE models
2. Construct initial smaller meta-models of pressure vessel components to test the feasibility and accuracy of the concept
3. Scale up the initial models to produce a full plug type header box model

1.5 Scope

For reasons elaborated upon later, the scope of this study is limited to the following:

- only single chamber un-stayed plug type header boxes will be considered
- only linear static analysis will be considered
- only linearised stresses according to ASME VIII Division 2 Part 5 will be modelled

Chapter 2

Literature review: Pressure vessel design

2.1 Design codes and standards

Most countries regulate the design and construction of pressure vessels. South African law (South African Dept of Labour, 1993) requires that any vessel operating above 50 kPa (gauge) internal pressure (South African Board of Standards, 2012) has to be designed according to a pressure vessel design code. Internationally, the most well known design code is the American Society of Mechanical Engineers' (ASME) Boiler & Pressure Vessel Code, Section VIII (ASME, 2015).

Division 1 of this ASME code provides a set of requirements to be followed for the design of a variety of pressure vessels. If all of the requirements are adhered to for a particular design, the design is deemed satisfactory and can be certified as code compliant. This method is known as 'Design by Rule'. This part of the code was written to be a set of simple equations that describes the behaviours of a wide variety of pressure vessel configurations. This simplified approach led to a set of design rules with a conservative basis and high safety margins (Becker, 2013). The requirements pertaining to the design of the body of a plug type header box may be found in Appendix 13 of this Division.

Division 2 Part 4 of the same code provides a similar set of requirements to that in Appendix 13 of Division 1, but allows for somewhat higher allowable stresses to be used, depending on the design conditions specified for a pressure vessel. Generally, this produces less conservative designs. This part of the code is, however, not used as readily as Division 1 due to the additional requirements with respect to the responsibilities of the user, designer and manufacturer, which have cost and time implications that often out weigh the benefits to be gained from obtaining a less conservative design.

Alternatively, pressure vessels may also be designed according to Part 5 of Division 2. This part provides requirements for the use of numerical modelling as a means of structural analysis, in order to design pressure vessels more accurately. Methods for analysing results are also given along with various failure criteria that need to be satisfied, in order to ensure a satisfactory design. This method is known as 'Design by Analysis'. This method is generally less conservative than the 'Design by Rule' approach, as it seeks to avoid high safety margins by allowing for a more detailed analysis of a pressure vessel's design.

In addition to design codes, pressure vessels are often designed to meet the requirements of additional standards, such as the API Standard 661 (API, 2013). Certain companies may also have their own standards that designers need to satisfy. The purpose of these standards is to provide additional guidelines pertaining to good engineering practice with regard to the design and construction of pressure vessels.

Examples of such guidelines from the API standard are provided in Figures 2.1, 2.2 and 2.3. The first is a figure showing nozzle loading orientations, accompanied by the second which is a table setting out the recommended nozzle loads which need to be taken into account when designing a header box. The third is a guide for recommended minimum header box wall thicknesses.

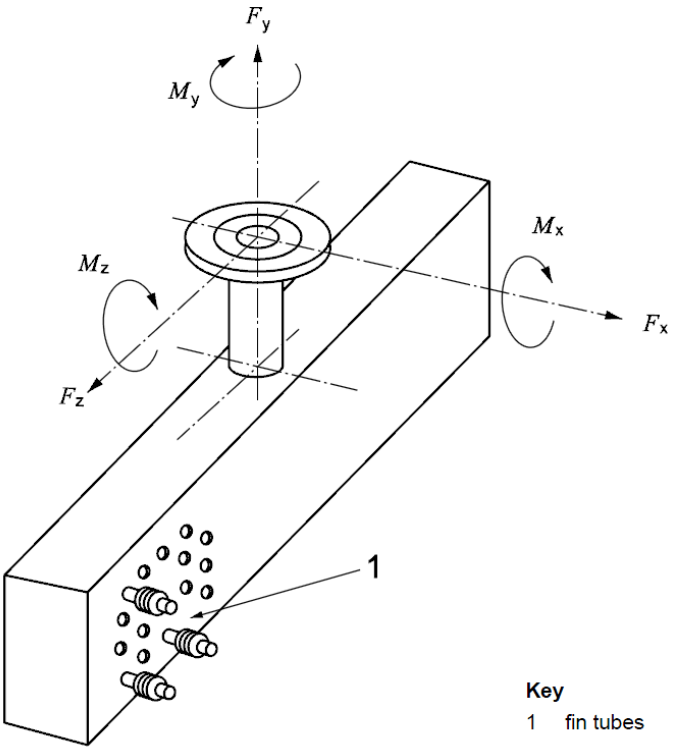

Figure 2.1: Nozzle loading orientations (API, 2013)

Table 4 — Maximum Allowable Nozzle Loads

Nozzle Size DN (NPS)	Moments N·m (ft·lbf)			Forces N (lbf)		
	M_x	M_y	M_z	F_x	F_y	F_z
40 ($1^1/_2$)	110 (80)	150 (110)	110 (80)	670 (150)	1020 (230)	670 (150)
50 (2)	150 (110)	240 (180)	150 (110)	1020 (230)	1330 (300)	1020 (230)
80 (3)	410 (300)	610 (450)	410 (300)	2000 (450)	1690 (380)	2000 (450)
100 (4)	810 (600)	1220 (900)	810 (600)	3340 (750)	2670 (600)	3340 (750)
150 (6)	2140 (1580)	3050 (2250)	1630 (1200)	4000 (900)	5030 (1130)	5030 (1130)
200 (8)	3050 (2250)	6100 (4500)	2240 (1650)	5690 (1280)	13,340 (3000)	8010 (1800)
250 (10)	4070 (3000)	6100 (4500)	2550 (1880)	6670 (1500)	13,340 (3000)	10,010 (2250)
300 (12)	5080 (3750)	6100 (4500)	3050 (2250)	8360 (1880)	13,340 (3000)	13,340 (3000)
350 (14)	6100 (4500)	7120 (5250)	3570 (2630)	10,010 (2250)	16,680 (3750)	16,680 (3750)

Figure 2.2: Nozzle loading guidelines (API, 2013)

Table 1 — Minimum Nominal Thickness of Header Components

Component	Minimum Thickness	
	Carbon or Low-alloy Steel mm (in.)	High-alloy Steel or Other Material mm (in.)
Tubesheet	19 ($^3/_4$)	16 ($^5/_8$)
Plug sheet	19 ($^3/_4$)	16 ($^5/_8$)
Top, bottom and end plates	12 ($^1/_2$)	10 ($^3/_8$)
Removable cover plates	25 (1)	22 ($^7/_8$)
Pass partition plates and stay plates	12 ($^1/_2$)	6 ($^1/_4$)

NOTE The thickness indicated for any carbon or low-alloy steel component includes a corrosion allowance of up to 3 mm ($^1/_8$ in.). The thickness indicated for any component of high-alloy steel or other material does not include a corrosion allowance. The thickness is based on an expanded tube-to-tubesheet joint with one groove.

Figure 2.3: Minimum allowable wall thickness guide (API, 2013)

2.2 ASME Division 1 design methodology

Appendix 13 of ASME VIII Division 1 provides specific requirements for the design of pressure vessels with non-circular cross-sections. Plug type header boxes fall into this category. The design approach followed in the appendix is to disregard the structural support of a pressure vessel's end plates and to determine necessary wall thicknesses of the remaining parts based only on their cross-sectional profiles. Once these have been designed, users are directed to other parts of the code to design the end plates.

To facilitate this procedure, the appendix provides a set of illustrated cross-sectional profiles, each accompanied by a set of design equations, from which the user must select the appropriate design. The equations enable the designer to calculate membrane and bending stresses at critical points in the pressure vessel's structure. These values must be compared to the failure criteria, given by Equations 2.1 and 2.2, in order to ensure that the header box design is strong enough. In these criteria, S is the material allowable stress.

$$\sigma_{membrane} \leq S \tag{2.1}$$

$$\sigma_{membrane+bending} \leq 1.5S \tag{2.2}$$

The illustrated configurations relevant to the design of plug type header boxes are shown in Figure 2.4.

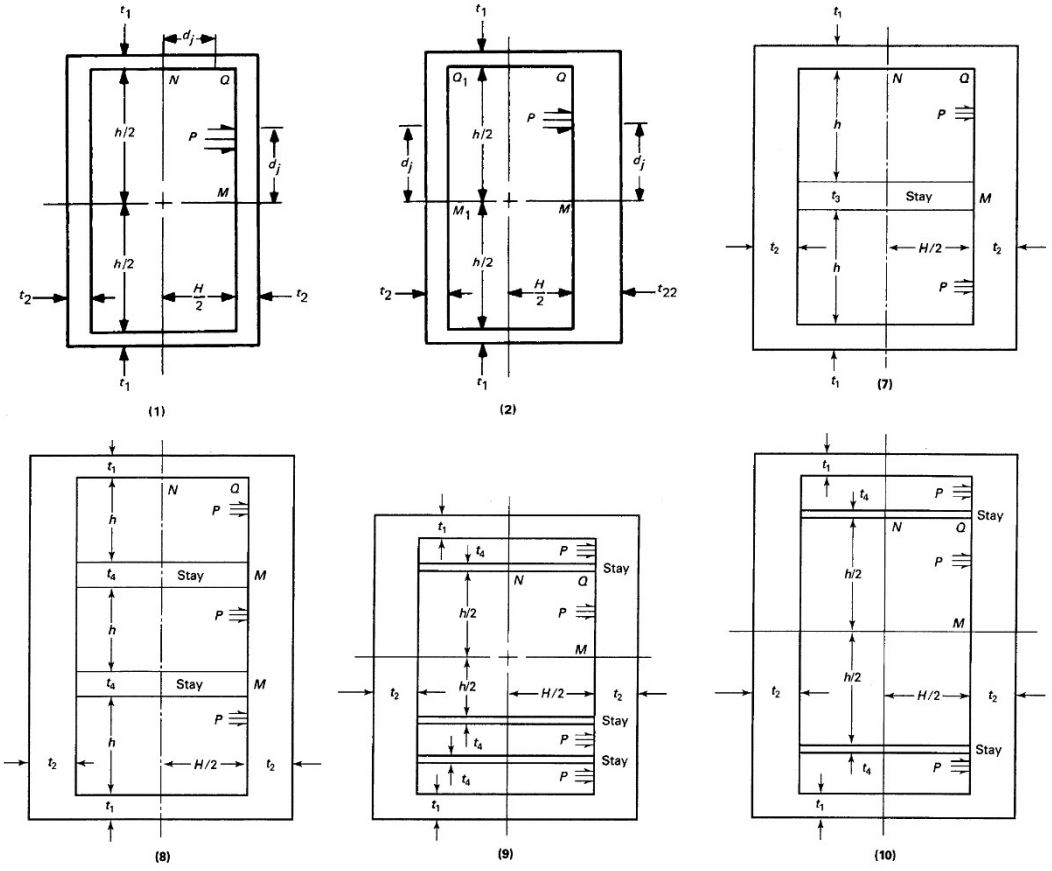

Figure 2.4: Pressure vessel configurations, adapted from (ASME, 2015)

Table 2.1 shows the equations given in the code for calculating the necessary membrane and bending stresses of a single chamber header box, where both sets of opposite sides have equal wall thickness; Configuration (1) in Figure 2.4.

Table 2.1: Single chamber vessel design formulae (ASME, 2015)

Membrane Stress	
Short side	$S_m = \frac{Ph}{2t_1}$
Long side	$S_m = \frac{PH}{2t_2}$
Bending Stress	
Centre of the short side	$S_{b_N} = \frac{Pc}{12I_1}\left(-1.5H^2 + h^2\frac{1+\alpha^2K}{1+K}\right)$
Short side joint	$S_{b_Q} = \frac{Ph^2c}{12I_1}\left(\frac{1+\alpha^2K}{1+K}\right)$
Centre of the long side	$S_{b_M} = \frac{Ph^2c}{12I_2}\left(-1.5 + \frac{1+\alpha^2K}{1+K}\right)$
Long side joint	$S_{b_Q} = \frac{Ph^2c}{12I_2}\left(\frac{1+\alpha^2K}{1+K}\right)$
Additional Equations	
Rectangular vessel parameter	$\alpha = \frac{H}{h}$
Vessel parameter	$K = \left(\frac{I_2}{I_1}\right)\alpha$
I_1 and I_2 are the moments of inertia of the respective pairs of opposite walls.	

These equations are meant for calculating the stresses in a header box with no perforations. A provision is however made that a plate ligament efficiency can be incorporated, which serves to reduce the calculated load carrying capacity of a specific wall of the vessel, to account for plates such as the plug and tube sheets which are perforated. This ligament efficiency is calculated based upon the fraction of material removed from a vessel wall relative to its original state. The allowable stress for the respective walls are then decreased by this fraction. Thus, if the ligament efficiency factor for a wall is 0.5, the calculated stresses for that wall may not exceed half the normal allowable stress.

In cases where a header box needs to have more compartments than shown in any of the configurations in Figure 2.4, a provision is made that it may be analysed using the equations for configuration (8) of Figure 2.4. The only requirement of this provision is that the dimension assigned to h, the compartment height, be the size of the largest compartment included in the overall design. Thus a header box with more than three unequally sized compartments will be designed as if it is the three compartment header in configuration (8) with each compartment having the size of the largest compartment in the actual header box. This is an approach which becomes increasingly conservative as the number of compartments are increased past three.

One area of the design which is not completely covered by the code is how to deal with the holes on the side plate of the header box, where the inlet or outlet nozzles are situated. Due to the size of the nozzles, the side plate no longer falls within the specifications given by UG-39 of Division 1, which dictates how openings in the flat side of a pressure vessel should be reinforced. Usually, such openings are reinforced by placing a material replacement collar around the hole, but due to shape and size requirements for header boxes, applying this method is also not feasible. Over time, a practice has developed whereby designers universally apply a 0.5 ligament efficiency factor to any side plate where the nozzle hole is larger in diameter than half of the plate's shortest span, in order to compensate for any structural weakening. Although this practice is not recognised by ASME, it is widely adopted in industry.

Once the shape and size of a pressure vessel are determined, Section UG-34 of Division 1 is used to design the end plates. The thickness of the end plate, t, is calculated using Equations 2.3 and 2.4.

$$t = H\sqrt{\frac{ZCP}{SE}} \tag{2.3}$$

$$Z = max\left(1, min\left(2.5, 3.4 - 2.4\frac{H}{h}\right)\right) \tag{2.4}$$

where C is an attachment factor of 0.2 and E is the joint efficiency factor between the end plate and the sides of the vessel.

The nozzles are designed using a combination of equations from ASME and stress calculations based on resolution of forces. The relevant equations are given in Table 2.2 where E_j is the nozzle-side plate joint efficiency, S is the allowable material stress, d_i the nozzle inner diameter and d_o the nozzle outer diameter.

Table 2.2: Nozzle design formulae, adapted from (Ackers, 2012)

Equations	
Minimum required wall thickness for internal pressure (UG-27 of ASME VIII Div 1)	$t_{req} = \frac{Pd_i}{s\,(SE_j - 0.6P)}$
Circumferential stress	$S_h = \frac{Pd_i}{2t_n}$
Nozzle cross-sectional area	$A_{cross} = \frac{\pi}{4}\,(d_o^2 - d_i^2)$
Tensile stress caused by F_y	$S_t = \frac{F_y}{A_{cross}}$
Section modulus	$Z = \frac{2I}{d_o}$
Nozzle second moment of inertia	$I = \frac{\pi}{64}\,(d_o^4 - d_i^4)$
Resultant bending moment	$M_r = \sqrt{M_x^2 + M_z^2}$
Bending stress due to resultant moment	$S_b = \frac{M_r}{Z}$
Resultant hoop, normal and bending stress	$S_r = S_h + S_t + S_b$
Shear stress x-component	$\tau_x = \frac{2F_x}{\pi d_o t_n}$
Shear stress y-component	$\tau_y = \frac{2M_y}{\pi d_o^2 t_n}$
Shear stress z-component	$\tau_z = \frac{2F_z}{\pi d_o t_n}$
Resultant shear stress	$\tau_r = \tau_x + \tau_y + \tau_z$
Equivalent stress	$S_e = \sqrt{S_r^2 + 4\tau_r^2}$
Acceptance criteria	$S_e \leq S$

Modular design

The current design process is a modular design process, where each part of the header box is designed in near isolation. Only essential information is passed down from one design step to the next. Information is never passed back up the design tree, in order to make sure that subsequent design steps do not affect any of the preceding steps.

A good example of this is where the body of a header box is designed using only the requirements in Appendix 13 of Division 1 of the code. The nozzles are subsequently designed based on these dimensions, taking both pressure and nozzle loading into account. Once it is confirmed that the nozzles are strong enough, no further checks are performed to ensure that the header box body can sustain the added effect of the nozzle loading over and above the internal pressure loading.

One of the main reasons why information is only passed down the design process is that the code is known to be conservative (Becker, 2013). Thus designers may assume that even though all of the header box parts are designed in isolation, once they are put together, the conservative nature of the individual design process will ensure that the overall structure is still sound.

2.3 ASME requirements for processing FE analysis results

2.3.1 Stress linearisation

A large portion of this study will be based on results generated by FE analyses. ASME Section VIII Division 2 Part 5 (ASME, 2015) gives specific requirements on how stress results from structural analyses should be evaluated. According to the code, stress results need to be linearised through the thickness of the pressure vessel. This allows for the three-dimensional stress results of a FE analysis to be interpreted into one of three components. These are membrane, bending and peak stresses. Figure 2.5 shows a visual illustration of what each of these components represent. The positions at which stresses are linearised are called stress classification lines (SCL).

Membrane stress is the average of the component stresses along the SCL and is calculated using Equation 2.5. σ_{ij} represents the component stress values at the nodes along the SCL. $\sigma_{ij,m}$ is calculated for each of the six nodal stress components which are then combined using the von Mises formulations to yield an equivalent membrane stress for the SCL position.

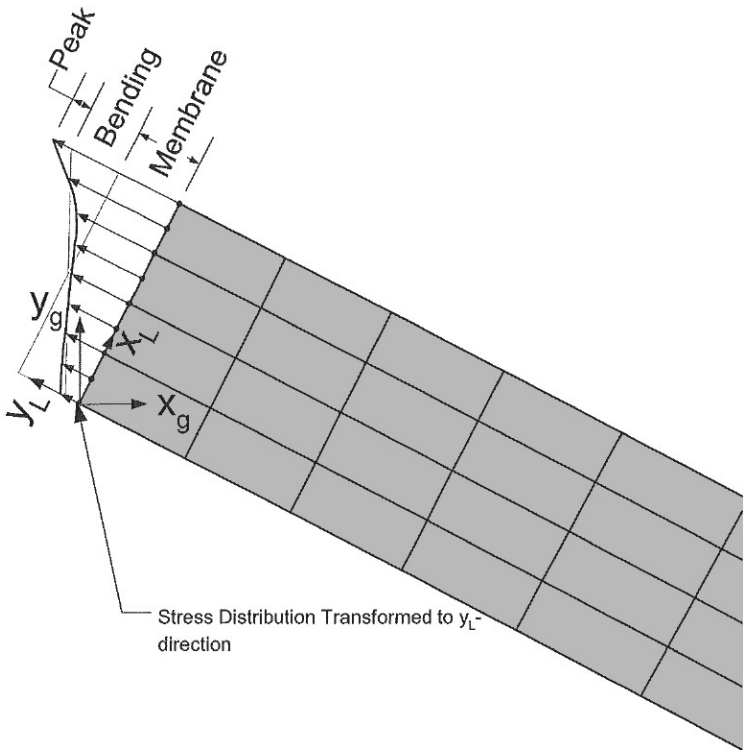

Figure 2.5: Stress classification, adapted from (ASME, 2015)

$$\sigma_{ij,m} = \frac{1}{t}\int_0^t \sigma_{ij}\, dx \tag{2.5}$$

Bending stress represents the portion of the component stresses along the SCL which varies linearly. The same procedure is followed as before, using Equation 2.6 instead to calculate the bending stress values. A minor difference however is that while the membrane stress calculations are performed for all six nodal stress components, the bending stress calculations only consider three of these components. According to the code, only stress components in the local hoop and normal directions and the shear component in the hoop-normal plane should be considered, as these are the only components that contribute to the bending of the structure at the point where a SCL is placed. The orientation of the hoop and normal directions is shown in Figure 2.6. Thus, if a SCL was positioned along the x-axis at a point within a structure, then only the linearised bending stress components for σ_y, σ_z and σ_{yz} should be included in the von Mises calculation for the equivalent bending stress at that point.

$$\sigma_{ij,b} = \frac{6}{t^2}\int_0^t \sigma_{ij}\left(\frac{t}{2} - x\right) dx \tag{2.6}$$

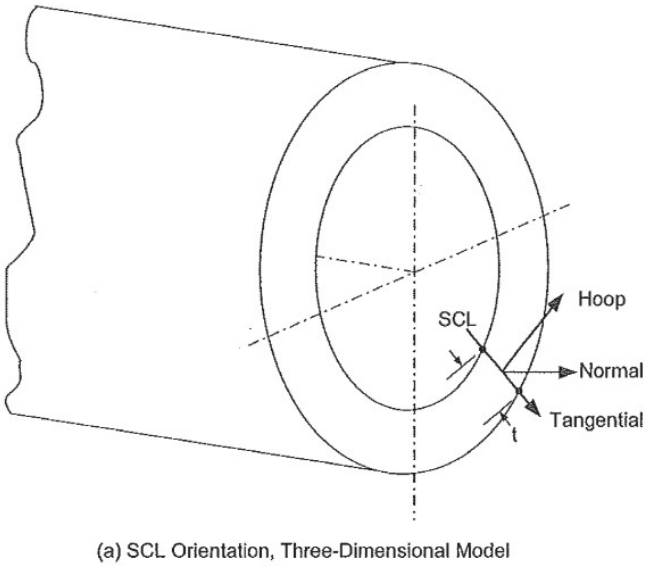

Figure 2.6: SCL orientation for 3D FE model (ASME, 2015)

Peak stress is the component that exceeds the membrane and bending stresses. Peak stress is however not relevant to this study as it is only used for fatigue failure assessment, which is not a concern in this study as header boxes do not commonly undergo high load cycle rates.

A combined stress that will be referred to later and which is required for the failure assessment of pressure vessels is the 'membrane plus bending stress'. This combined stress cannot be calculated by simply adding the values of the previously calculated equivalent von Mises membrane and bending stresses. Rather, this value is calculated by adding the individually linearised component stress values that would be used for the equivalent membrane and bending stress calculations to one another and then calculating a new 'membrane plus bending' equivalent von Mises value based on these combined component values.

2.3.2 SCL placement

The code provides guidance as to where SCLs should be placed. Figure 2.7a and Figure 2.7b are examples of this, showing where an SCL should be positioned to analyse the stress where a nozzle meets a pressure vessel. These guidelines show that the SCL should be positioned on the edge of the region that forms the junction between the plate and the nozzle, at the toe of the welds. Additionally, SCLs must also be placed in a similar position at the weld toe where two plates meet and along the central span of flat plates to assess the stress levels in these areas.

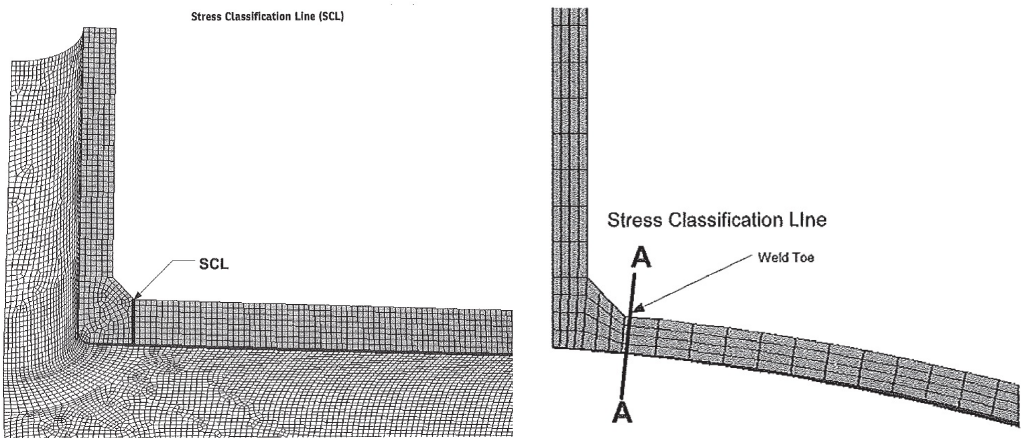

(a) SCL positioning (ASME, 2015) (b) SCL at weld toe (ASME, 2015)

Figure 2.7: SCL positioning at nozzle and wall intersections

2.3.3 Stress classification and failure criteria

Once stresses have been linearised, the code further requires that all stresses be categorised for the purpose of failure assessment. There are three main stress categories, namely primary, secondary and peak. Stresses are categorized according to where they have been extracted from, what type of loading caused them (for example mechanical or thermal loading) and whether they have the ability to cause distortion to the component.

In short, primary stresses are caused as a direct result of external loading on a component. Secondary stresses occur as a result of constraints between adjacent parts or because of severe structural discontinuities and can be caused by external loading. Secondary stresses can also be caused by thermal loading, while primary stresses cannot. Peak stresses are stresses that do not cause noticeable distortion, but may be the source of fatigue cracks or brittle failure. Figure 5.1 from ASME VIII Division 2 gives further descriptions of all the stress categories and a schematic of how the stresses from each category are used to test for failure. The figure is shown here as Figure 2.8.

Out of the five failure criteria shown in Figure 2.8, only four are applicable to the design of plug type header boxes. They are the failure criteria that deal with the protection against plastic collapse and ratcheting in the header box. These criteria are repeated in Equations 2.7 to 2.10, where S is the material allowable stress, S_{PL} is the allowable local primary membrane and local primary membrane plus bending stress and S_{PS} is the allowable primary plus secondary stress range. The other criterion protects again fatigue failure, which is not applicable in this study as header boxes do not commonly undergo high load cycle rates. An additional failure criterion from the code is given by

Figure 5.1
Stress Categories and Limits of Equivalent Stress

Stress Category	Primary			Secondary Membrane plus Bending	Peak
	General Membrane	Local Membrane	Bending		
Description (For examples, see Table 5.2)	Average primary stress across solid section. Excludes discontinuities and concentrations. Produced only by mechanical loads.	Average stress across any solid section. Considers discontinuities but not concentrations. Produced only by mechanical loads.	Component of primary stress proportional to distance from centroid of solid section. Excludes discontinuities and concentrations. Produced only by mechanical loads.	Self-equilibrating stress necessary to satisfy continuity of structure. Occurs at structural discontinuities. Can be caused by mechanical load or by differential thermal expansion. Excludes local stress concentrations.	1. Increment added to primary or secondary stress by a concentration (notch). 2. Certain thermal stresses which may cause fatigue but not distortion of vessel shape.
Symbol	P_m	P_L	P_b	Q	F

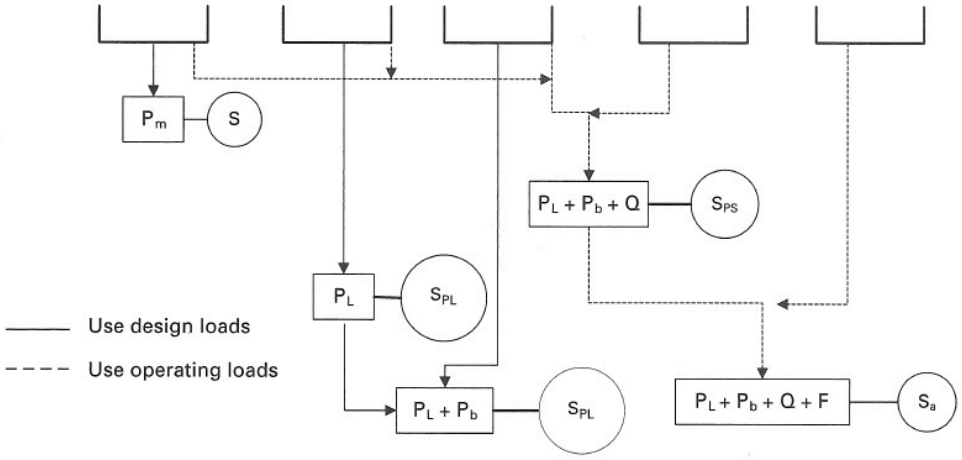

Figure 2.8: Stress categories (ASME, 2017)

Equation 2.11 which ensures protection against local failure. σ_1, σ_2 and σ_3 are the principal stresses based on the membrane plus bending stress components.

$$P_m \leq S \tag{2.7}$$

$$P_L \leq S_{PL} \tag{2.8}$$

$$P_L + P_b \leq S_{PL} \tag{2.9}$$

$$P_L + P_b + Q \leq S_{PS} \tag{2.10}$$

$$\sigma_1 + \sigma_2 + \sigma_3 \leq 4S \tag{2.11}$$

2.3.4 Equivalent Material Modelling

When a FE model is set up to validate a single header box design, the process is fairly simple. Only a single CAD model needs to be imported, meshed, loaded and simulated in order to reach the final results. When setting up a FE model that will be used to generate data for a meta-model however, one needs to plan for the fact that the FE model will be used as the basis of thousands of simulations. It is thus imperative to make sure that the FE model is as computationally robust and efficient as possible (the concept of meta-modelling and reason why so may FE models will have to be simulated are discussed in the next chapter).

One of the ways to reduce the computational complexity of a header box model is to replace the perforated plates, representing the plug and tube sheets, with a solid material having equivalent material properties to the perforated plates. The ASME code makes provision for this approach and includes in Appendix 5-E of Division 2 requirements for calculating equivalent material properties for plates with square or equilateral triangular perforation patterns. After an analysis is run with these modified properties, the actual stresses are calculated by multiplying the results with a stress multiplication factor computed for the effective solid plate.

2.4 Supporting research

In the past, numerous studies have been performed in the field of rectangular pressure vessel design and a few of them are briefly discussed here. No work has however been published that models the structural design of a complete plug type header box, with all of its components.

Zeng *et al.* (1990) developed a new model for the design of rectangular vessels subject to internal pressure. Their model improved on the formulae given by Division 1 of ASME. However, it only focussed on the design of the side walls of a rectangular pressure vessel and did not include calculations for the end plates or nozzles.

Nel *et al.* (2012) looked at the design of an un-partitioned plug type header box. They attempted to develop a new design method, based on rigid frame theory, which would account for the effect of nozzle loading on the structure of the header box, but found that this was not possible. One of the main reasons for this is that nozzle loading takes place in three dimensions, while rigid frame theory only allows for calculations in two dimensions.

Ackers (2012) looked at combining the mechanical and thermal design of a plug type header box. His aim was to improve the cost to performance ratio of these header boxes. He made a valuable contribution by showing how a favourable selection of header box component configurations can improve the overall cost to performance ratio of plug type header boxes. His study did, however, not focus on improving the actual methods used for the structural design of plug type header boxes.

Chapter 3

Literature review: Meta-modelling

The focus of this study will be to construct a meta-model that can accurately predict the structural behaviour of a plug type header box. A meta-model is a mathematical model that predicts the behaviour of another model, based on a set of test or simulation results. No such model has been found in literature describing the design of rectangular pressure vessels.

The construction of such a meta-model will involve setting up and testing numerous FE models of header boxes encompassing a wide array of header box configurations, shapes and sizes. This will generate a database of results describing how a set of known header box designs behave. These test results will be correlated and have trend models fitted to them in order to construct a meta-model which will predict the structural behaviour of future header boxes, without having to simulate them individually.

3.1 Design of experiments (DOE)

In order to create a meta-model, test or simulation data needs to be collected. A key aspect in the DOE process is deciding where to sample this data in the design space.

The most basic sampling method is full factorial sampling. For this method, a set number of points are selected along the design space of each variable, usually two or three. Data is then sampled at every point formed by a unique combination of the points selected for each individual design variable. This method is illustrated in Figure 3.1, for a two and a three variable design space (the figure refers to variables as factors). The example shows a sample frequency of two points per design variable with the dots representing the sampling points.

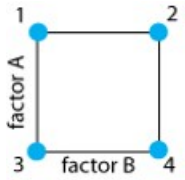

trial	A	B
1	+	−
2	+	+
3	−	−
4	−	+

(a)

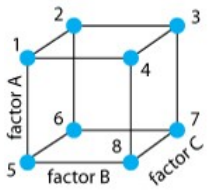

trial	A	B	C
1	+	−	−
2	+	−	+
3	+	+	+
4	+	+	−
5	−	−	−
6	−	−	+
7	−	+	+
8	−	+	−

(b)

Figure 3.1: Full factorial sampling (Harvey, 2013)

When sampling only two points per variable in this manner, it is only possible to deduce linear relationships between variables. In order to expand this capability to identifying quadratic trends, without the addition of sampling points on each variable, the Central Composite method can be employed. As shown in Figure 3.2, this method adds a central sample point and a number of star points, all of which increase the accuracy of quadratic trend identification.

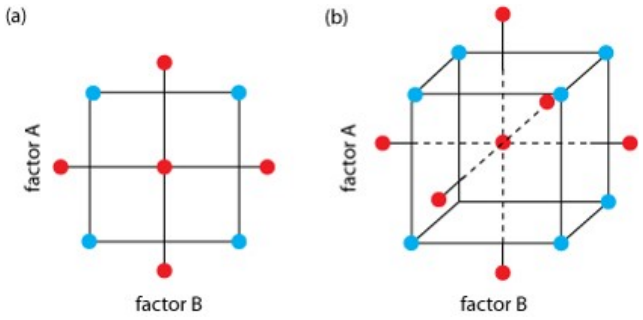

Figure 3.2: Central composite sampling (Harvey, 2013)

The major drawback of these methods is that the number of sample points grow exponentially with the number of design variables. These sampling methods are thus only suitable for design problems with a small number of variables.

A different method for choosing sample points is Latin Hypercube (LHC) sampling (McKay *et al.*, 1979). In this method, each design variable is split into an arbitrary number of subdivisions. The sampling points are then made up of random combinations of variable subdivisions, but such that every variable subdivision is only used as part of one combination (Cavazzuti, 2013). This method is illustrated in Figure 3.3, where the variables are divided into five subdivisions. A benefit of the LHC sampling is that the method can be expanded to work for any number of variables while still maintaining the ability to only sample the desired amount of points, thus giving the user more control.

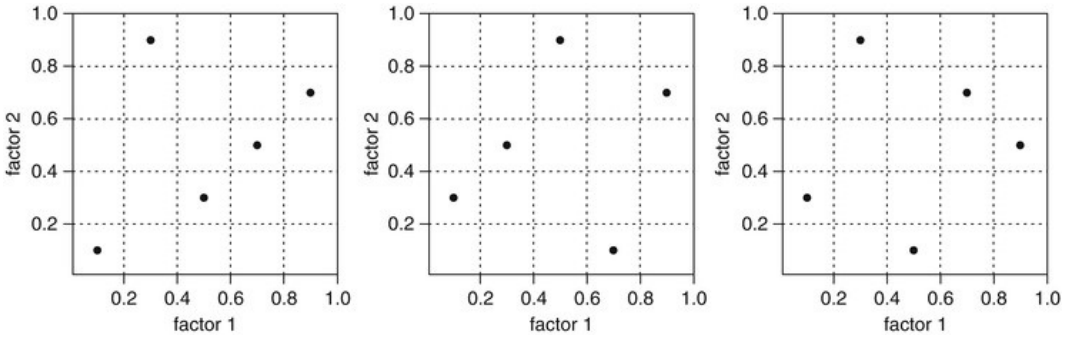

Figure 3.3: Latin hypercube sampling, adapted from (Hung, 2013)

A weakness of the Latin Hypercube method is that it is possible for sample points to be randomly chosen in such a manner that there is a strong correlation between the points. This yields weak space filling characteristics. An example of this is shown in Figure 3.4 (a). Figure 3.4 (b) on the other hand shows an example of Latin Hypercube sampling with good space filling properties and less correlation between the points.

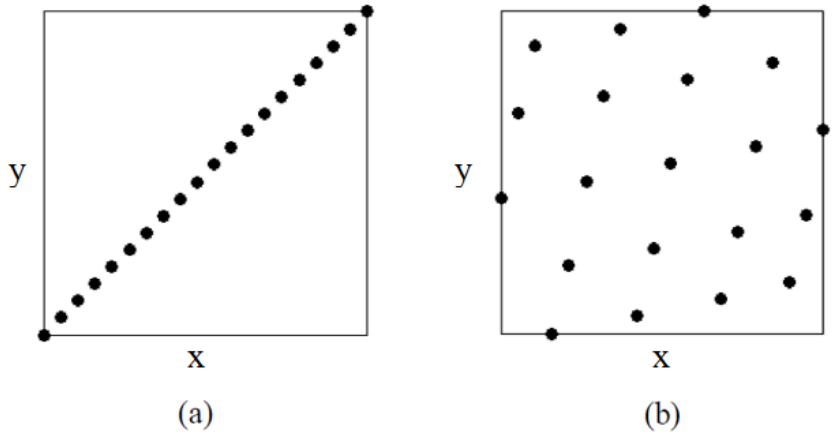

Figure 3.4: Latin hypercube examples, adapted from (Viana, 2013)

Much research has been done to find methods to optimise the Latin Hypercube sampling distribution. There is however no clear answer as to what the objective function of such methods should be. Some authors favour optimising the space filling properties of the sampling layout, while others advocate minimising the dimensional correlation between sampling points. Still, there is no way of showing, unless proven for a specific problem, that either of these approaches will necessarily yield a better result (Viana, 2013).

Even with a reasonable objective function for which to optimise the sampling pattern, the optimisation itself is still a very intensive procedure. This is

because the search space has possible design options on the order of $(p!)d$, where p is the number of sample points and d is the number of dimensions (Viana, 2013). To optimise the position of only ten points in a space with three variables, there are more than 10^{19} possible designs. For twenty samples in a four variable design space, there are in excess of 10^{73} possible designs. It is thus evident that this problem scales very badly as one moves to higher dimensions. In comparison, a reasonably inexpensive alternative is to generate a number of random sampling patterns and then choose the best one from this pool. This way, one can avoid spending more computational effort on finding the sampling points than on evaluating the actual design problem.

3.2 Mathematical models

Numerous data models are available that can be fitted to a data set to approximate its behaviour. All models will, however, not perform equally under the same conditions. Each model has its own strengths and weaknesses and will be better suited to certain data sets. A few well known data models are discussed below.

3.2.1 Response surface approximation

A response surface approximation works by fitting a polynomial model to a data set. Depending on the dimensionality and behaviour of the data, the model can range from being a constant value to a higher order hyper plane spanning multiple dimensions. An advantage of a response surface approximation is that it yields an explicit function which describes the data and from which gradient information can be extracted. This simplifies optimisation of the system as it allows for gradient based optimisation to be used. A drawback of this method is that it is limited in its capacity to approximate highly non-linear data sets.

As an example, consider the case where a second order response surface is fitted to a two dimensional data set. The equation for this response surface is given by Equation 3.1 (Myers *et al.*, 2009).

$$h(\boldsymbol{x}) = \beta_0 + \beta_1 x_1 + \beta_2 x_2 + \beta_3 x_1^2 + \beta_4 x_2^2 + \beta_5 x_1 x_2 \tag{3.1}$$

To estimate the β_i parameters, a least squares regression can be applied. For this the training points of the model are put in the form

$$\boldsymbol{y} = \mathbf{X}\boldsymbol{\beta} + \boldsymbol{\varepsilon} \tag{3.2}$$

where

$$\boldsymbol{y} = \begin{bmatrix} y_1 \\ y_2 \\ \vdots \\ y_n \end{bmatrix}, \quad \boldsymbol{\beta} = \begin{bmatrix} \beta_0 \\ \beta_1 \\ \vdots \\ \beta_5 \end{bmatrix}, \quad \boldsymbol{\varepsilon} = \begin{bmatrix} \varepsilon_1 \\ \varepsilon_2 \\ \vdots \\ \varepsilon_n \end{bmatrix}$$
$$\mathbf{X} = \begin{bmatrix} 1 & x_{11} & x_{21} & x_{11}^2 & x_{21}^2 & x_{11}x_{21} \\ 1 & x_{12} & x_{22} & x_{12}^2 & x_{22}^2 & x_{11}x_{22} \\ \vdots & \vdots & \vdots & \vdots & \vdots & \vdots \\ 1 & x_{1n} & x_{2n} & x_{1n}^2 & x_{2n}^2 & x_{1n}x_{2n} \end{bmatrix} \tag{3.3}$$

Here, $\mathbf{X}$ and $\boldsymbol{y}$ contain the n training points and $\boldsymbol{\varepsilon}$ represents the error at each training point. $\boldsymbol{\beta}$ is the vector of unknown regression coefficients. A vector, $\boldsymbol{b}$, is required to estimate the parameters of $\boldsymbol{\beta}$ such that the sum of the squared errors, given by Equation 3.4, is minimised.

$$L = \sum_{i=1}^{n} \varepsilon_i^2 = \boldsymbol{\varepsilon}^T\boldsymbol{\varepsilon} = (\boldsymbol{y} - \mathbf{X}\boldsymbol{\beta})^T(\boldsymbol{y} - \mathbf{X}\boldsymbol{\beta}) \tag{3.4}$$

By multiplying out the terms this equation may be simplified to

$$L = \boldsymbol{y}^T\boldsymbol{y} - 2\boldsymbol{\beta}^T\mathbf{X}^T\boldsymbol{y} + \boldsymbol{\beta}^T\mathbf{X}^T\mathbf{X}\boldsymbol{\beta} \tag{3.5}$$

This equation presents a quadratic problem which allows for the estimator, $\boldsymbol{b}$, to be found by setting the derivarite equal to zero, as shown in Equation 3.6.

$$\frac{\partial L}{\partial \boldsymbol{\beta}}\Big|_{\boldsymbol{b}} = -2\mathbf{X}^T\boldsymbol{y} + 2\mathbf{X}^T\mathbf{X}\boldsymbol{b} = 0 \tag{3.6}$$

This can be simplified to

$$\mathbf{X}^T\mathbf{X}\boldsymbol{b} = \mathbf{X}^T\boldsymbol{y} \tag{3.7}$$

which yields

$$\boldsymbol{b} = (\mathbf{X}^T\mathbf{X})^{-1}\mathbf{X}^T\boldsymbol{y} \tag{3.8}$$

The result of solving this system will then produce a response surface comparable to that in Figure 3.5.

Due to the high cost of calculating the inverse of $\mathbf{X}^T\mathbf{X}$, these systems are usually not solved directly. Instead these systems are more often solved by means of Cholesky or QR Factorisation, in cases when $\mathbf{X}$ is full rank. An alternative way of solving a least squares regression is to calculate $\boldsymbol{b}$ by means of a singular value decomposition (SVD) method pioneered by Golub and

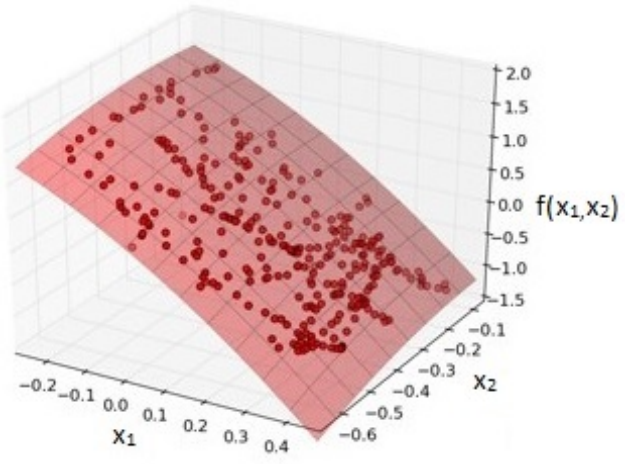

Figure 3.5: Second order surface fit, adapted from (Kassner, 2011)

Reinsch (1970). This method is particularly useful when fitting higher order RS models, where the $\mathbf{X}$ matrix is at or near rank deficiency (Lin, 2006). This is often encountered when fitting high order RS models with a large number of variables. A brief explanation of the method is given below based on the work of Jiguan Lin (2006).

For an $n \times p$ matrix $\mathbf{X}$, a SVD yields a $n \times n$ orthogonal matrix $\mathbf{U} = [\mathbf{u}_1, ..., \mathbf{u}_n]$, a $p \times p$ orthogonal matrix $\mathbf{V} = [\mathbf{v}_1, ..., \mathbf{v}_p]$ and a $n \times p$ matrix $\mathbf{S}$ whose only non-zero elements lie on the leading diagonal and are non-negative such that

$$\mathbf{U}^T\mathbf{X}\mathbf{V} = \mathbf{S} \quad \text{or} \quad \mathbf{X} = \mathbf{U}\mathbf{S}\mathbf{V}^T \tag{3.9}$$

Using the orthogonal properties of $\mathbf{U}$ and $\mathbf{V}$, we also know that $\mathbf{X}^T = \mathbf{V}\mathbf{S}^T\mathbf{U}^T$ and $\mathbf{X}^T\mathbf{X} = \mathbf{V}\mathbf{S}^T\mathbf{S}\mathbf{V}^T$, which when combined with Equation 3.7 yields

$$\mathbf{V}\mathbf{S}^T\mathbf{S}\mathbf{V}^T\boldsymbol{b} = \mathbf{V}\mathbf{S}^T\mathbf{U}^T\boldsymbol{y} \quad \text{or} \quad \mathbf{S}^T\mathbf{S}\mathbf{V}^T\boldsymbol{b} = \mathbf{S}^T\mathbf{U}^T\boldsymbol{y} \tag{3.10}$$

Now we denote the rank of matrix $\mathbf{X}$ as r, such that $\mathbf{S}_r = diag\{s_1, ..., s_r\}$ contains all the non-zero singular values of $\mathbf{X}$. If we then partition $\mathbf{U}$ and $\mathbf{V}$ such that $\mathbf{U} = [\mathbf{U}_r, \mathbf{U}_z]$, where $\mathbf{U}_r = [\boldsymbol{u}_1, ..., \boldsymbol{u}_r]$ consisting of the first r columns of $\mathbf{U}$ and $\mathbf{V} = [\mathbf{V}_r, \mathbf{V}_z]$, where $\mathbf{V}_r = [\boldsymbol{v}_1, ..., \boldsymbol{v}_r]$ consisting of the first r columns of $\mathbf{V}$, Equation 3.10 takes on the form

$$\begin{bmatrix} \mathbf{S}_r^2 & 0 \\ 0 & 0 \end{bmatrix} \begin{bmatrix} \mathbf{V}_r^T \\ \mathbf{V}_z^T \end{bmatrix} \boldsymbol{b} = \begin{bmatrix} \mathbf{S}_r & 0 \\ 0 & 0 \end{bmatrix} \begin{bmatrix} \mathbf{U}_r^T \\ \mathbf{U}_z^T \end{bmatrix} \boldsymbol{y}$$

which can be simplified to

$$\mathbf{S}_r\mathbf{S}_r\mathbf{V}_r^T\boldsymbol{b} = \mathbf{S}_r\mathbf{U}_r^T\boldsymbol{y} \tag{3.11}$$

When rearranged, this yields Equation 3.12, which is now trivial to solve once the SVD has been performed, as $\mathbf{V}_r$ and $\mathbf{U}_r^T$ are then known and $\mathbf{S}_r^{-1}$ is simply the inverse of a diagonal matrix.

$$\boldsymbol{b} = \mathbf{V}_r \mathbf{S}_r^{-1} \mathbf{U}_r^T \boldsymbol{y} \tag{3.12}$$

3.2.2 Kriging

Kriging is an optimal interpolation technique based on the regression of a set of observed values around a point, where the influence of each point is weighted according to a spatial covariance value (Bohling, 2005). An advantage of Kriging is that it is flexible enough to approximate a diverse range of problems (Martin and Simpson, 2004), both linear and non-linear (Simpson *et al.*, 2001). A Kriging model is a combination of two functions. The first is a global model and the second is a localised departure model (Simpson *et al.*, 2001), given by

$$h(\boldsymbol{x}) = f(\boldsymbol{x}) + Z(\boldsymbol{x}) \tag{3.13}$$

where $h(\boldsymbol{x})$ is the hypothesis function and $f(\boldsymbol{x})$ is a known approximation, usually a constant or polynomial. $Z(\boldsymbol{x})$ is a stationary random field with a zero mean and covariance given by

$$cov(\boldsymbol{x}_1, \boldsymbol{x}_2) = \sigma^2 R(\boldsymbol{x}_1, \boldsymbol{x}_2) \tag{3.14}$$

where the process variance, σ^2, scales a spatial correlation function, $R(\boldsymbol{x}_1, \boldsymbol{x}_2)$.

In simple terms, Kriging estimates the function value at a point by taking the global approximation at that point and adding to it a deviation value. The deviation value is calculated based on the function values of the points around the point of interest and their relative spatial relation and covariance to it.

3.2.3 Radial Basis Function

The Radial Basis Function (RBF) method (Broomhead and Lowe, 1988) works by assuming that every point in an available data set will influence the function approximation at any other point, based on its distance from that point (Abu-Mostafa, 2012). This method is implemented by placing a RBF at each data point. An overall function approximation, $h(\boldsymbol{x})$, is then calculated as a weighted sum of all the RBF's in the design space, as given by

$$h(\boldsymbol{x}) = \sum_{i=1}^{n} \omega_i \phi \left(||\boldsymbol{x} - \boldsymbol{x}_i|| \right) \tag{3.15}$$

where ω_i is a weight coefficient and n represents the number of training points in the data set. ϕ is a RBF based on the Euclidean norm, $||\boldsymbol{x} - \boldsymbol{x}_i||$, between

the training point $\boldsymbol{x}_i$ and the design point $\boldsymbol{x}$. A frequently used RBF is the Gaussian formulation given by

$$\phi\left(||\boldsymbol{x} - \boldsymbol{x}_i||\right) = exp\left(-\gamma||\boldsymbol{x} - \boldsymbol{x}_i||^2\right) \tag{3.16}$$

where γ is a scaling factor which controls the influence of the radial basis function. This influence is illustrated by Figure 3.6.

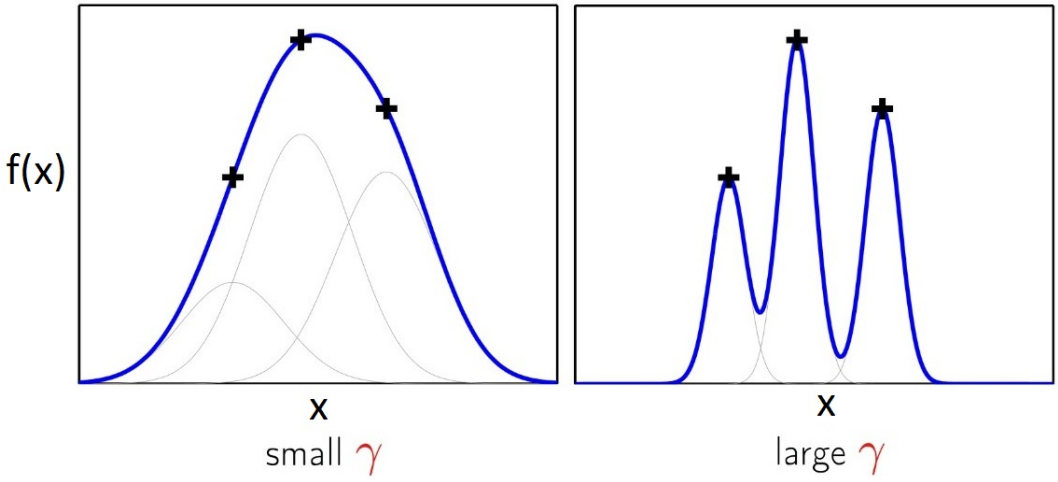

Figure 3.6: Effect of varying γ, adapted from (Abu-Mostafa, 2012)

An advantage of radial basis functions is that they can be differentiated. Thus they can be used directly as part of a gradient based optimisation.

3.2.4 Support Vector Regression

Support Vector Regression (SVR) (Vapnik, 1995) is a form of a Support Vector Machine which is used for function estimation. Traditionally, Support Vector Machines are used for classification and attempt to maximise the margin between different sets of data. SVR attempts to find a function which follows a set of training data and maximises the number of points falling within a set margin, ε, of the function while allowing for some outliers, as shown in Figure 3.7. A basic formulation of the function the SVR attempts to fit is given by

$$y = \sum_{i=1}^{n} (\boldsymbol{\alpha}_i - \boldsymbol{\alpha}_i^*) \cdot \langle \boldsymbol{x}_i, \boldsymbol{x} \rangle + b \tag{3.17}$$

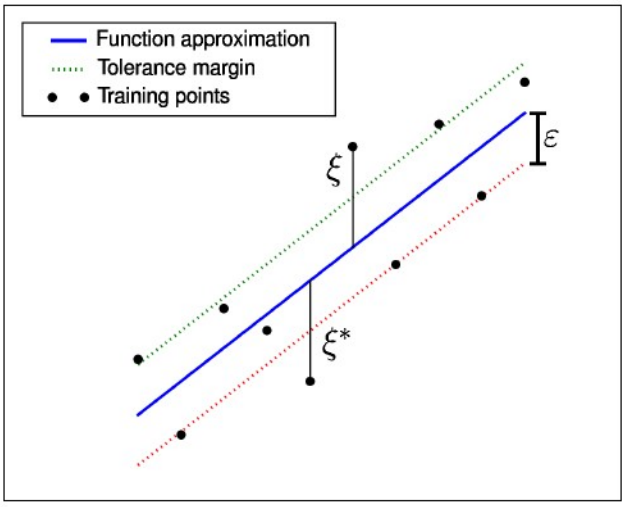

Figure 3.7: Support vector regression with provision for outliers (Wise, 2008)

Here we see that the approximation at a design point $\boldsymbol{x}$ is a function of a set of weight vectors, $\boldsymbol{\alpha}_i$ and $\boldsymbol{\alpha}_i^*$ and the dot product between the training points $\boldsymbol{x}_i$ and the design point. A powerful feature of SVR is the ability to exchange this dot product, known as a linear kernel for other non-linear kernels. Some examples of other kernels are shown in Table 3.1. This essentially allows the SVR to map non-linear data into a feature space where it can be fit linearly, thus enhancing SVRs ability to approximate non-linear data.

Table 3.1: SVR kernels

Linear	$\langle \boldsymbol{x}_1 \cdot \boldsymbol{x}_2 \rangle$
Polynomial	$\langle \boldsymbol{x}_1 \cdot \boldsymbol{x}_2 \rangle^d$
Guassian Radial Basis Function	$e\left(\frac{-\|\|\boldsymbol{x}_1 - \boldsymbol{x}_2\|\|^2}{2\sigma^2}\right)$

3.3 Number of sample points

Part of the DOE process is to determine how many sample points are needed to fit a suitable meta-model. There are two principal boundaries to this problem. At the top end of the scale, the number of points to be sampled is capped by the computational expense of evaluating all the sample points. The lower end of the scale is capped by the amount of points that are required to successfully fit a curve or trend. For example, the curve given by Equation 3.18 will require at least three sample points to be fitted.

$$f(\boldsymbol{x}) = \beta_0 + \beta_1 x_1 + \beta_2 x_2^2 \tag{3.18}$$

Depending on the nature of the data though, three sample points may not be sufficient to accurately predict the underlying trend of the data set. This concept is illustrated in Figure 3.8. In the figure, the solid line represents a quadratic trend line fitted to all of the shown data points. The dashed line is a quadratic curve which is fitted to only three of the sample points, the minimum required number. The example illustrates how fitting a trend using too few data points may misrepresent the actual data trend.

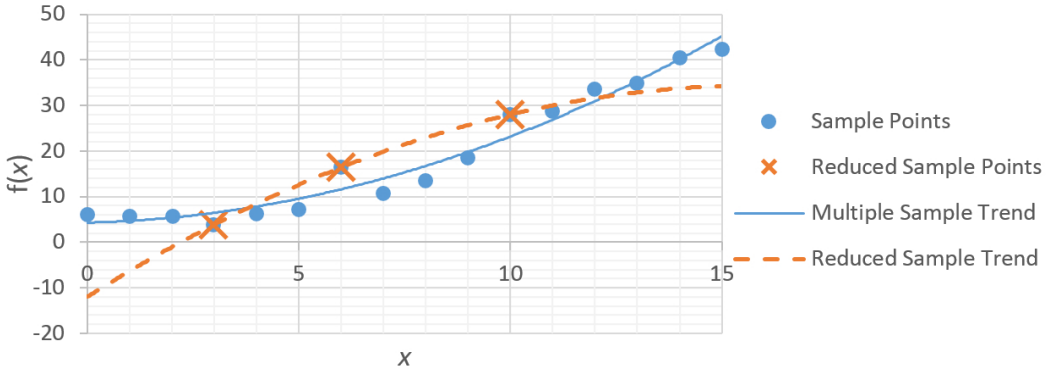

Figure 3.8: Sample curve fit

In order to determine the effective minimum number of required sample points, a lower accuracy boundary may be established by means of an error calculation or performance measure. This lower bound, governing the number of necessary sample points, will however be unique to each case, depending on a combination of the behaviour of the sample data and the model being trained.

3.4 Error calculation and performance estimation

Error calculation is simply a method of quantifying how well a given curve or model fits a given set of data. This information can be used to help estimate a model's performance. The following description of error calculation and various cross validation methods is based on two sets of notes produced by Ricardo Gutierrez-Osuna (2015) and Yaser Abu-Mostafa (2012) respectively.

Cross validation works by dividing the available data set of sampled points into two groups. The first is used to fit a hypothesis model and is called the training set. The remaining group is used to test the hypothesis model and is called the testing set.

There are a number of schemes that propose how the testing set should be selected as a portion of the overall sampled data set. The most basic is the Holdout method, illustrated in Figure 3.9. Using this method, a fixed portion of the available test data is kept aside for testing while the training set is used to train a model. The drawback of this method is that none of the data in the test set is ever used to train the model and is costly to generate. Also, if there is a significant trend deviation which only appears in the test set, this information will be completely lost.

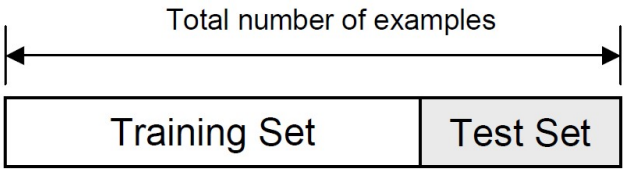

Figure 3.9: Holdout cross validation Gutierrez-Osuna (2015)

A method that reduces the probability of trend information being lost is the Leave-one-out method, which uses all the available data both for training and testing. As shown in Figure 3.10 the data is split n times, each time fitting the model to all the data points except one. The one data point that was not used for fitting the model, is used to test the fit.

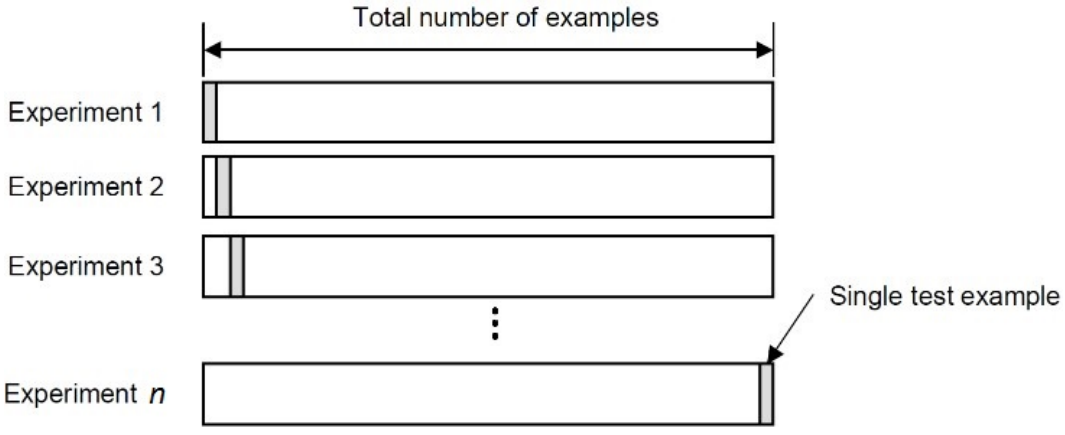

Figure 3.10: Leave-one-out cross validation, adapted from Gutierrez-Osuna (2015)

This method is however not suitable for systems with large data sets as it is computationally expensive. In such cases a variation of the leave-one-out method may be preferred, where an incrementing subset of testing samples are left out each time. This method is illustrated in Figure 3.11.

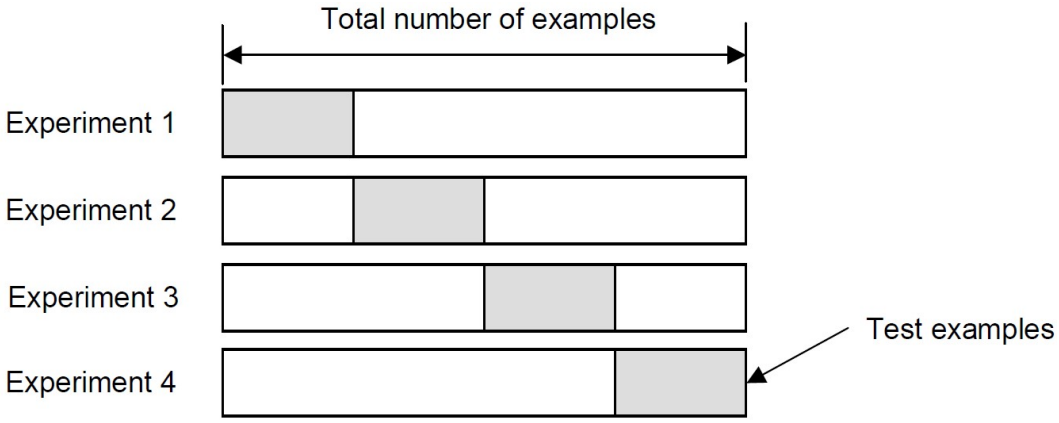

Figure 3.11: Leave-many-out cross validation Gutierrez-Osuna (2015)

The end goal of cross validation is to assist with performance estimation. One way of testing the hypothesis model is by calculating the mean of the squared errors over all the points in the testing set, which yields a representation of how well the samples in the testing set fit the hypothesis model. The mean squared error, E_i, is given by

$$E_i = \frac{1}{K} \sum_{k=1}^{K} \left(h\left(\boldsymbol{x}_k\right) - f\left(\boldsymbol{x}_k\right) \right)^2 \tag{3.19}$$

where K is the number of data points used to test the model. $\boldsymbol{x}$ is the vector of design variables $\{x_0, x_1, ..., x_d\}$ and $h(\boldsymbol{x})$ is the function evaluation of the hypothesised model at $\boldsymbol{x}$. $f(\boldsymbol{x})$ is the value of the target function sampled at $\boldsymbol{x}$ and the subscript 'i' is used to denote the fact that the calculate error relates to a specific test set. In cases where a leave-one or leave-many-out testing format is used, the overall error simply becomes the mean of the errors for each test, as per Equation 3.20, where N is the number of error calculations performed.

$$E = \frac{1}{N} \sum_{i=1}^{N} E_i \tag{3.20}$$

Figure 3.12 shows a simplified illustration of how cross validation can be used to compare the performance of two models used to approximated the same data set. The illustration uses the leave-one-out method to fit a linear

and a constant model to the same data points. The results show that the overall error is lower when the constant model is fitted than when the linear model is fitted. In the same way, this method can be used to compare any number of data models to one another.

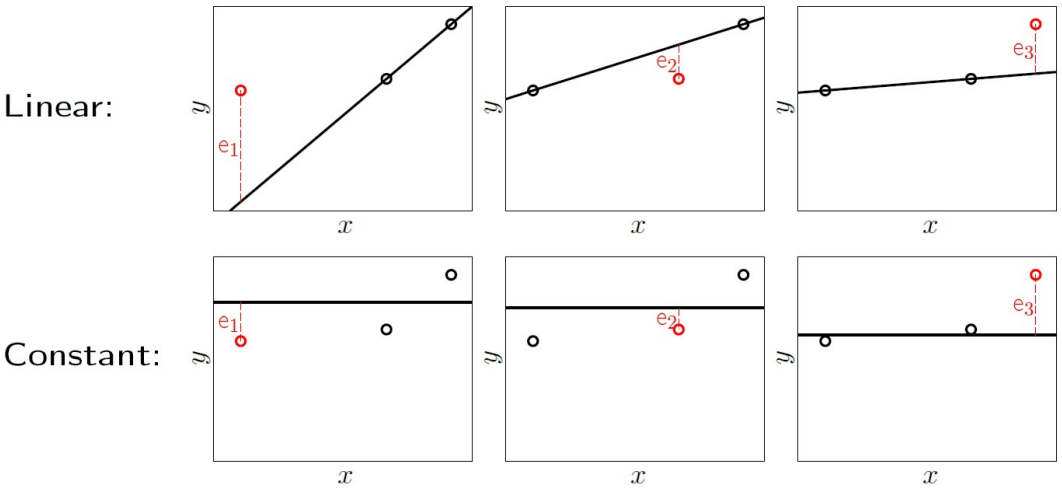

Figure 3.12: Leave-many-out cross validation Abu-Mostafa (2012)

Another method that can be used to assess the performance of a model is to calculate its R-squared value. A R-squared value is a measure that relates what percentage of the variance in a set of data can be explained by a model being used to approximate it. It is calculated using

$$R^2 = 1 - \frac{\sum_i (f(\boldsymbol{x}_i) - h(\boldsymbol{x}_i))^2}{\sum_i (f(\boldsymbol{x}_i) - \bar{f})^2} \tag{3.21}$$

where $h(\boldsymbol{x})$ is the function evaluation of the hypothesised model at $\boldsymbol{x}$, $f(\boldsymbol{x})$ is the value of the target function sampled at $\boldsymbol{x}$ and $\bar{f}$ is mean of the sampled values. The closer the R-squared value is to one, the higher the performance of the model is deemed to be, while having a R-squared value of zero means that the model does not explain any of the variance in the data.

While the performance measures described thus far have all been calculated values, visual methods also exist for gauging the performance of a model. One such method is to compare the actual values for a set of sampled data with those predicted by a model on a graph. Two examples of such a plot are shown in Figures 3.13 and 3.14. On these graphs, the closer the points lie to the 45° line running through the middle of the plot, the more accurate the prediction is. One can thus qualitatively see that the model in Figure 3.13 performs better than that in Figure 3.14. These graphs are also useful for assessing the overall accuracy bounds or error margins of a model, while other

performance measures such as R-squared only yield a representative measure of performance which does not convey this information.

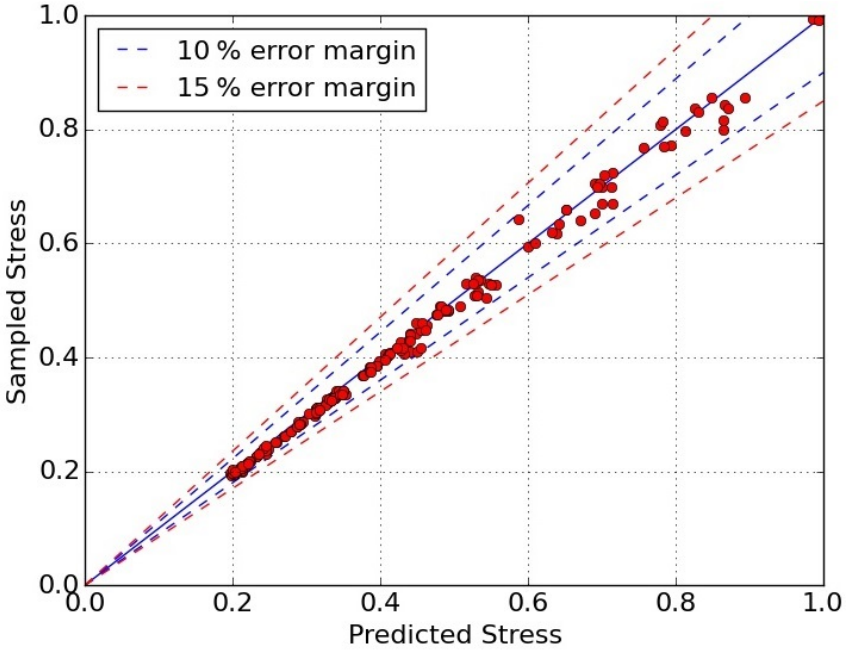

Figure 3.13: Sampled vs predicted results for accurate fit: $R^2 = 0.9981$

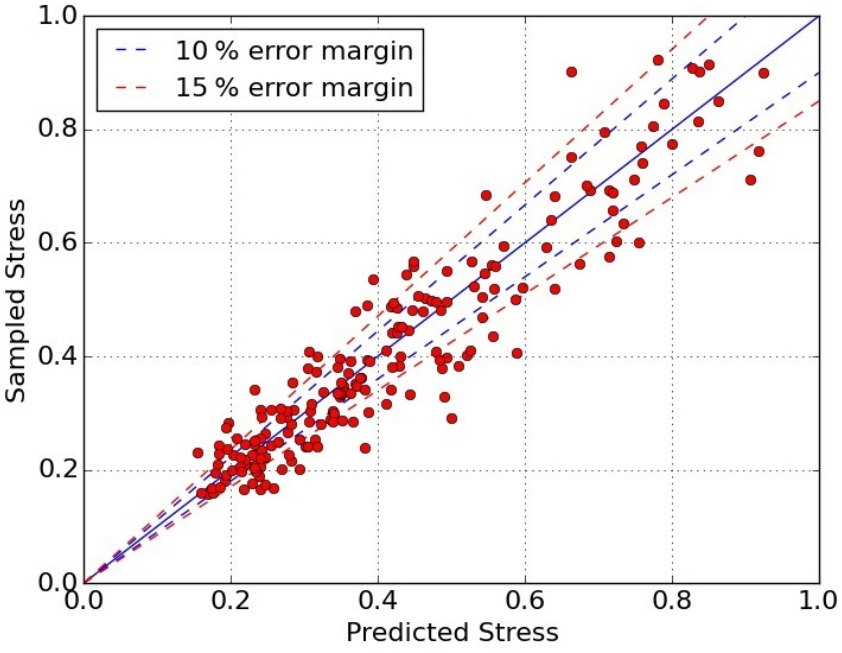

Figure 3.14: Sampled vs predicted results for less accurate fit: $R^2 = 0.9486$

In cases where testing data is too expensive to acquire, the performance measures described here may also be implemented using the training data itself. A drawback of this method is that it may lead to an over-estimation of the performance of a model as the performance measures are not independent of the data used to train the models. These values will in effect only measure how well the model fits the training data, instead of giving a true representation of the model's performance at new data points that lie outside the training set. A simplified example of this would be a case where three data points are used to train a one-dimensional quadratic model. If the error for this model was calculated based on the training data, it would always be zero percent, regardless of how well the model actually performs.

These factors may be mitigated by using the cross validation techniques described earlier in this section or by making use of adjusted R-square values. The adjusted R-squared is calculated from

$$R^2_{adj} = 1 - \left(\frac{n-1}{n-p}\right)\left(1 - R^2\right) \tag{3.22}$$

where n is the number of sample points used and p is the number of terms in the model. When a significant difference is observed between the R-squared and adjusted R-squared values, it gives an indication that non-significant terms may be included and that the model is over-fitting the data (Myers *et al.*, 2009).

Chapter 4

Procedure and implementation

4.1 Procedure

The goal of this study was to build a meta-model, based on FE analysis results, which will predict the structural behaviour of a plug type header box. The plan for constructing this meta-model was to fit a mathematical regression model, such as a response surface, to a discrete set of data points in order to produce a continuous prediction of the header box's structural behaviour, for any point in the design space.

To set up this meta-model, an adequate amount of FE results had to be generated to create the data set with which to train the meta-model. In order for each data point to be generated, a FE model had to be set up, simulated and have its results processed. Due to the large number data points that would be required for the meta-model in this study, it was not practical to repeat this sequence manually and an automated process had to be developed to perform these steps. In the section that follows, each part of the overall procedure, from setting up the FE simulation to collecting and processing the results, will be discussed in further detail.

4.2 Automation

To make the description that follows easier to understand, a schematic of the tasks performed by the automation tool set is shown in Figure 4.1.

The process starts by setting up a parametric CAD model of the structure to be simulated using Siemens NX 10.0 (Siemens, 2017). Each parameter or dimension is linked to a variable in the program that can be altered in order to modify the size of the structure. NX allows for this CAD model to be directly linked to its FE analysis software, where a FE model is set up to incorporate all the required detail mentioned in Section 2.3.

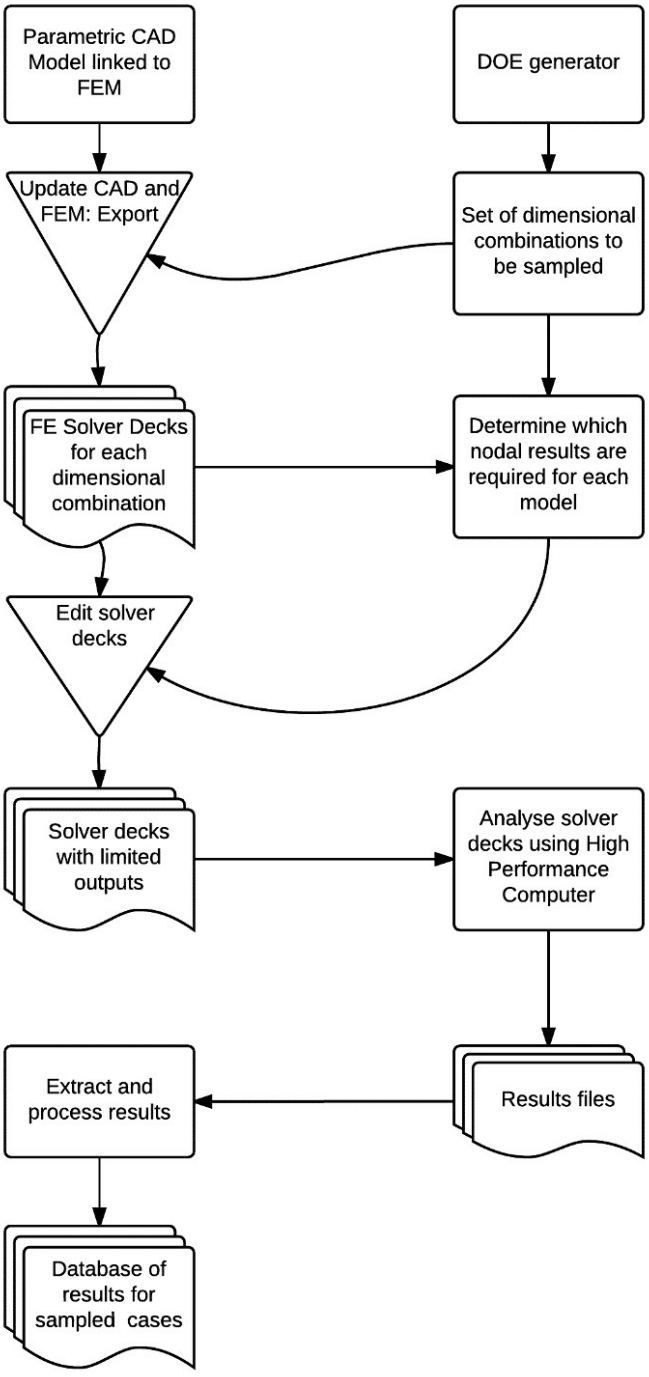

Figure 4.1: Flow chart of automation process

Parallel to this step a Python script generates the required DOE sample points that will be tested, in order to create the data from which to construct a meta-model. The DOE is based on LHC sampling and each sample point consists of a set of dimensions which corresponds to the parametric variables in the CAD model.

Another Python script, executed within the NX software environment, loads the DOE set and, for each sample point, applies the parametric dimensions to the CAD model and updates the FE model accordingly. This update completely re-meshes the structure according to its new dimensions while retaining the original loading and boundary conditions. It also retains any meshing preferences from the initial FE model, such as mesh seeding at the SCL positions. Upon completion of each FE model update, the script exports a Nastran solver deck for that model, with a unique file name, to be analysed at a later stage.

Based on the dimensions of each sample case and the mesh information of its corresponding solver deck, a new Python script determines exactly which nodal results will be required in order to later calculate the linearised stresses which are to be modelled. It then modifies the solver decks so that only the necessary nodal results are printed to the output file when they are solved. This step vastly reduces the time required for the subsequent post processing of the results and plays a significant role in managing the practical aspect of reducing the storage space required to save the results.

Due to the large number of FE models being considered, it is not practical to analyse the solver decks on a standard computer. Instead, the solver decks are processed using a high performance computer where they can be analysed in parallel. University of Stellenbosch's HPC1 (University of Stellenbosch, 2017) and the Centre for High Performance Computing's Lengau (Centre for High Performance Computing, 2017) were used for this purpose.

Finally, a Python script reads each results file and calculates the relevant linearised stresses for each load case. This process involves sorting the nodal results into groups, depending on which SCL they are associated with and arranging them in the correct order through the thickness of the plate or nozzle before performing the mathematical calculations described in Section 2.3. The linearised individual membrane and membrane plus bending stress components are then exported to be used as training and testing data for the meta-models.

With these procedures in place, the process of generating numerical data is greatly simplified and allows the user to construct larger and more complex FE models than would otherwise have been possible. The tools have also been created in such a way that they can be used to analyse any structure, and not only plug type header boxes, thus allowing them to be employed in future studies of other structures as well.

Chapter 5

Initial test problem

The first overall meta-model to be considered will focus on modelling the structural behaviour at the intersection where a nozzle meets the side plate of a plug type header box. The design of this part of a header box is not covered by Division 1 of the ASME code. Designers usually rely on a FE analysis to validate their own hand calculation designs, leaving little room for optimisation in the process. Having a meta-model that predicts the stresses in this area will allow the designer to first search for an optimum design before performing a final FE analysis for validation.

5.1 FE Model setup

Two separate FE models are discussed in this chapter. The first, shown in Figure 5.1a and 5.1b, consists of a large flat plate with a nozzle in the centre. This FE model was created as a simplified test case, with only a limited number of dimensions to be varied. Its purpose was to test the process and tool set used to construct a meta-model and to provide a platform where any errors could be corrected, before moving on to more complex models.

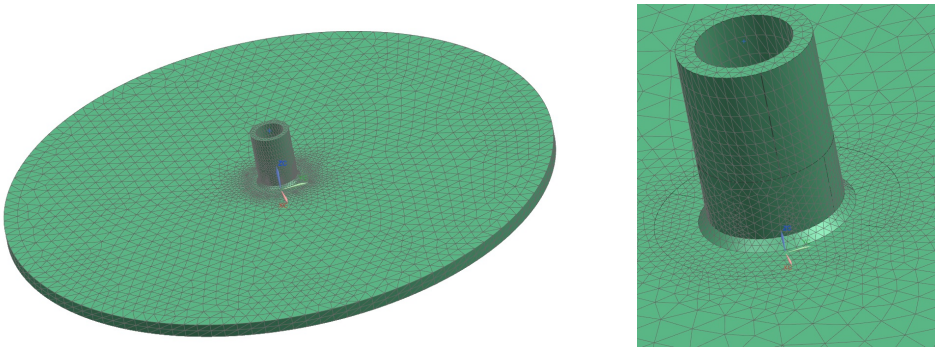

(a) Large flat plate and nozzle

(b) Nozzle close up

Figure 5.1: Mesh detail

The area of interest for this FE model lay around the base of the nozzle where it connects to the flat plate. This area was meshed in finer detail, while the surrounding mesh was made coarse to reduce the computational expense of the FE model. Specific attention was paid to the mesh around the base of the nozzle, seen in Figure 5.2a, to ensure that there were enough nodes in the areas where results are to be extracted. The red lines in Figure 5.2b show exactly where the stress results were extracted. The minimum number of through thickness second order elements along these lines was set to five. This number was chosen based on the results of a mesh sensitivity study that was performed on a representative FE model. The details regarding stress extraction and why these lines are necessary are discussed in Section 2.3.2. The figures also show how the FE model has been segmented to allow for stress extraction at 8 equally spaced points around the circumference of the nozzle junction. The boundary condition applied to this FE model is a simply supported constraint around the outer edge of the plate.

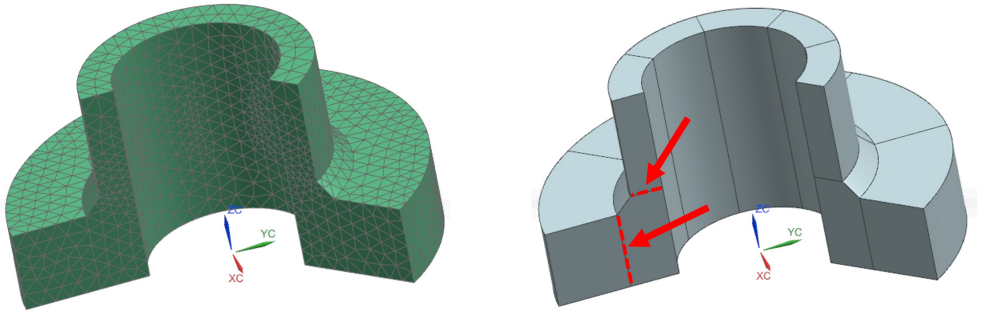

(a) Mesh detail (b) FE model detail and SCL positioning

Figure 5.2: Segmented design at nozzle intersection to allow for SCL positioning

The second FE model, seen in Figure 5.3a and Figure 5.3b, was created to more accurately simulate the boundary conditions that a nozzle would experience as part of a plug type header box. It has seven dimensions that can be varied. These are the nozzle diameter, nozzle thickness, nozzle length, box height, box length and the thicknesses of the two sets of opposing box sides. Each set of parallel sides on the box has the same thickness. The width of the box was not chosen as an independent variable, but was coupled to the diameter of the nozzle. The width of the box is fixed so that the outer edge of the nozzle weld is always in vertical alignment with the inner edge of the box's weld. Thus the box's width is kept as small as possible without having the nozzle and box's welds overlap one another. Further details of the exact dimensions of the box are provided in the Section 5.2.

In this FE model the ends of the box are held with fixed constraints in order to approximate the stiffening effect of a header box's end plates. The same detailed and segmented meshing pattern described for the first FE model was replicated around the base of the nozzle.

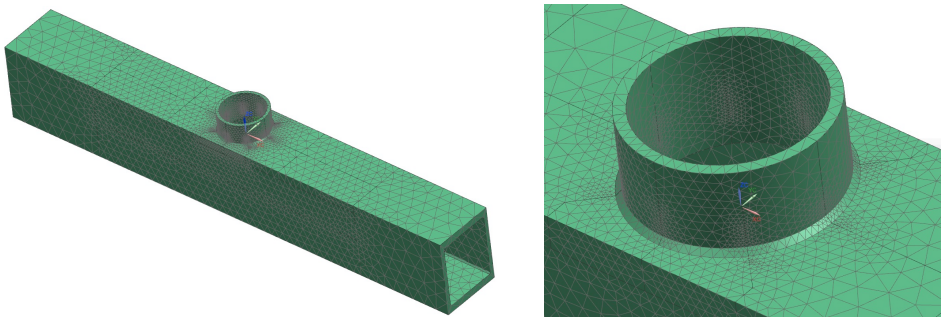

(a) Box shell and nozzle (b) Nozzle close up

Figure 5.3: Box detail

The two sets of loads that were considered are pressure loads and nozzle loads. Pressure loads were applied to the areas that would form part of the inside of the box. This load is also accompanied by an equivalent force, known as the 'pressure force', which was applied to the top face of the nozzle, in order to account for the effect of having the nozzle connected to a pressurised piping system. This force was applied in line with the axis of the nozzle and acts to pull the nozzle away from the flat plate. The magnitude of this force is calculated using

$$Force = \frac{\pi \times (Internal\ Nozzle\ Diameter)^2}{4} \times InternalPressure \qquad (5.1)$$

Nozzle loads were applied as shown in Figure 5.4, where, F_x, F_y and F_z represent forces applied to the top face of the nozzle and M_x, M_y and M_z moments applied to the top of the nozzle. In the numerical simulations, each of these loads were applied as separate load cases so that the results could be analysed individually and combined as necessary during post processing.

Due to the fact that header boxes operate at elevated temperatures, thermal loading should be taken into account where applicable. For the single chamber header boxes under consideration in this study, these thermal stresses do however not play a role as there is no significant thermal gradient present in the structure. The complete form of these header boxes are also mounted as floating structures thus allowing them to expand freely as they with any rise or fall in temperature.

An isotropic material with a Poisson's ratio of 0.3, as dictated by the ASME guidelines, was used for this and all the remaining FE models, unless otherwise specified. While it is customary to also state the Young's Modulus used when reporting on FE analyses it is not necessary in the case of this study. Several tests that were performed, all of which confirmed that the stress results produced by the FE models in this study are invariant of the Young' Modulus value used. This is an advantageous feature of the meta-model being constructed which means that the results hold true for any material operating within its linear elastic region.

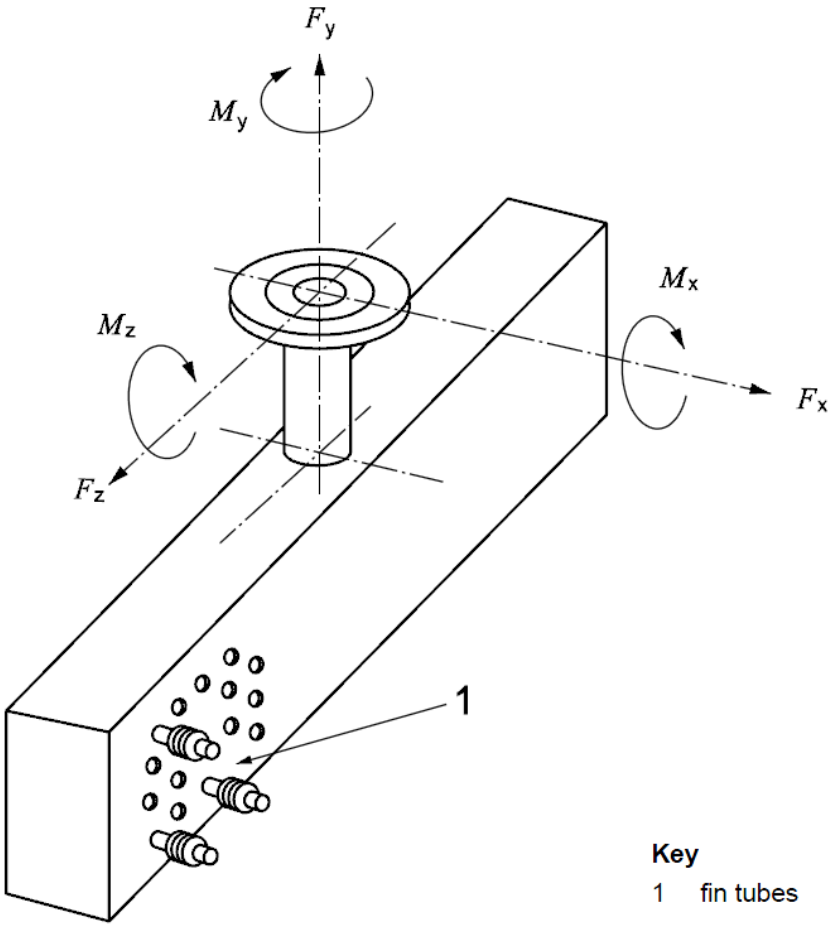

Figure 5.4: API 661 nozzle loading (API, 2013)

As the first model described in this section was only created to test the software tools used in the initial steps of setting up a FE model and using it to generate training data for constructing a meta-model, no further details about this FE model are pertinent. As such, the descriptions in Section 5.2

and 5.3 will focus on the second FE model described here, which will be used to construct a meta-model.

5.2 Design space

Taking into account the computational resources available, it was decided that a set of 2500 test cases would be sampled. To maximise efficacy of the data points when fitting mathematical models, the size of the design space had to be reduced as far as possible to increase the sampling density. This was done by screening out redundant areas in the global design space, based on known non-dimensional ratios and design limitations for plug type header boxes. Further design space reductions were implemented to limit the design space to the region of available construction materials and to ensure that the parametric CAD model did not collapse onto itself due to incompatible dimensional combinations.

The bounds of the final design space are given in Table 5.1. A further illustration of the variables is given in Figure 5.5. The variable $x7$, which appears in the table but not in the figure represents the length of the box. The size of the welds, w, was fixed at 10 mm.

Table 5.1: Design space description

Inequality/Equation	Practical description
$100\text{ mm} \leq x1 \leq 270\text{ mm}$	The nozzle outer diameter may vary between 100 mm and 270 mm
$20\text{ mm} \leq x2 \leq 70\text{ mm}$	The thickness of the two plates orientated perpendicular to the nozzle (called the side plates) may vary between 20 mm and 70 mm
$\frac{1}{2.5} \leq \frac{x3}{x1+4w} \leq 2.5$	The inside height of the box may not be less than 2.5 times smaller than the box's inside width and may not be larger than 2.5 times the box's width
$\frac{1}{2} \leq \frac{x4}{x2} \leq 2$	The thickness of the two plates parallel to the nozzle (plug and tube sheet) may not be smaller than half the side plates' thickness and may not be larger than two times the side plates' thickness
$20\text{ mm} \leq x4 \leq 80\text{ mm}$	The thickness of the two plates parallel to the nozzle may vary between 20 mm and 80 mm

$\frac{1}{16a} \leq \frac{x5}{x1} \leq \frac{1}{4a}$ $a = \frac{150 + x1}{210}$	The nozzle thickness may not be more than $16a$ times smaller than the outer diameter of the nozzle and may not be larger than $4a$ times smaller than the nozzle's outer diameter. a is a scaling factor that varies between 1.2 and 2. It has a value of 1.2 when the nozzle outer diameter is equal to 100 mm and increases linearly to 2 when the nozzle outer diameter is equal to 270 mm. This scaling is applied to keep the design space within the bounds of commonly manufactured nozzle sizes
$x5 \geq x2$	The thickness of the nozzle may not exceed the thickness of the side plate
100 mm $\leq x6 \leq$ 350 mm	The nozzle length may vary between 100 mm and 350 mm
$max(3, b) \leq \frac{x7}{x1} \leq 10$ $b = \frac{x1 + 4w + 2(x4) + 80 \text{ mm}}{x1}$	The length of the box may be between three and ten times larger than the outer diameter of the nozzle, except when b is larger than three, in which case it becomes the new limiting factor. (This exception is implemented under certain conditions to prevent the CAD model from collapsing due to the formation of overlapping features)

5.3 Simulation and modelling

To build a meta-model which predicts the equivalent linearised stresses in this structure, mathematical models were fit to each of the 1344 stress component sets contained within the larger pool of sampled results. This number originates from the fact that there are 16 SCLs, which each yield 12 linearised stress component results, 6 for membrane stress and 6 for membrane plus bending stress, and there are 7 load cases being considered. In order to combine the results of two or more load cases it is necessary to sum together the individual

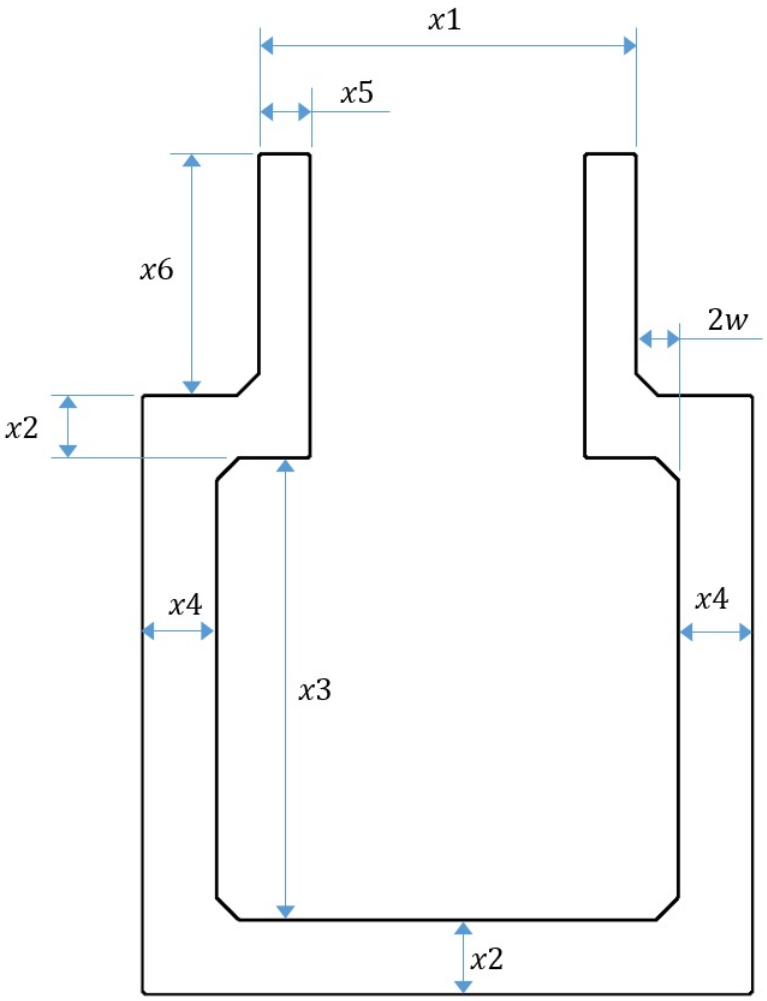

Figure 5.5: Cross-section of parametric FE model

stress components of the relevant load cases. These values can then be used to calculate a new set of equivalent von Mises stresses for the combination. This is why it is necessary to model each of the 1344 individual stress components, rather than only modelling the equivalent von Mises membrane and membrane plus bending stress for each load case, of which there are only 224.

Based on the large number of models that had to be created in each case, it was decided to use a response surfaces (RS) to approximate the data, as these models are computationally inexpensive to fit (a detailed discussion surrounding this decision is given in Section 8.3). As it was intended to attempt fitting 4^{th} and 5^{th} order RS models, whose solution matrices are often rank deficient, it was decided to solve the least squares regression using the SVD method described in Section 3.2.1 (more details about this decision is given later in this section).

An attempt was made to reduce the order of the RS required to fit the data by means of using intermediate variables, otherwise known as scaling (Myers *et al.*, 2009). This was done by attempting to raise the values used for various parameters to a higher power and then testing whether a lower order RS would fit the data better than before. To illustrate this concept simply, consider a model with only one parameter, x, which is approximated well only by a 4^{th} order polynomial or higher. If, instead of using x as a parameter, an intermediate variable x^2 is used, it may be possible that a 2^{nd} or 3^{rd} order polynomial now approximates the model equally well. After much trial and error however, no intermediate variables were found that allowed for lower order RS to be used. It was thus decided to carry on with the 4^{th} and 5^{th} order models.

Careful consideration was given to the risks of over fitting when using these high order RS models. These risks were mitigated by having a minimum of three times more training points than model variables, in the case of the 5^{th} order fit, and by having a large independent testing set comprised of 15 % the size of the training set, with which to confirm the accuracy of the models.

LHC sampling was chosen as the DOE method. To ensure a somewhat optimized Latin hypercube design with a low level of correlation between the sampled points, 10 000 Latin Hypercube samples, each containing 2500 points, were generated and the one with the lowest correlation between its points was chosen as the set of 2500 points to be sampled. The data from these samples was used as the training data. Using the same approach, an additional set of 375 sample points were also generated to be used as an independent testing set. All the sample points were simulated using the procedure described in Chapter 4.

Where possible, non-dimensional parameters were used when fitting the RS surface models. Including these non-dimensional parameters as opposed to only using the standard dimensions of the box resulted in a noteworthy performance improvement of the RS models that were fit. For example, the best R-squared value attained for the *Pressure* load case was improved from 0.9339 to 0.9716 (the overall results will be discussed below). Several attempts were made to non-dimensionalise the remaining parameters, but no further useful non-dimensional entities could be found. A summary of the seven parameters used is given in Table 5.2.

Table 5.2: Design parameter

Parameter	Description
$x1$	Nozzle outer diameter
$x2$	Side plate thickness
$\frac{x3}{x1+4w}$	Box inner height over inner width
$\frac{x4}{x2}$	Plug and tube sheet thickness over side plate thickness
$\frac{x5}{x1}$	Nozzle thickness over nozzle outer diameter
$x6$	Nozzle length
$x7$	Box length

The performance results for the models that were fit are shown in Table 5.3. The table shows the R-squared values based on the testing set, grouped by load case, for the equivalent von Mises stress result predictions calculated using the results of the 1344 sub-models. This was done as it is not practical to present the result for all 1344 data fits and because the von Mises values are the results that the meta-model will finally yield, thus making them a better measure of the model's performance.

Table 5.3: R-squared values based on testing set

Load case	SVD Regression 1	SVD Regression 2	Combined Model
		3^{rd} order models	
Pressure	0.8388	0.8388	0.8388
F_x	0.9815	0.9815	0.9815
F_y	0.9927	0.9927	0.9927
F_z	0.9818	0.9818	0.9818
M_x	0.9810	0.9810	0.9810
M_y	0.9507	0.9507	0.9507
M_z	0.9807	0.9807	0.9807

		4^{th} order models	
Pressure	0.9399	0.9400	0.9404
F_x	0.9927	0.9926	**0.9927**
F_y	0.9951	0.9948	**0.9951**
F_z	0.9932	0.9931	**0.9932**
M_x	0.9932	0.9925	**0.9932**
M_y	0.9915	0.9892	0.9915
M_z	0.9928	0.9923	**0.9928**
		5^{th} order models	
Pressure	0.9403	0.9698	**0.9716**
F_x	0.9857	0.9893	0.9908
F_y	0.9880	0.9920	0.9930
F_z	0.9856	0.9903	0.9909
M_x	0.9867	0.9836	0.9892
M_y	0.9926	0.9713	**0.9944**
M_z	0.9866	0.9823	0.9885

For all of the load case models, three sets of R-squared values are presented. The first two sets are the performance values attained from two separate regression analyses performed using the SVD method. The difference of the two analyses are described below.

When fitting higher order models, the solution matrix, $\mathbf{X}$, often does not satisfy the full rank assumption. When the full rank assumption is not satisfied, $\mathbf{X}^T\mathbf{X}$ becomes singular and can thus not be inverted, directly or indirectly (Lin, 2006). In such cases SVD regression techniques can be used to train a model, in spite of rank deficiency.

The rank of a matrix is determined by the number of non-zero singular values associated with it. Varying the tolerance of what constitutes a non-zero singular value, taking into account machine precision and the scaling of the solution matrix, will thus accordingly influence the rank of a matrix. In

the case of a SVD regression, this will influence the size of the portion of the **U**, **V** and **S** matrices that are employed as part of the calculations (refer to Section 3.2.1) and in turn possibly influence the quality of the models being fit. In this study, two tolerance values were tested. The point at which a singular value is deemed effectively equal to zero, for the 1^{st} SVD regression analysis, was taken as 2^{-53} times the largest singular value. For the 2^{nd} SVD regression analysis, this limit was taken as 2^{-52} times the largest singular value times the largest of, the number of rows or columns. These were default recommended tolerance values of two software packages used as part of the regression calculations (the value of performing these two separate regression analyses is discussed in detail in Chapter 8).

The third set of performance values shown for each load case is for a combination of the models produced by the above two methods, comprising of only the best performing components of each. To assemble this combined case, the 1344 sub-models for each of the two model fitting methods were compared one by one and only the best performing models were then used in the von Mises stress calculations on which the R-squared values in this table are based. The underlined values indicate the overall best performing model in each load case.

From the results, we can see that both the 4^{th} and 5^{th} order RS models approximate the data well. In some cases it can also be seen that the 4^{th} order RS models outperform the 5^{th} order models. If the performance values had been based on the training data only, this would not have been possible, as a higher order model would necessarily have produced a higher R-squared performance value. Because these performance results are however based on an independent test set, we are able to analyse these results and recognise that in these cases, where the 4^{th} order models outperform the 5^{th} order model, the 5^{th} order models are over fitting the data.

The final meta-model was constructed using the 5^{th} order combined model to predict stresses for the *Pressure* and M_y load cases and the 4^{th} order combined model as a predictor for the remaining load cases. To visually represent the accuracy of the overall meta-model, Figures 5.6 and 5.7 show plots of the best and worst performing components of the model. Each plot shows how well the model was able to predict the sampled results of the independent testing set, for a given load case. In these plots, the closer the points lie to the 45° line in the middle of the graph, the more accurate the predictions are. Points lying below the 45° line represent a conservative prediction by the model, while points above this line are unconservative predictions. In each plot, there are 12 000 points being displayed as a 96 % transparent dot, in order for densely populated areas to be more apparent. The blue and red dashed lines represent

the 10 % and 15 % error margins respectively. The comparison plots for the remaining five load cases are given in Appendix A.

It is valuable to note here that even though the points in Figure 5.6 appear widely spread, only 1.63 % of the data yields unconservative predictions with an error margin of more than 15 %, while the vast majority of the data is concentrated on or around the 45° line.

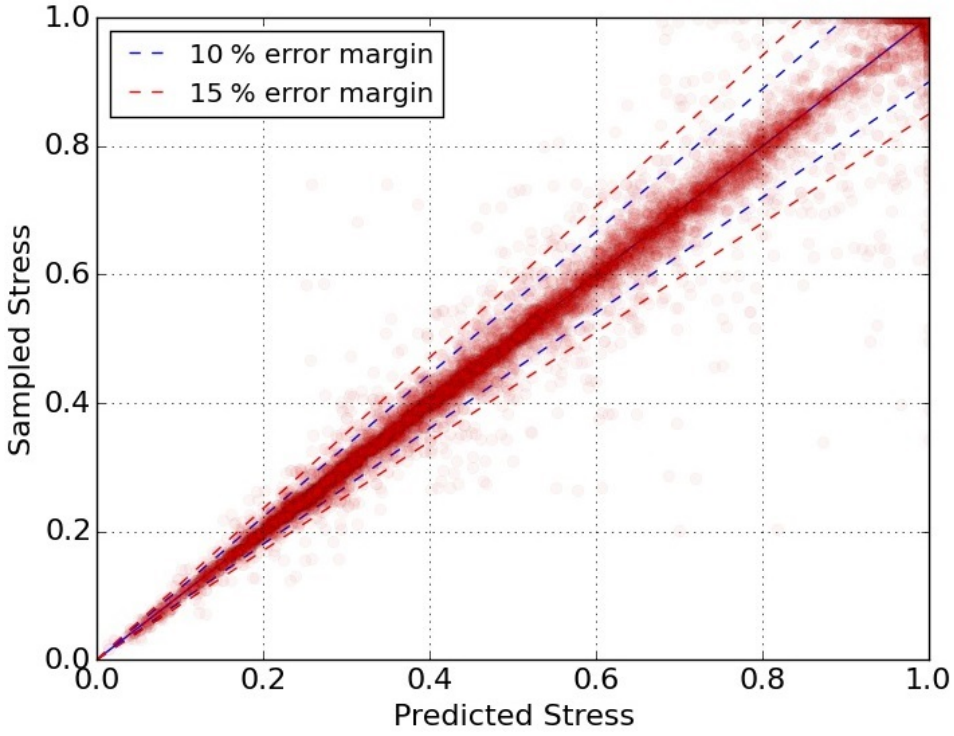

Figure 5.6: Lowest scoring model based on testing set: $R^2 = 0.9716$

5.4 Graphical user interface

To make the results of the meta-model more accessible, a graphical user interface (GUI) was created with which to select model inputs and request result outputs. The layout of this GUI is shown in Figure 5.8. The top half of the interface focuses on allowing the user to extract results for a specific design case with fixed dimensions and loads. On the left-hand side of this part, each slider controls a dimension that can be varied in the meta-model. On the right-hand side, the components of the load case and the allowable stresses can be specified. From here a graph can be generated in real time to show the predicted stresses at each of the stress extraction points around the nozzle.

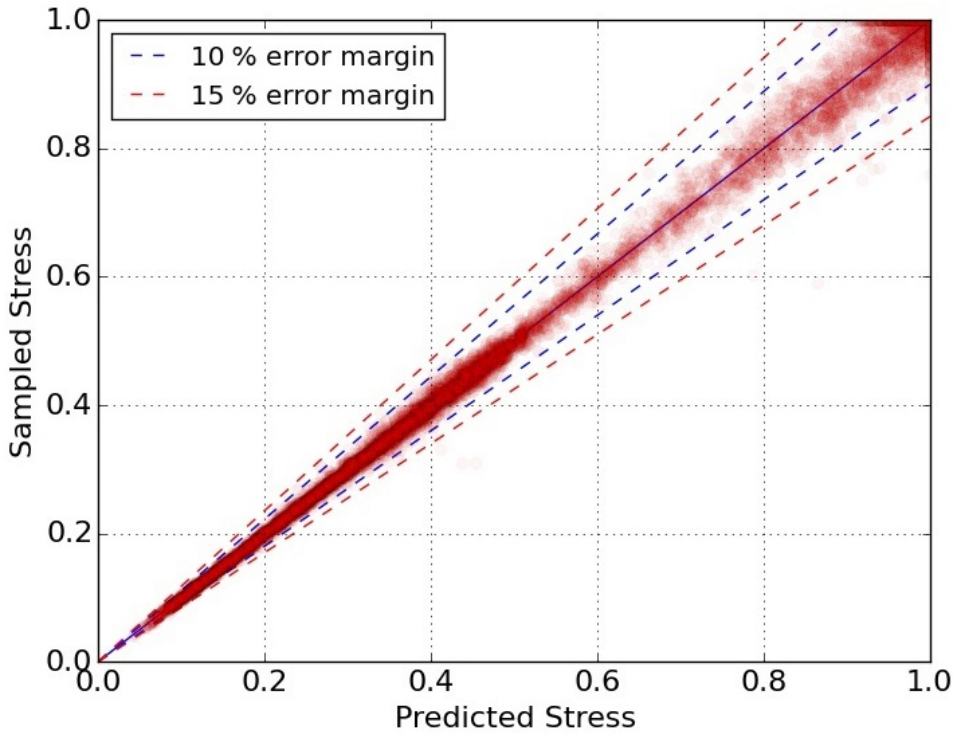

Figure 5.7: Highest scoring model based on testing set: $R^2 = 0.9951$

The lower half of the interface allows the user to go further and study what the overall effect would be of changing individual dimensions. Using the sliders here, the users can set up a new combination of dimensions which are different from the set above and then request a graph of how the stress values change, as the dimensions morph from the first set to the second. Examples of result plots mentioned here are shown in the following section. An important element that is incorporated into this GUI is that it only allows the user to predict results for designs that lie within the design space of the meta-model that was tested, as any extrapolation of the results, especially with the high order RS models being used, can lead to significant error.

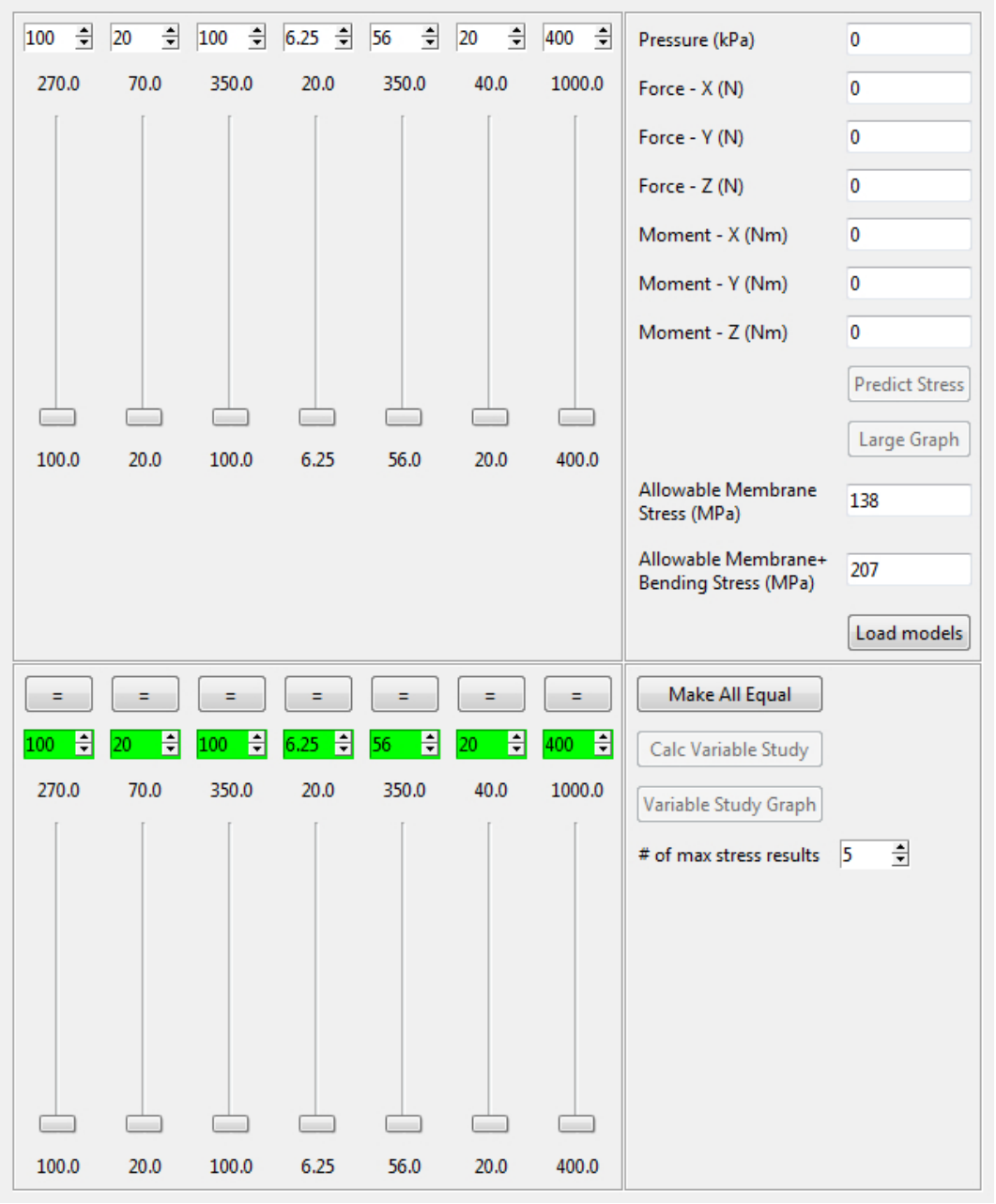

Figure 5.8: Meta-model post processing GUI

5.5 Results

Although the first model was only intended to be used to test the process of constructing a meta-model, it did produce some interesting results. By adding a number of additional stress extraction points at intervals further away from the nozzle junction, the plot in Figure 5.9 was produced. This plot makes it possible to visualise the decay of bending stress in a flat plate as one moves away from a nozzle to which an external load is applied. The results are

for the load case when only the force F_x was applied. Each bar represents the results from one of the eight segments around the perimeter of the nozzle. The left hand side of each bar shows the bending stress at the base of the nozzle junction and moving from left to right, they show how the stress values decay with increasing distance from the nozzle. The solid blue lines are sine curves that were fit to the results, with which it is possible to interpolate between the segments.

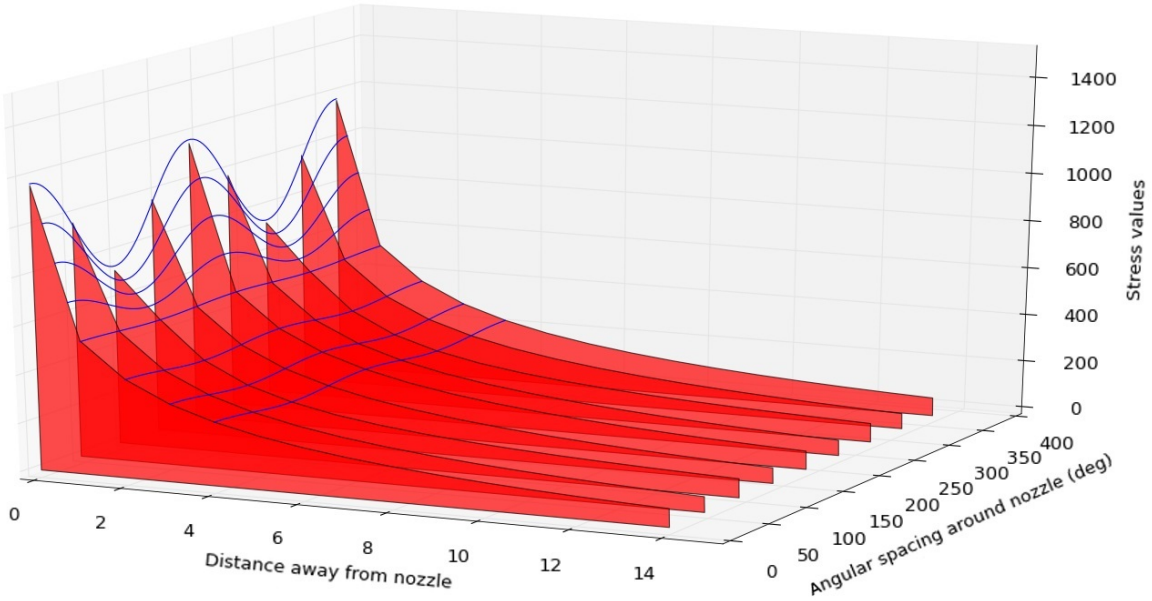

Figure 5.9: Bending stress distribution in flat plate

Looking at the results from the second model, Figure 5.10 shows an example of a stress prediction plot that can be generated by the meta-model created in this study. In the first plot, the eight groupings shown along the x-axis correspond to the eight points around the nozzle where stresses are predicted. In each of these groupings, the four shaded bars show the predicted membrane and membrane plus bending stress in the flat plate and the nozzle. The dashed line in the graph shows the allowable limit for membrane stress and the solid line shows the allowable limit for membrane plus bending stress, as set by the user.

The results for the second part of the GUI's functionality take on a different form to those seen before. The purpose of these results is to show how the stresses around the nozzle junction change, as the dimensions of the header box are changed. Figures 5.11 and 5.12 show the results from two studies that were performed using the second part of the GUI. In these graphs, all the stress results are plotted on top of one another at twenty intervals between the

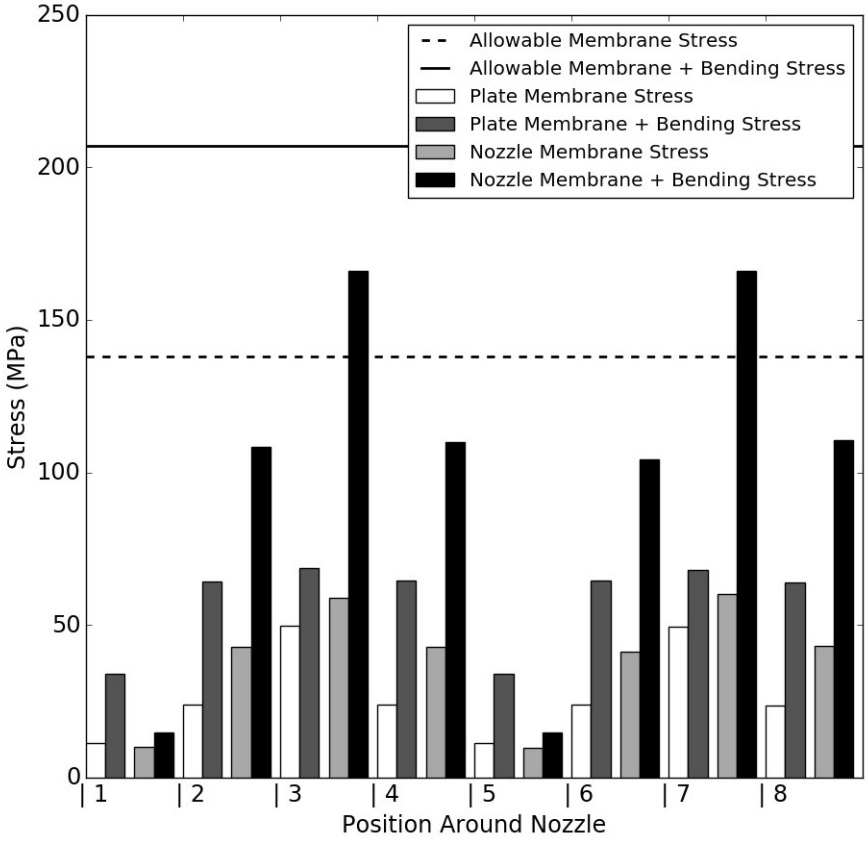

Figure 5.10: Sample result output

two points being considered. The results for each individual SCL is connected by a line across the twenty intervals. For the cases shown, only the results for the six SCLs showing the highest stress predictions have been plotted, to avoid confusion and unnecessary clutter on the graph. This number can be controlled by the user from the GUI.

Figure 5.11 shows the results for a design case where all the dimensions of the FE model were kept constant, except for the length of the nozzle which was varied. The same procedure was followed for Figure 5.12, only here, the height of the box between the nozzle and the bottom plate was varied. The results show how the critical stresses at the nozzle junction do not always vary monotonically up or down, as may have been expected, for the linear up or downward variation of a single dimension of the header box. Furthermore, the results show that the point at which the highest stress occurs may shift from one position to another, depending on the dimensions of the box. This is seen by the fact that the maximum stresses do not always occur along a single line that follows the results for a specific SCL, but passes from one line to another. By using such results, a user is able to consider the macro effects that changing the dimensions of the header box will have on the nozzle junction. Users can

thus easily identify favourable design regions where optimal header box designs are likely to occur.

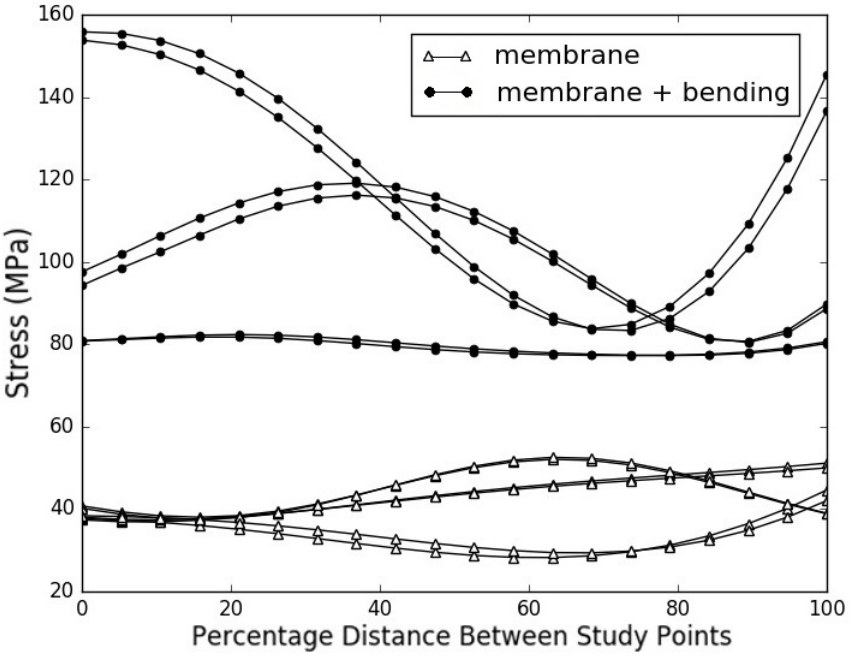

Figure 5.11: Stress variation with nozzle length change

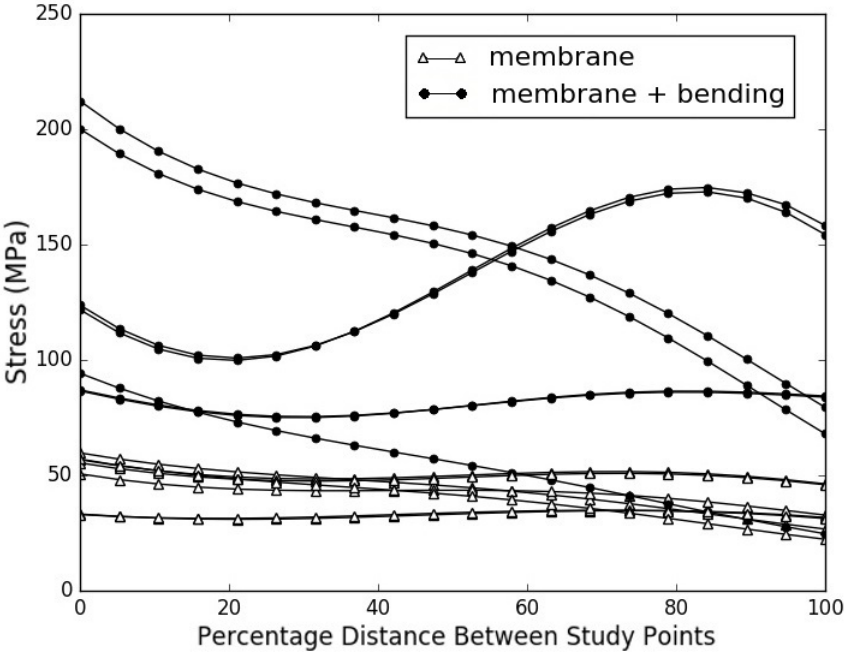

Figure 5.12: Stress variation with box height change

Chapter 6

Partial header box model

A second overall meta-model was constructed to study the stresses in the body of the box around the region where a nozzle is attached. As discussed in Section 2.2, the body of a plug type header box (without the end plates) is designed based on the guidelines set out in Appendix 13 of ASME VIII Division 1. In this appendix, the designer selects the relevant cross-sectional profile corresponding to the header box being designed and the accompanying equations are used to calculate the stresses in the sides of the box. In cases where one or more of the sides of the header box are perforated, to allow for piping and nozzle connections, a ligament efficiency factor is introduced and applied to reduce the allowable stress value for the relevant side to compensate for the weakened state of the plate.

A weakness of this method is that it does not adjust the allowable stress for the components adjacent to the weakened member in order to compensate for the fact that these members will be experiencing a different set of loads. In the same way, the allowable stress values for adjacent members are also not adjusted in cases where a plate is strengthened. These disregarded effects are however particularly relevant when designing a header box with a nozzle.

Traditionally in the South African design environment, a nozzle which is not reinforced using compensation material is considered to be a component that structurally weakens the side plate of a header box. As such a ligament efficiency factor is calculated for this plate and applied, which lowers its allowable stress values. The header box inlet/outlet nozzle size most frequently used for plug type header boxes, however, falls outside the guidelines given by the ASME code for calculating an appropriate ligament efficiency. A South African industry accepted norm has become to use a ligament efficiency factor of 0.5 in such cases, effectively halving the allowable stress for the relevant plate.

Depending on its placement, diameter and wall thickness, a nozzle may however act to weaken or strengthen the side plate of a header box. In doing

so, it may affect the components adjacent to it and have the opposite of the anticipated weakening effect on the side plate of the box. Until now, there has been no way to quantify these effects.

In this chapter, three meta-models are constructed, focusing on the study of these effects. All three meta-models are based on the same CAD model, but each one has a different number of input variables that can be controlled, thus varying their complexity and the number of simulated sample points required to construct and test them.

6.1 FE model set up

The geometry of the FE model is identical in shape to that of the previous chapter, but was constructed in such a way that more detailed stress results could be extracted from the body of the box. Figure 6.1 shows the CAD model of the pressure vessel and Figure 6.2 shows the box when meshed. The lines on the CAD part show where the structure has been divided in correspondence with the positions of the SCLs. This allows for more detailed mesh control in the areas where stresses are extracted.

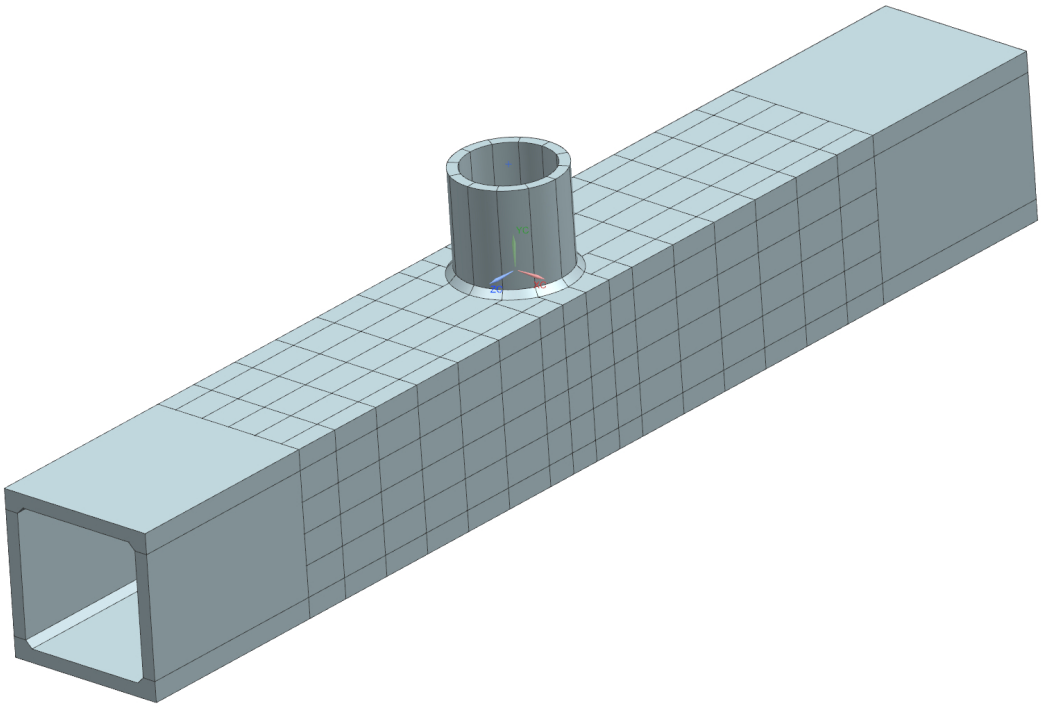

Figure 6.1: CAD layout for new FE model

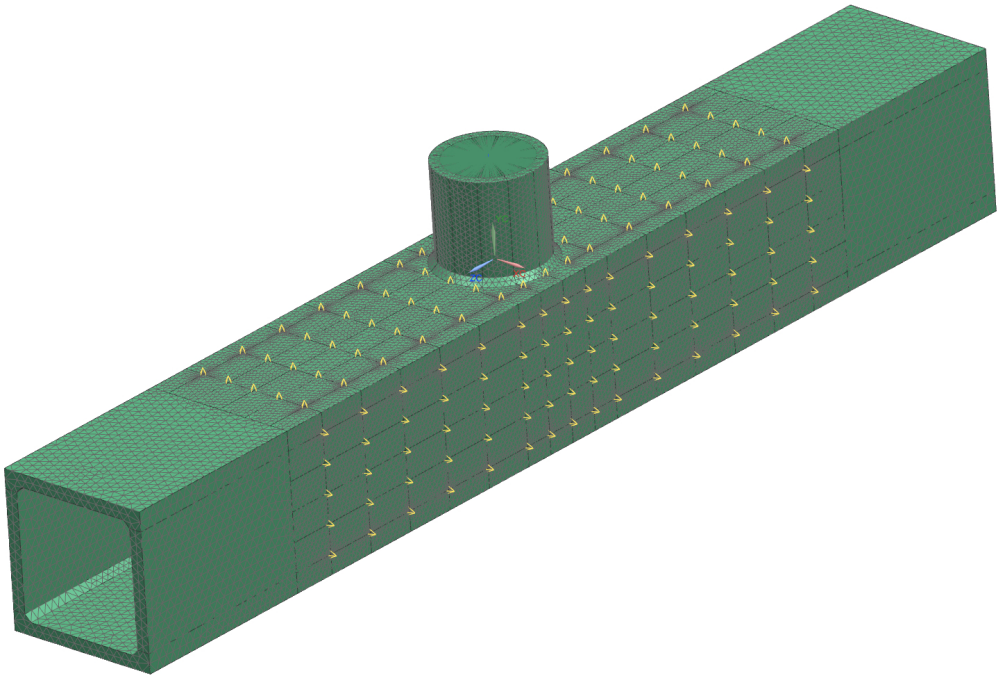

Figure 6.2: Mesh and SCL placement

This FE model has 291 new SCLs, which replace the 16 SCLs from the previous FE model in Chapter 5. Their positions are shown by the yellow pointers in Figure 6.2. These new SCLs are laid out such that each one lies on one of the twenty stress classification planes (SCP) that span the middle section of the box, running past the nozzle, as shown in Figure 6.3.

This layout makes it possible for the user to track the stress at a particular position on the cross-section of the box, along the length of the box, as it moves past the position of the nozzle. The SCLs were concentrated around the central region of the box, as the focus of this model was only to classify the effect that a nozzle has on the stresses already existing in the body of a header box pressure vessel. In other words, the purpose of this model was not to predict the overall stresses that would occur in a given flat sided pressure vessel, but rather to show how the stresses already present are influenced by the presence of a nozzle on a given box.

To ensure that the central section of the box where the stresses are extracted would always be large enough to capture the relevant results, its size was scaled proportionally to the diameter of the nozzle. The central section of the box was set to reach three diameter widths to either side of the nozzle. Past this point, an additional section of box was added to each end of the structure to create a separation between the outer most points where results were extracted and the fixed boundary conditions that were placed at the ends of the box.

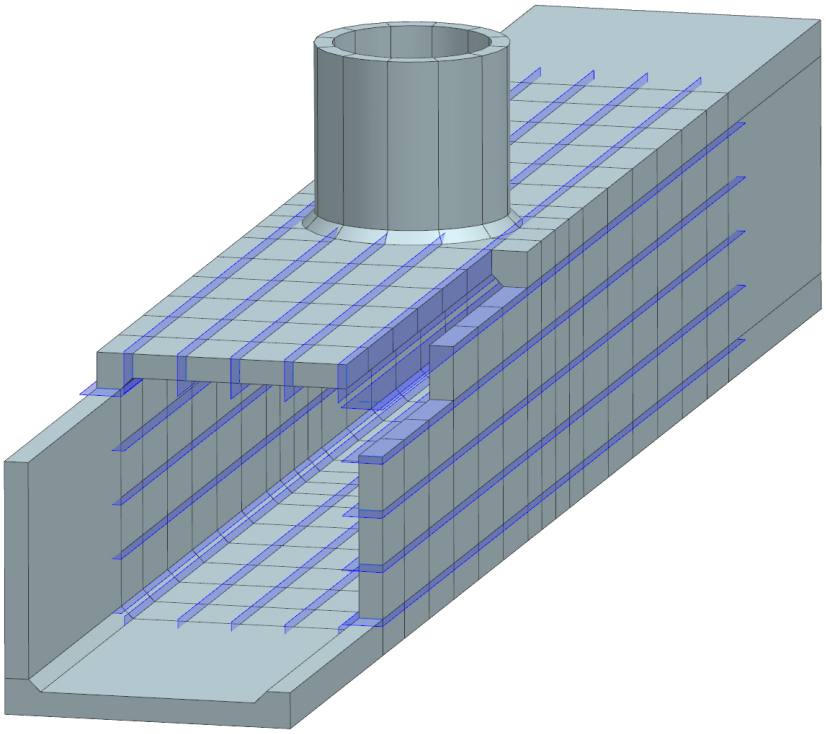

Figure 6.3: Stress classification plane positions

The length of these additional box section were set to 1.5 times the maximum of the box height or box width, after testing revealed that this distance would isolate the stress extraction points from any boundary condition interference.

It is useful to note at this point that the combination of the two dimensioning conditions described above mean that the overall length of the box will always be determined by a combination of the cross-sectional dimensions of the box. It is thus no longer an independent variable that can be varied like in the FE model from the previous chapter.

6.2 Design space

The FE model in this chapter was used to perform three sets of analyses, each having a different number of variables and producing a separate meta-model. For ease of reference, the cross-sectional schematic of the box is shown again in Figure 6.4 along with a description of the six design variables common to all three of the overall meta-models in Table 6.1.

Table 6.1: Design space description

Inequality/Equation	Practical description
$100 \text{ mm} \leq x1 \leq 270 \text{ mm}$	The nozzle outer diameter may vary between 100 mm and 270 mm
$20 \text{ mm} \leq x2 \leq 70 \text{ mm}$	The thickness of the two plates orientated perpendicular to the nozzle (called the side plates) may vary between 20 mm and 70 mm
$\frac{1}{1.2} \leq \frac{x3}{x1 + 4w} \leq 1.2$	The inside height of the box may not be less than 1.2 times smaller than the box's inside width and may not be larger than 1.2 times the box's width
$1 \leq \frac{x4}{x2} \leq 2$	The thickness of the two plates parallel to the nozzle (plug and tube sheet) may not be smaller than the side plates' thickness and may not be larger than two times the side plates' thickness
$20 \text{ mm} \leq x4 \leq 80 \text{ mm}$	The thickness of the two plates parallel to the nozzle may vary between 20 mm and 80 mm
$\frac{1}{16a} \leq \frac{x5}{x1} \leq \frac{1}{4a}$ $a = \frac{150 + x1}{210}$	The nozzle thickness may not be more than $16a$ times smaller than the outer diameter of the nozzle and may not be larger than $4a$ times smaller than the nozzle's outer diameter. a is a scaling factor that varies between 1.2 and 2. It has a value of 1.2 when the nozzle outer diameter is equal to 100 mm and increases linearly to 2 when the nozzle outer diameter is equal to 270 mm. This scaling is applied to keep the design space within the bounds of commonly manufactured nozzle sizes

$x5 \geq x2$	The thickness of the nozzle may not exceed the thickness of the side plate
100 mm $\leq x6 \leq$ 350 mm	The nozzle length may vary between 100 mm and 350 mm

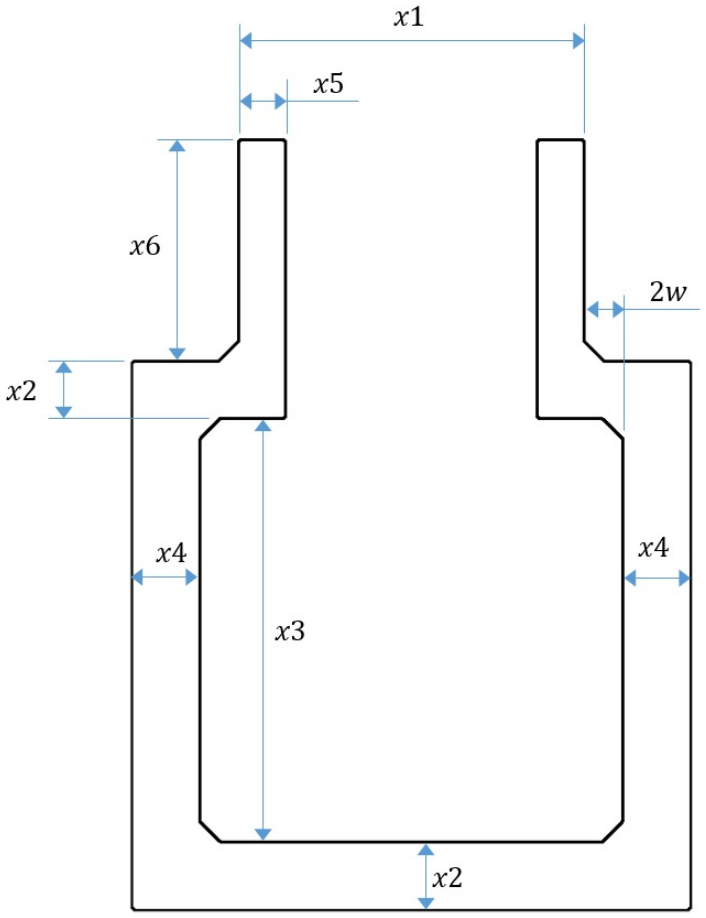

Figure 6.4: Cross-section of parametric FE model

While the new design space is largely similar to that of the first meta-model described in Chapter 5, there is a difference with the new bounds that govern the aspect ratio of the box, given by the ratio, $x3/(x1 + 4w)$. In this ratio $x3$ represents the height of the box and $(x1 + 4w)$, which is a combination of the nozzle outer diameter and weld size, represents the inside width of the box. Previously, this aspect ratio was allowed to vary between 1/2.5 and 2.5.

This meant the box could be up to 2.5 times wider than it was high and vice versa. After performing an initial set of analyses on the structure with the new SCLs positions, it was found that these large aspect ratios produced excessively high stresses in the corners of the box which completely thwarted any efforts of fitting response surfaces to the data. After consulting with the chief engineer at Kelvion Thermal Solutions, the study's industry partner, it was found that pressure vessels of this configuration very rarely have an aspect ratio greater that 1.2, except in cases where additional internal supports are added. The new aspect ratio bounds were thus set to 1/1.2 and 1.2, which produced favourable results.

Another design space boundary that was changed is the limits placed on the thickness of the plug and tube sheets, represented by $x4$, in relation to the thickness of the side plates, $x2$. The new bounds prevent the plug and tube sheets from being thinner than the side plates. This new design space bound was motivated by a manufacturing requirement described by Beyers *et al.* (2015). In short, if the plug or tube sheet of a header box is thinner than the side plates, the respective joints will need to be welded form the side of the plug or tube sheet. This causes a heat affected zone where the material is hardened in the region where the plug or tube holes need to be drilled. Consequently, the cost of drilling these holes increases as the bits break more often or become blunt sooner. The plug and tube sheets are thus prevented from being thinner than side plates so that the joint welds may be performed from the side plate end. An illustration of this concept is shown in Figure 6.5.

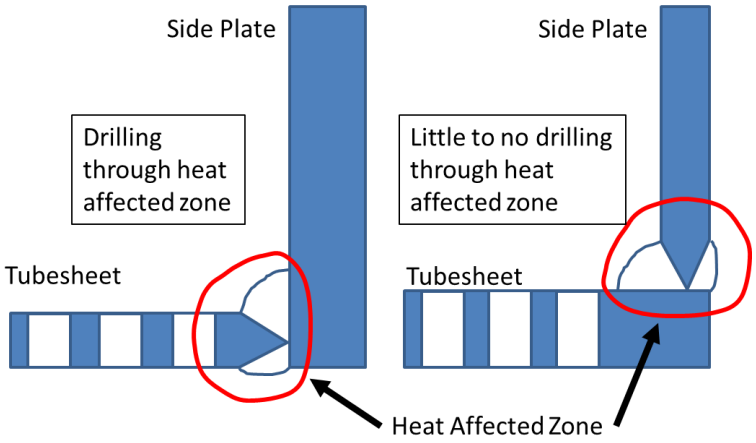

Figure 6.5: Welding related manufacturing constraints (Beyers *et al.*, 2015)

Table 6.2 provides further design space information about the additional variables that were used for the 2^{nd} and 3^{rd} overall meta-models in this chapter.

Table 6.2: Additional design space description

Inequality/Equation	Practical description
Meta-models set 2	
$0.4 \leq x7 \leq 0.6$	The equivalent Young's Modulus of the tube and plug sheet may be between 0.4 and 0.6 times that of the main body of the box
Meta-models set 3	
$0.4 \leq x8 \leq 0.6$	The equivalent Young's Modulus of the tube sheet may be between 0.4 and 0.6 times that of the main body of the box
$0.75 \leq \frac{x9}{x8} \leq 1$	The equivalent Young's Modulus of the plug sheet may be between 0.75 and 1 times that of the tube sheet

6.3 Loading, boundary conditions and mesh refinement

The loading and boundary conditions for this FE model are identical to that of the model in Chapter 5. The entire FE model was again meshed using second order tetrahedral elements, except for the RBE2 elements that were used to distribute the nozzle loads from a single point to the top surface of the nozzle.

A mesh refinement study was performed on a representative FE model by varying the number of through thickness elements at the SCLs between 3 and 7. The results showed that for the SCLs that lay in the corners of the box next to the welds, satisfactory convergence was reach when using 6 through thickness elements. For the remainder of the SCLs, which all lay further way from any structural discontinuities, a through thickness element count of 3 showed sufficient convergence. For a clearer indication of which SCLs are being described here, please reference Figure 6.6. All the SCLs which lie on SCP 1, 5, 6, 10, 11, 15, 16 and 20 were given 6 through thickness elements and the remaining SCLs were given 3 through thickness elements.

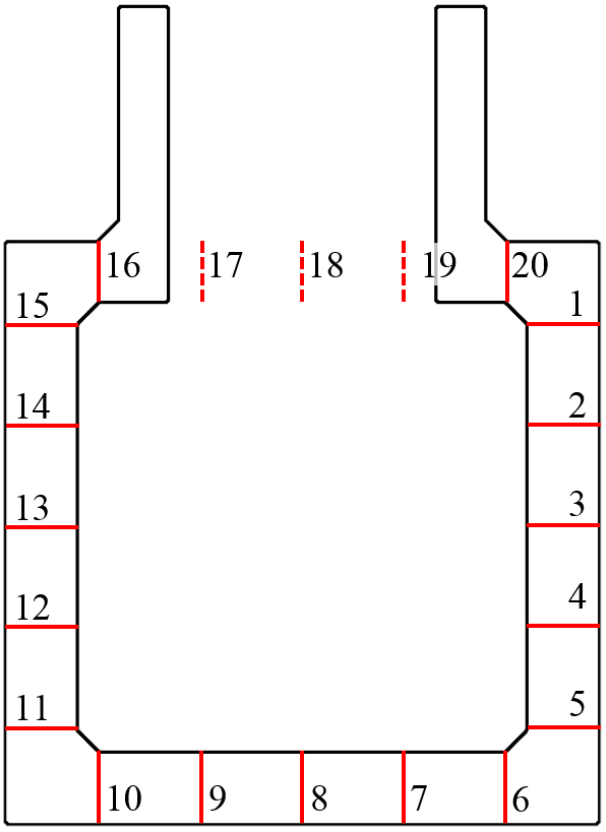

Figure 6.6: SCP reference guide

6.4 Simulation and results

While studying the structural effects that a nozzle has on the body of a header box, the meta-models in this chapter were also used to determine how the performance of these models differ, based on the number of training points that are used to construct them. The approach taken was to fit three separate sub models while constructing each of three overall meta-models, where each sub model uses a different number of training points. A schematic layout of this approach is shown in Figure 6.7.

Using the results from the meta-model in Chapter 5 as a desired baseline for performance, it was decided that the smallest of the three sub models in each case (the sub model using the fewest training points) would use a similar number of training points to the model in Chapter 5. This number was taken to be three times the number of unknowns required to fit a 5^{th} order RS. The training set to be used for the second and third sub model in each case were respectively selected to be two and three times this size, so that the model

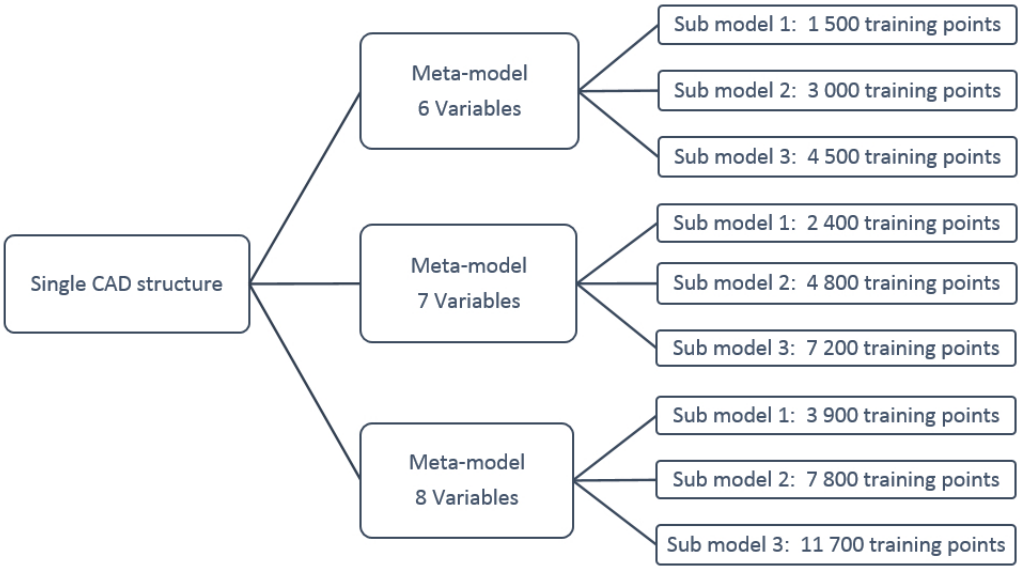

Figure 6.7: Summary of models to be trained

performance could be measured against a significant increase in the number of training points.

In addition to the training sets, an independent testing set was also generated for each of the three overall meta-models. The testing set in each case was 15 % of the size of the training set used for the first sub model, or in other words it would have 45 % of the number of points required to fit a 5^{th} order RS. In practice, these numbers were rounded up to figures that were easier to work with (e.g. 462 rounded to 500), which simplified the process of keeping track of the larger number of simulations that followed.

6.5 First partial header box model

The 1^{st} meta-model had 6 variables. The number of unknowns for a 5^{th} order RS in 6 dimensions is 462. This number was rounded up to 500. This meant that the total number of training points required to fit the largest of the three sub models was 4500. To reach this number, LHC design was used to generate two independent sampling sets of size 1500 and 3000. The sampled results from the first independent set could then be used to train the first sub model, the second independent set to train the second sub model and the combination of the two sets to train the third sub model. A third independent set of 225 points was also generated to be used as the testing set. As in Chapter 5, for each independent sampling set generated, 10 000 LHC DOEs were generated and the instance with the lowest correlation between points was selected (this

technique will be employed for all future LHC sets generated in this study, but will not be explicitly mentioned going forward).

For this new meta-model, the number of mathematical models to be trained for every sub model rose sharply from 1344 to 24 444. This is due to the significant increase in the number of SCLs from 16, for the model in Chapter 5, to 291 for this model. Consequently, the amount of time and resources required to train these models also rose significantly, espesially for the subsequent meta-models with more variables and training points.

The parameters used to fit these mathematical models are shown in Table 6.3. These are the same parameters used for the model in Chapter 5, but without the box length being a variable.

Table 6.3: Design parameters

Parameter	Description
$x1$	Nozzle outer diameter
$x2$	Side plate thickness
$\frac{x3}{x1+4w}$	Box inner height over inner width
$\frac{x4}{x2}$	Plug and tube sheet thickness over side plate thickness
$\frac{x5}{x1}$	Nozzle thickness over nozzle outer diameter
$x6$	Nozzle length

The R-squared results for the largest of the three sub models that were fit are shown in Table 6.4. These values were calculated based on the data of the testing set. A full discussion of how the first two sub models performed and how the number of training points used influences the performance of these models will be undertaken in Chapter 8.

Once again, the 4^{th} and 5^{th} order RS models showed the best results and the final meta-model was constructed from a combination of these. The 5^{th} order RS models were used for the *Pressure*, F_x and F_z load cases and the 4^{th} order RS models were used for the remaining load cases.

Table 6.4: R-squared values based on testing set

Load case	SVD Regression 1	SVD Regression 2	Combined Model
		3^{th} order models	
Pressure	0.9821	0.9821	0.9821
F_x	0.9913	0.9913	0.9913
F_y	0.9977	0.9977	0.9977
F_z	0.9919	0.9919	0.9919
M_x	0.9949	0.9949	0.9949
M_y	0.9965	0.9965	0.9965
M_z	0.9925	0.9925	0.9925
		4^{th} order models	
Pressure	0.9940	0.9941	0.9941
F_x	0.9981	0.9977	0.9981
F_y	0.9990	0.9980	**0.9990**
F_z	0.9977	0.9975	0.9977
M_x	0.9986	0.9967	**0.9986**
M_y	0.9989	0.9972	**0.9989**
M_z	0.9986	0.9951	**0.9986**
		5^{th} order models	
Pressure	0.9884	0.9961	**0.9962**
F_x	0.9969	0.9946	**0.9984**
F_y	0.9973	0.9932	0.9980
F_z	0.9971	0.9967	**0.9979**
M_x	0.9966	0.9894	0.9968
M_y	0.9976	0.9902	0.9977
M_z	0.9964	0.9801	0.9968

A visual representation of the accuracy of the overall meta-model is given in Figures 6.8 and 6.9. These plots show a normalised comparison of the predicted versus actual stress results based on the testing set. Each of these two plots show 130 950 comparison points being displayed as 98 % transparent dots in

order for densely populated areas to be more apparent. The transparency value used here differs from that in Chapter 5 due to the increased amount of data points displayed in a single graph. The comparison plots for the remaining five load cases are given in Appendix B.

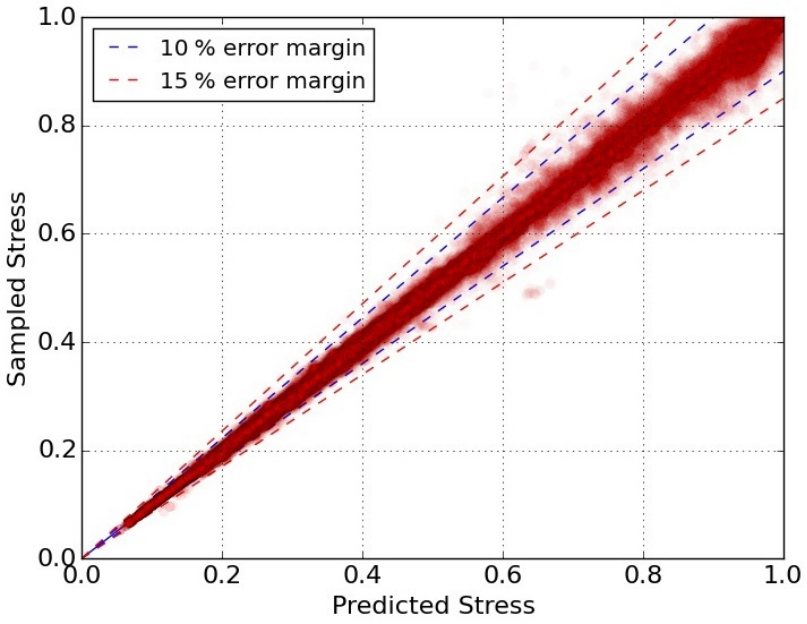

Figure 6.8: Lowest scoring model based on testing set: $R^2 = 0.9962$

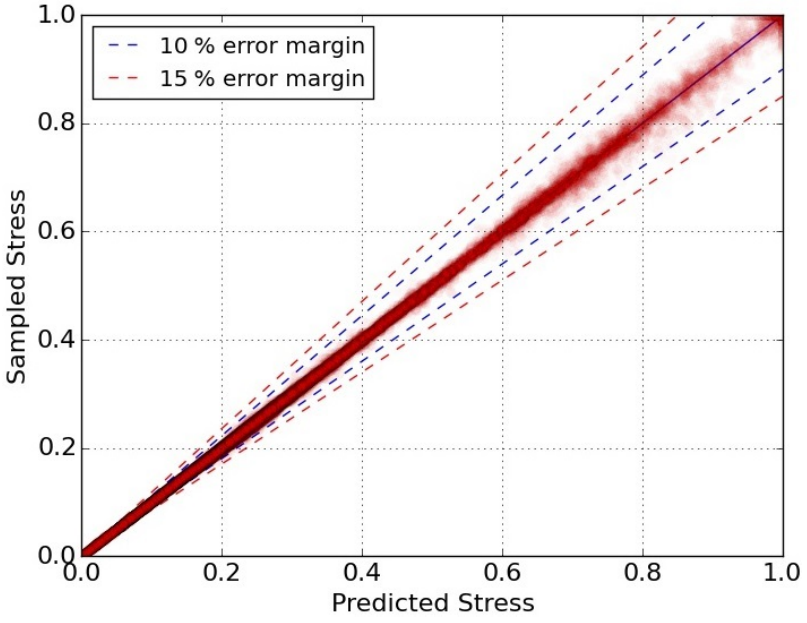

Figure 6.9: Highest scoring model based on testing set: $R^2 = 0.9990$

Another method of visually inspecting the results is to plot the predicted and actual results of a single sample case together on a graph. Figure 6.10 shows an example of such a plot. The results showcased are for the first sample case of the testing set generated earlier. This is effectively a random selection from the testing set as there is no organised pattern according to which the LHC generated the points.

To make the comparison easier to understand, the results were split over four graphs, with each graph showing the results for one of the header box sides. In each graph, there are ten sets of results, five showing membrane stress and five showing membrane plus bending stress (no distinction is made between these in the plot as its purpose is only to compare predicted and actual results). The result sets are represented by lines running from left to right across the graph. Each line corresponds to a stress value (membrane or membrane plus bending) at a position on the box's cross-section, where the SCPs are located, which is then tracked as it moves along the length of the box past the region where the nozzle is located (refer to Section 6.1). In cases where the lines moving from left to right are broken in the middle, these are the results from the SCPs that move through the nozzle. The results in Figure 6.10 are for the load case with pressure only, which had the lowest R-squared values and thus represent the worst case scenario. The blue lines represent the predicted stresses and the red lines show the actual samples stress values.

From all of these results it is clear that the meta-model approximates the stresses on the body of the box very well. The R-squared values for the various load cases range between 0.9962 and 0.9990 and for the lowest performing load case, only 0.2 % of the test points yielded a non-conservative prediction with an error of more than 10 %. Both the tabulated and visual results also show an increase in performance over the models in Chapter 5. The reasons for this change is attributed primarily to the new design space that was adopted and to the fact that there is a larger ratio between the number of training points and unknowns in this model. An analysis of what the results presented here means, along with a discussion about their value to designers follows in Section 6.8.

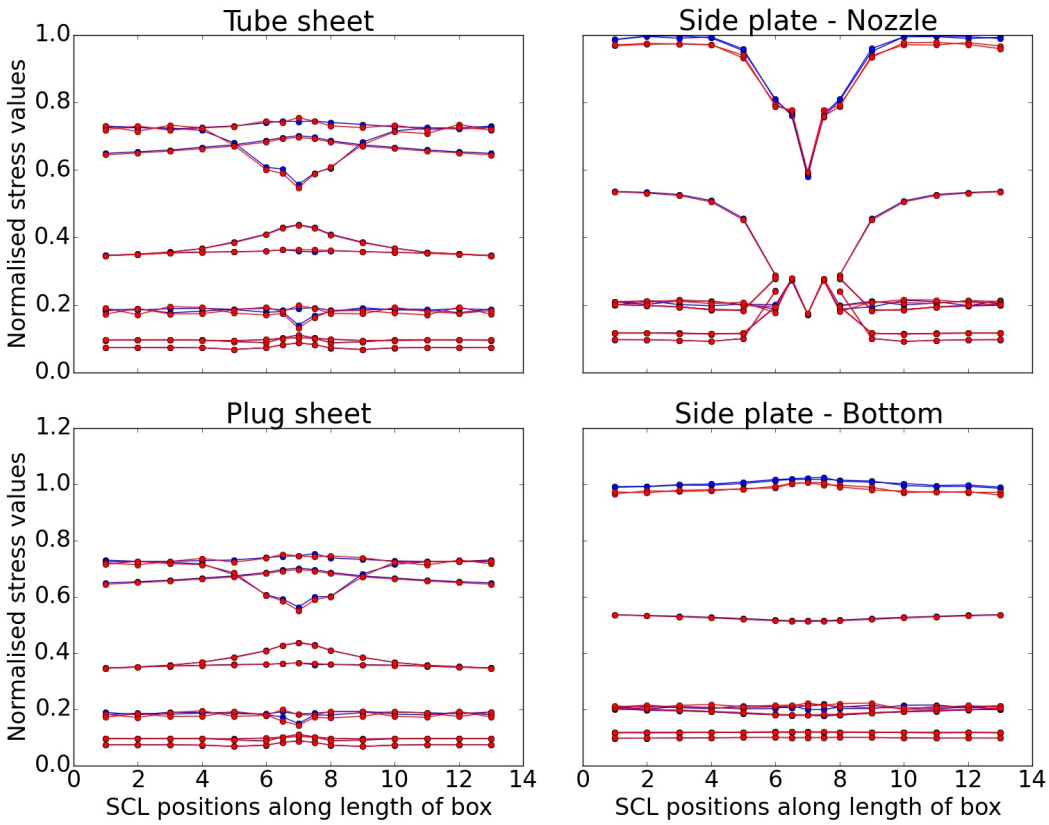

Figure 6.10: Visual comparison of single sample case: blue - predicted, red - actual

6.6 Partial header box with experimental equivalent material

Building on the success of the previous meta-model, it was decided to increase the complexity of the model by adding a new variable. The new variable was used to introduce a simplified equivalent material into the FE model in order to approximate the weakened state of the tube and plug sheets, which contain numerous holes. The new variable, $x7$, took the form of a ratio between the value for Young's Modulus used in the main body of the box and a reduced Young's Modulus that was applied to the tube and plug sheets as given by Equation 6.1. This variable was allowed to range between 0.4 and 0.6, as previously stated in Table 6.2.

$$x7 = \frac{E_{reduced}}{E_{body}} \tag{6.1}$$

With 7 variables the number of unknowns for a 5^{th} order RS fit is 792. This number was rounded up to 800. Consequently, the total number of new

training points to be analysed was 7200. This was once again divided into two smaller sets of 2400 and 4800 respectively. Additionally, an independent testing set of 360 points was also analysed.

While this meta-model had an additional variable compared to the previous model, the number of mathematical models to be trained stayed constant, as this only depends on the number of SCLs being considered. The time and computational resource required to fit the models did however increase, as the number of terms in the models and the number of training points were increased.

The R-squared values for the new models are given in in Table 6.5. Once again, these values are based on the results of the testing set. Here again, the 5^{th} order RS models preformed the best for the *Pressure*, F_x and F_z load cases and the 4^{th} order RS models preformed the best for the remaining load cases.

Table 6.5: R-squared values based on testing set

Load case	SVD Regression 1	SVD Regression 2	Combined Model
		3^{th} order models	
Pressure	0.9759	0.9759	0.9759
F_x	0.9893	0.9893	0.9893
F_y	0.9975	0.9975	0.9975
F_z	0.9887	0.9887	0.9887
M_x	0.9926	0.9926	0.9926
M_y	0.9965	0.9965	0.9965
M_z	0.9904	0.9904	0.9904
		4^{th} order models	
Pressure	0.9930	0.9931	0.9932
F_x	0.9975	0.9969	0.9975
F_y	0.9992	0.9979	**0.9992**
F_z	0.9971	0.9967	0.9971
M_x	0.9983	0.9954	**0.9983**
M_y	0.9988	0.9965	**0.9988**
M_z	0.9982	0.9934	**0.9982**

		5^{th} order models	
Pressure	0.9816	0.9959	**0.9961**
F_x	0.9974	0.9954	**0.9982**
F_y	0.9965	0.9939	0.9969
F_z	0.9972	0.9965	**0.9981**
M_x	0.9968	0.9898	0.9973
M_y	0.9973	0.9905	0.9977
M_z	0.9958	0.9846	0.9968

As done previously, these results were also confirmed visually by comparing the results from the testing set with those predicted by the meta-model. Figures 6.11 and 6.12 show this comparison for the lowest and highest performing load case. The results for the remaining five load cases available in Appendix C. Each of these plots show 209 520 points of comparison.

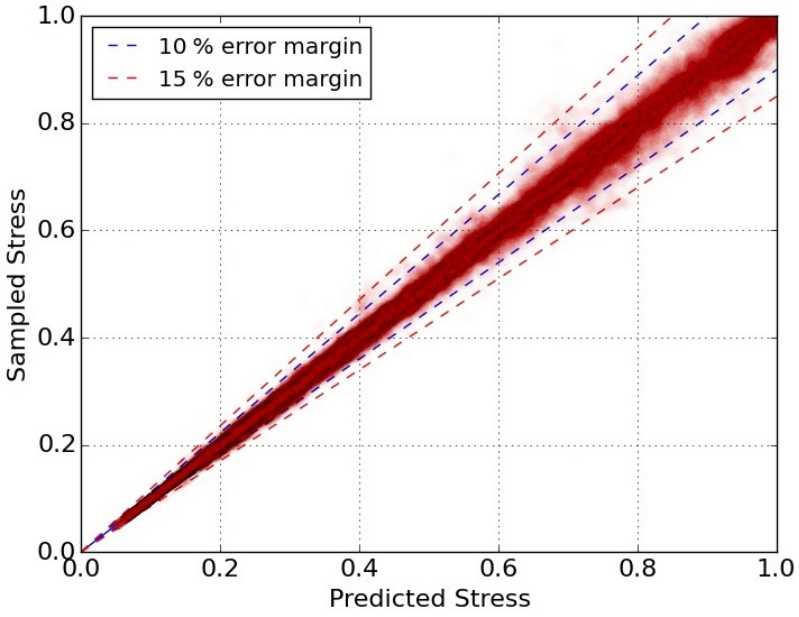

Figure 6.11: Lowest scoring model based on testing set: $R^2 = 0.9961$

Further visual confirmations were also performed by comparing the results of individual test samples with predicted results and were found satisfactory. Overall, these models once again showed a very high degree of accuracy with R-squared values of 0.9961 and above. This in turn served to confirm the feasibility of modelling equivalent material behaviour by varying a material property, which was the first non-geometric variable to be considered.

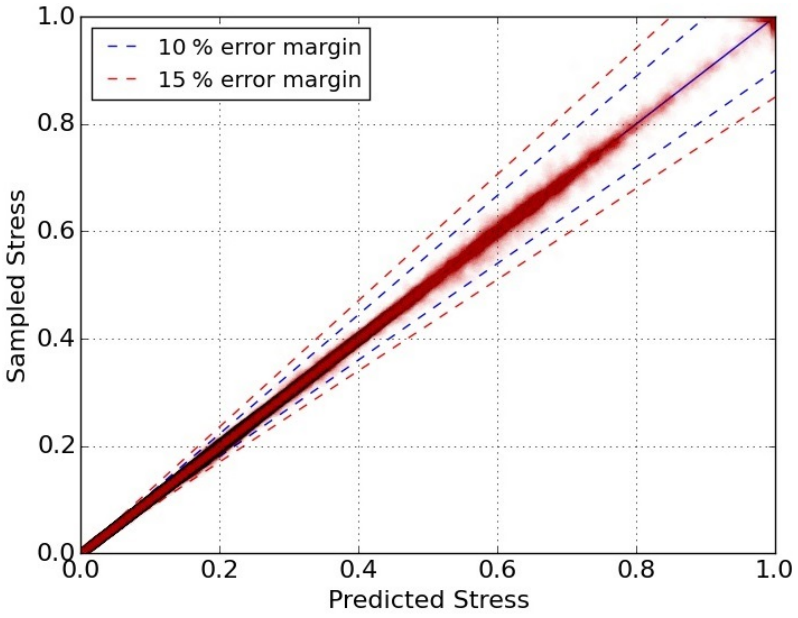

Figure 6.12: Highest scoring model based on testing set: $R^2 = 0.9992$

6.7 Partial header box with basic equivalent material

The purpose of the final model in this chapter was first to expand the capabilities of the overall meta-model, but also to further test the equivalent material modelling capabilities. As such, an additional variable was added which allows for the tube and plug sheets to each have individual equivalent material properties.

In practice it is most often the case that the plug sheet of a header box has a lower ligament efficiency than the tube sheet. This is because the holes in a plug sheet are usually larger than the holes in the tube sheet due to construction and maintenance requirements. With the new variable integrated, the Young's Modulus of the tube sheet was again allowed to vary between the same bounds as in the previous meta-model. The Young's Modulus of the plug sheet was then proportionally coupled to the value of the tube sheet and could vary to between 75 and a 100 % of the tube sheet's Young's Modulus, thus allowing it to be somewhat weaker also (refer to Table 6.2 for more detail).

With eight variables considered in this meta-model, the total number number of training points to be sampled was taken as 11 700, based on the 1 287 unknowns in the corresponding 5^{th} order RS. The training points were again comprised of two smaller independent sample sets of size 3 900 and 7 800 respectively and the testing set contained 585 sample points. The R-squared results for the models that were fit are given in Table 6.6.

Table 6.6: R-squared values based on testing set

Load case	SVD Regression 1	SVD Regression 2	Combined Model
		3^{th} order models	
Pressure	0.9764	0.9764	0.9764
F_x	0.9900	0.9900	0.9900
F_y	0.9977	0.9977	0.9977
F_z	0.9893	0.9893	0.9893
M_x	0.9925	0.9925	0.9925
M_y	0.9961	0.9961	0.9961
M_z	0.9903	0.9902	0.9903
		4^{th} order models	
Pressure	0.9929	0.9931	0.9930
F_x	0.9976	0.9970	**0.9976**
F_y	0.9992	0.9978	**0.9992**
F_z	0.9969	0.9967	**0.9970**
M_x	0.9984	0.9959	**0.9984**
M_y	0.9989	0.9965	**0.9989**
M_z	0.9984	0.9946	**0.9984**
		5^{th} order models	
Pressure	0.9883	0.9951	**0.9952**
F_x	0.9829	0.9947	0.9954
F_y	0.9640	0.9932	0.9939
F_z	0.9898	0.9957	0.9962
M_x	0.9718	0.9891	0.9916
M_y	0.9766	0.9905	0.9919
M_z	0.9599	0.9844	0.9882

From the results we can see that the 5^{th} order RS fit approximates the *Pressure* load case the best, while the the remaining load cases are best approximated by 4^{th} order RS fits.

In some cases it is noted that the performance of the combined model is marginally lower than of the initial SVD model cases. This can be attributed to two reasons. The first is that the performance values being compared are equivalent von Mises stresses. As mentioned, these values are calculated using the predictions of six individual RS models and the decision of which models to include in the final combined model happens at this level. It is however not necessarily the case that a comparison of equivalent von Mises performance values will produce better results simply because the models that were used to predict their input values showed better individual performances. The second reason is that there are only a finite number of sample points in the testing set used to calculate the predicted performance values for the models. These results are thus not exact and may vary to a certain degree.

The visual comparisons in Figure 6.13 and 6.14 again show the lowest and highest scoring load case results, with the remaining results available in Appendix D. Each of these plots display 340 470 points of comparison.

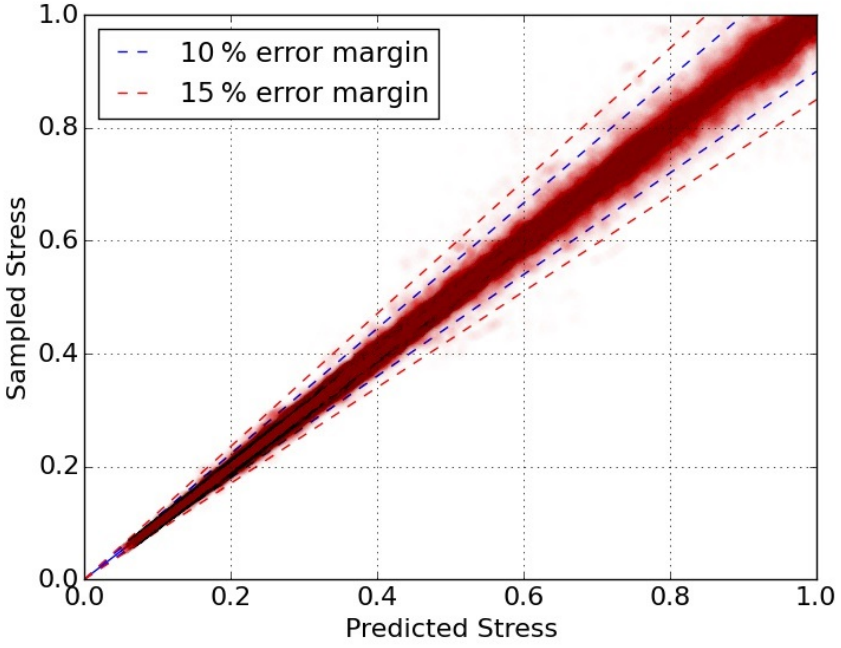

Figure 6.13: Lowest scoring model based on testing set: $R^2 = 0.9952$

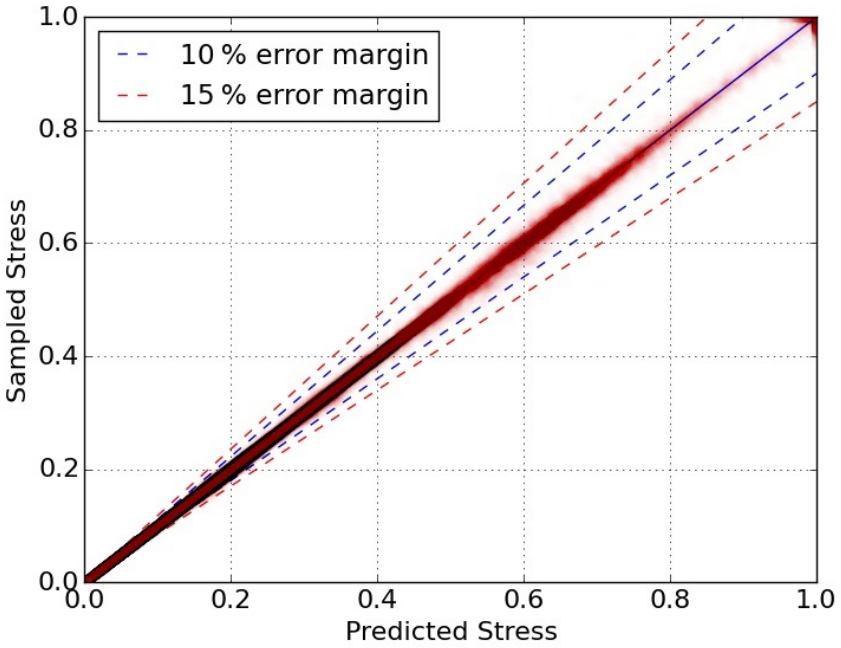

Figure 6.14: Highest scoring model based on testing set: $R^2 = 0.9992$

These results confirm that this final meta-model again approximates the data accurately with 98.9 % of the results for the *Pressure* load case having an error of less than 10 %. This allows the meta-model to be used with a reasonably high level of confidence.

6.8 Results discussion

With the accuracy of the meta-models established, a discussion of the value of these models will now follow. For the purpose of this discussion, only the results of the final meta-model that was trained, with 8 variables, will be used. This model supersedes the complexity of the other two models and due to the similar nature of the three overall models no additional insight will be gained from considering the results of each meta-model separately.

Using the processing tools of the GUI from Section 5.4, a results plot similar to that in Figure 6.10 can be produced. Figure 6.15 shows such a plot, for a header box under pressure loading only. The purpose of this normalised plot is to give a designer an overview of the behaviour of stress values predicted for the body of the box. The results for each side of the header box are presented on a separate graph where the red lines represent membrane stresses and the blue lines membrane plus bending stresses. Each of the lines corresponds to one of the 20 SCPs shown in Figure 6.3 and tracks the stress values on these

planes along the length of the box, past the position of the nozzle. By following the lines from left to right, the user can asses to what degree the stresses on each side of the header box are affected by the nozzle.

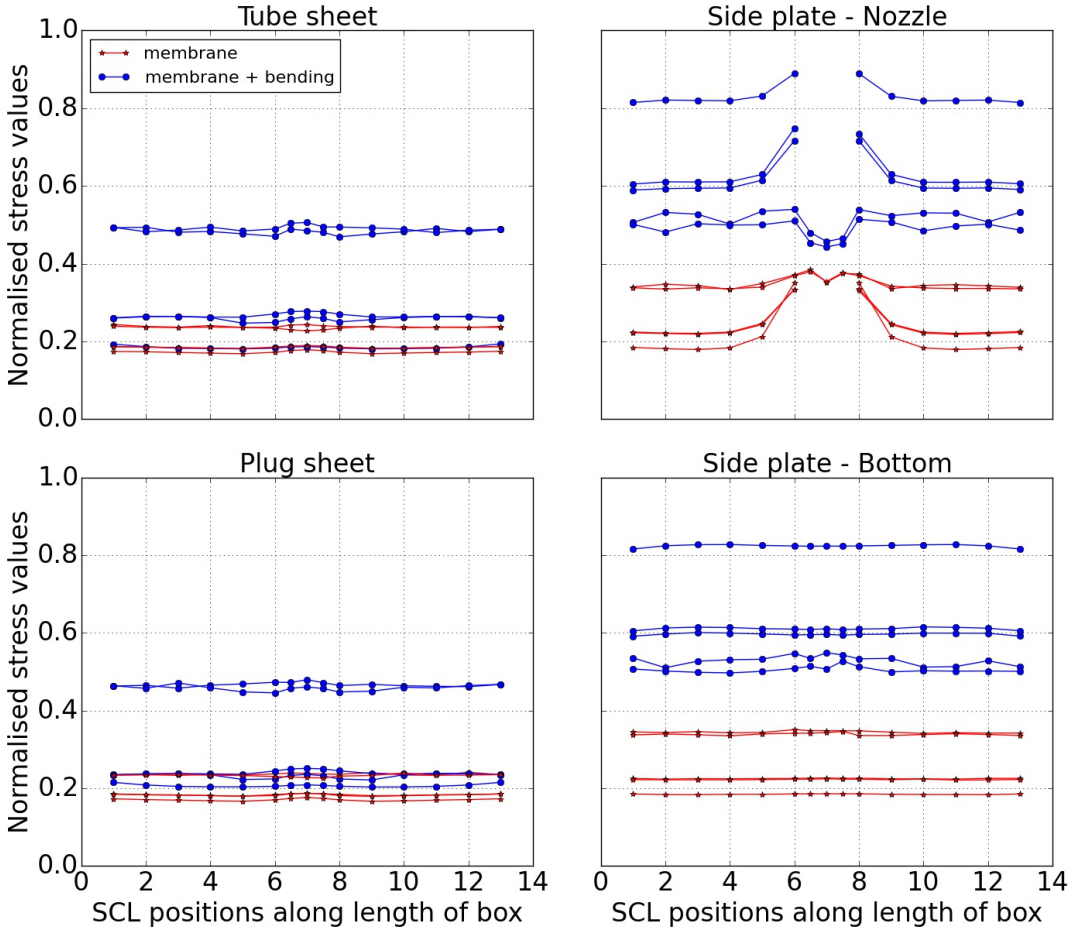

Figure 6.15: Example results predicted by meta-model

Based on the results shown we can see that for this example, only the side plate of the header box to which the nozzle is connected experiences any significant increase in stress as a result of the nozzle. This result stands to supports the best practice design methods currently employed, which assume that only the side of a header box with a nozzle is affected by its presence.

The benefit of having the meta-model results is that the designer is now able to asses to what extent the side plate is actually weakened, rather than having to use the generically applied 0.5 ligament efficiency value for the side plates (the origin of the 0.5 ligament efficiency factor was discussed in the introduction of this chapter). The user can also go a step further than the standard

design method and calculate separate ligament efficiency factors which apply individually to the membrane or membrane plus bending results of each SCP. These values are calculated as the inverse of the percentage rise seen along each of the membrane or membrane plus bending lines, up to a maximum value of one. For the cases shown, the new effective limiting membrane stress ligament efficiency factor for the side plate with the nozzle would become 0.86 and the limiting membrane plus bending stress ligament efficiency factor would become 0.91. Even though the calculated efficiency values for some of the SCPs may be lower than this, these are effectively the efficiency factors that matter, as they are the values calculated along the SCPs where the critical membrane and membrane plus bending stresses are found. Having a higher ligament efficiency factor means that a higher effective allowable stress will be permitted for the side plate.

Another set of results for a different design case are shown in Figure 6.16. These results, which are also for a header box under pressure loading, show a completely different set of trends. Looking at the side plate with the nozzle, we see that while the membrane stresses still increase in the region of the nozzle, the membrane plus bending stresses decrease significantly in this region. Also, when looking at the tube and plug sheets, we see that the stresses here have been significantly affected around the region of the nozzle. While the membrane stresses remain more or less unchanged, we see that the critical membrane plus bending stress in each case increases in the region of the nozzle. This is behaviour which is not accounted for at all by the traditional design calculations. Thus, apart from potential cost savings implications of this new tool, it also serves as an additional safety check for designers that will highlight cases where traditional design methods may be non-conservative.

In the same way that the results for the *Pressure* load case have been viewed, any of the other load cases can also be visualised. Figure 6.17 shows the results for the same example as the previous plot, but with the load case F_x applied. While the stress patterns in this plot differ significantly from those in the previous example, this is to be expected as the loading in this case is focussed on the nozzle. The general trend of seeing high stresses at the centre of each graph that decrease as they move towards the end was thus anticipated. Plots showing the predicted stress profiles for the remaining five load cases can be seen in Appendix G.

Depending on the design loads of a specific case, the nozzle loads can be added to the pressure load results in any ratio and viewed together to assess the overall combined effect. An example of this is shown in Figure 6.18 where the *Pressure* and F_x load cases have been added together.

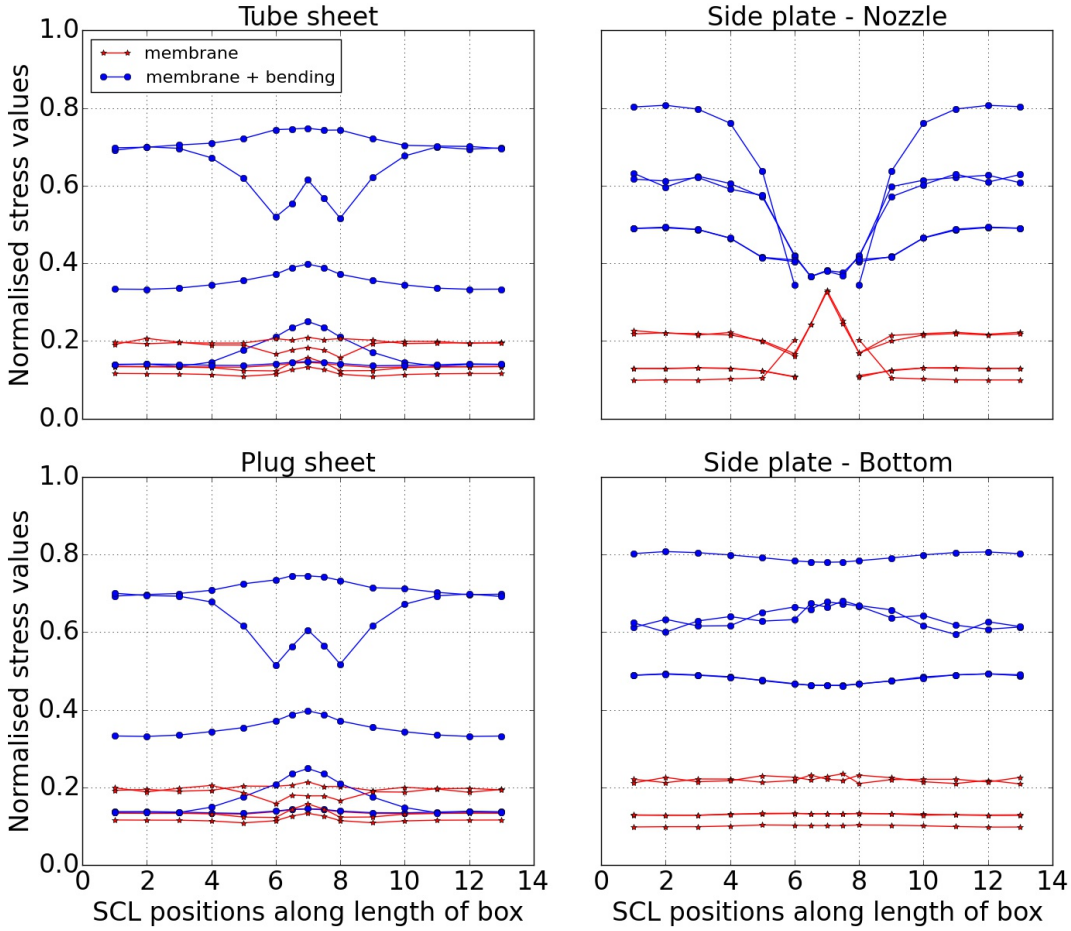

Figure 6.16: Example results predicted by meta-model for load case *Pressure*

As required, the designer can also view the results for any of the four sides of the header box in more detail, as shown in Figure 6.19, where the numbers in the legend correspond the SCP numbering in Figure 6.6.

By completing this meta-model two goals have been achieved. The first was to successfully scale up the size and complexity of the meta-models being constructed as well as the process used to produce the meta-models. A sense of this scale can be gained when considering the following: the number of SCLs where stresses were extracted and can thus be predicted at was increased from 16 in Chapter 5 to 291 for the meta-models in this chapter. The total number of simulations performed was increased from 2 875 to 24 570. Finally, the total number of RS trained, while searching for the best models, was increased form 8 064 in Chapter 5 to 1 319 976 in this chapter.

The second goal that was achieved was to create an interactive tool which gives designers real time results and allow them to assess the effects a nozzle has on the body of a header box under various loading conditions in a manner not previously available. Using these results, designers will be able to assess a structure and calculate true required ligament efficiency factors, rather than using a blanket value. This will lead to safer designs and unlock possible cost savings potential.

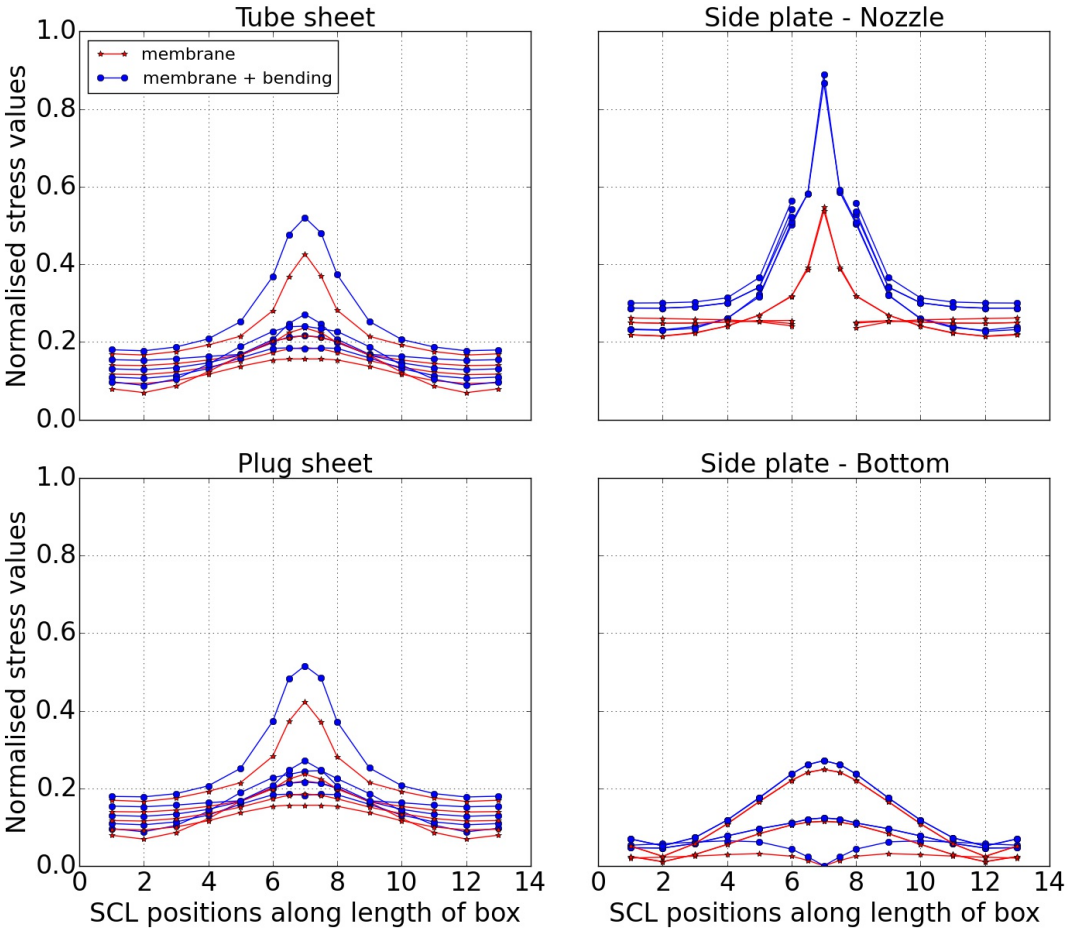

Figure 6.17: Example results predicted by meta-model for load case F_x

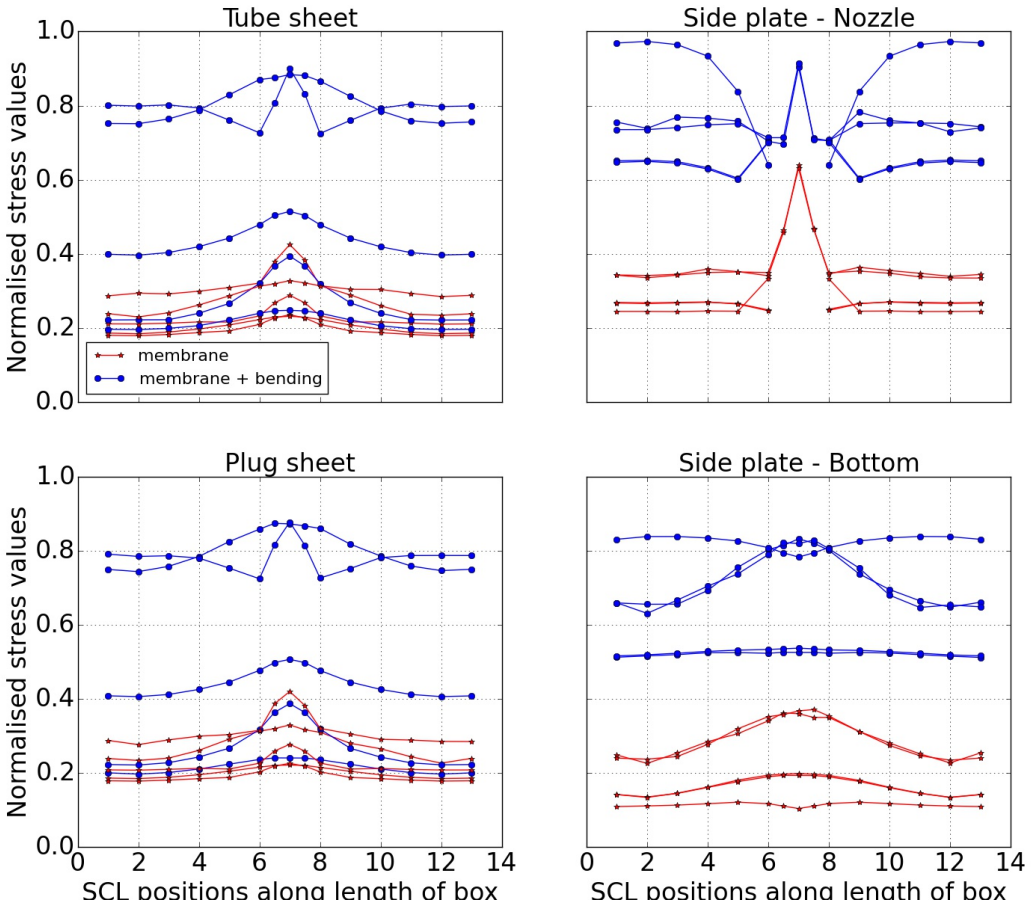

Figure 6.18: Example results predicted by meta-model for combined loading

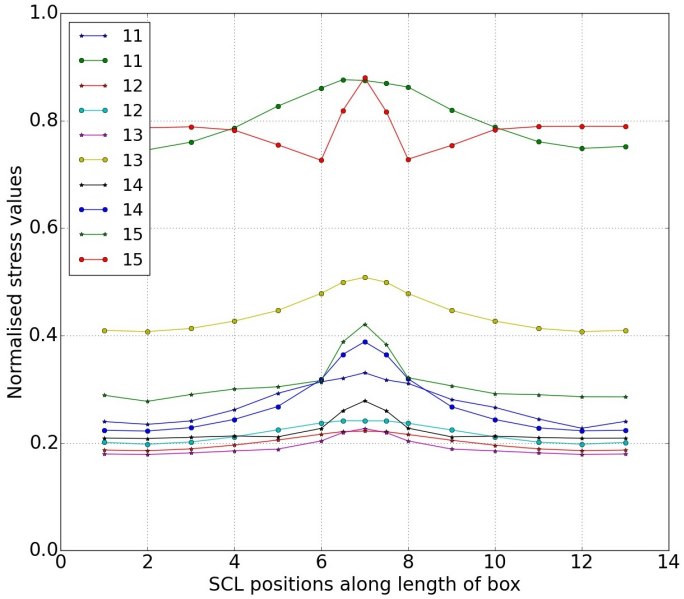

Figure 6.19: Detailed results prediction: stars - membrane, dots - membrane plus bending

Chapter 7

Complete header box model

The final step in the evolution of this study was to upgrade the meta-models from the previous chapters to a complete plug type header box model. In this chapter two such models were constructed. The first model, with ten variables, was used as a test case for the new geometry and also to further study the performance of these models in relation to the number of training points used to construct them. The second model, having twelve variables, was constructed as the final and most complete plug type header box model that could be assembled within the scope of this study, given the available computational resources.

7.1 Model setup

The primary difference of the FE models in this chapter to those that came before is that the new FE models include the end plates of the header box structure, as seen in Figure 7.1. Once again, the CAD structure has been divided to correspond with the positions of the SCLs to allows for more detailed mesh control in these areas. Attached to the end plates are the tabs used to fasten a header box to the frame of an air cooled heat exchanger. While other methods for fastening header boxes do exist, for the purpose of this study tabs were used as that is the design used by the industry partner supporting this research. The tabs were given a fixed size, extending 85 mm past the edge of the end plates.

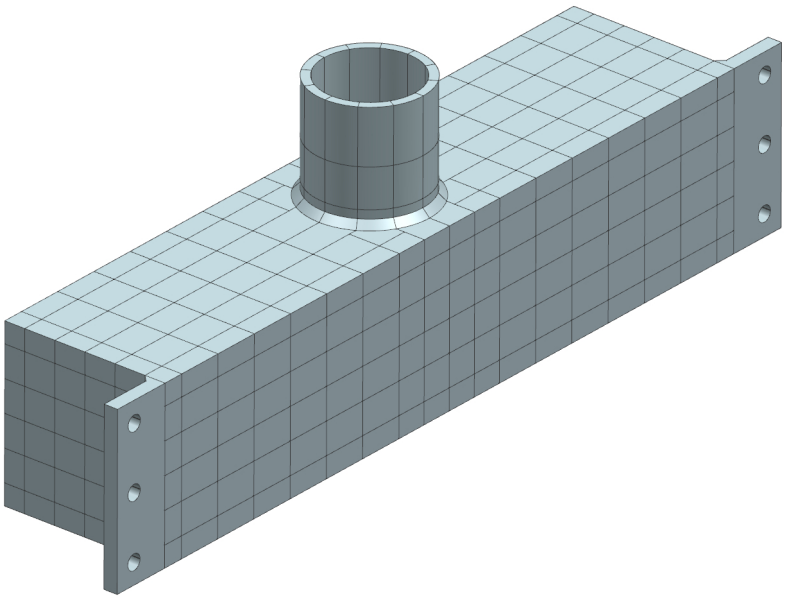

Figure 7.1: CAD layout for new FE model

A meshed example of the structure showing the positions of the SCLs, indicated by the yellow pointers, is shown in Figure 7.2. This new structure has 429 SCLs arranged to cover the entire body of the structure. This is almost 50 % more than in the previous FE models. The SCLs on the four large sides of the box were arranged in a similar manner, along twenty SCPs as in Chapter 6, only this time the SCPs stretch the entire length of the box. These SCPs retained the same numbering system from one to twenty, as was given in Figure 6.6.

The SCLs on each end plate were also arranged along a set of five SCPs. The layout and numbering of these SCPs are shown in Figure 7.3. Finally, the SCLs in and around the nozzle were arranged along what will be referred to as circular SCPs. The positions and numbering used for these circular SCPs are shown in Figure 7.4. Along each of these SCPs there are 12 SCLs, spaced equally around the perimeter of the nozzle.

7.2 Loading, boundary conditions and mesh refinement

While the design of the tabs on the header box include three bolt holes, only the upper and lower hole in each tab is used when fastening. The third hole is used only during construction. After being fastened in place, the bolts holding the header are loosened slightly, to allow the header to float to a certain degree while being held in position. This prevents the header box

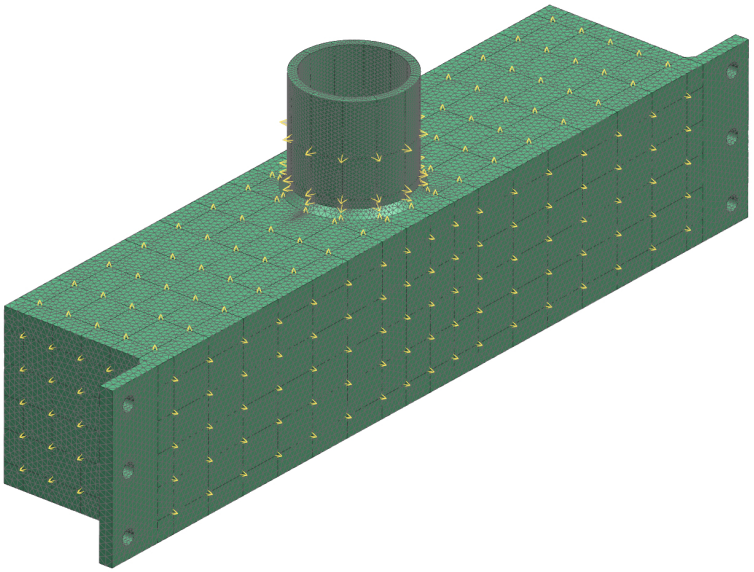

Figure 7.2: Mesh and SCL placement

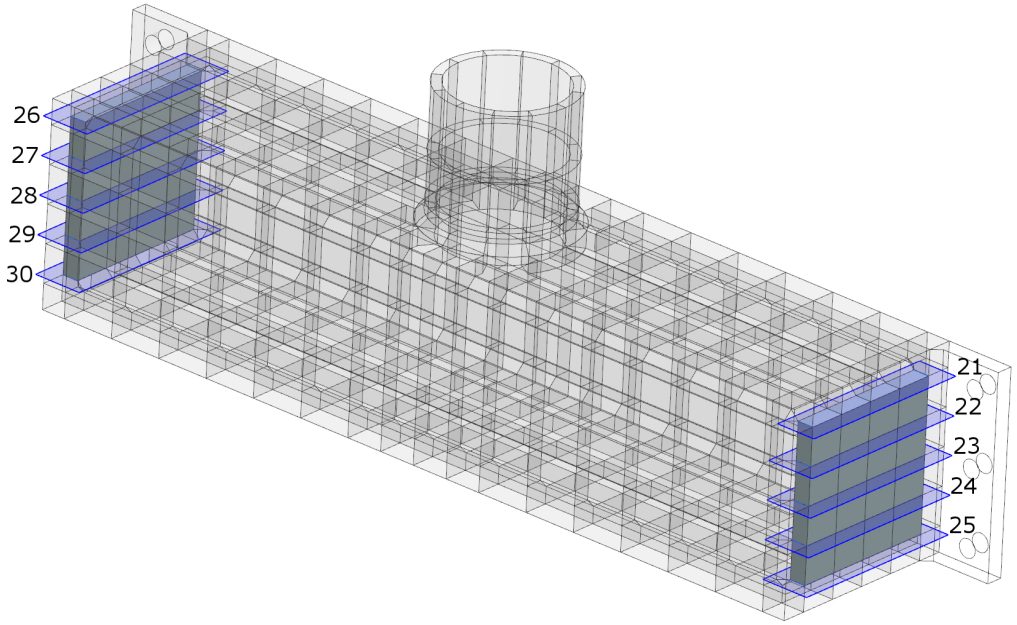

Figure 7.3: SCP placement on end plates

from deforming the frame it is connected to when it expands or contracts, as the header structure is usually far more stiff than the frame. In an attempt to mimic these conditions, the following boundary constraints were applied. The outward facing side of the two tabs, indicated in red in Figure 7.5, were constrained in the X-direction and the upper most bolt hole on either side of the header box was give a cylindrical constraint, which prevented the nodes inside the hole from moving radially outwards from the hole axis, but freed

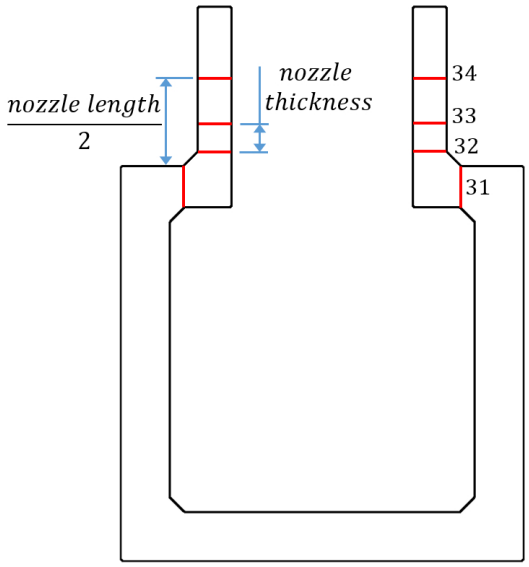

Figure 7.4: SCP placement around nozzle intersection

them to move tangentially around the axis. This allowed the structure to rotate freely around the central axis of each bolt. Finally, the center axis of one of the two cylindrical constraints was freed and allowed to move in the Z-direction to permit the unconstrained expansion of the header along its length.

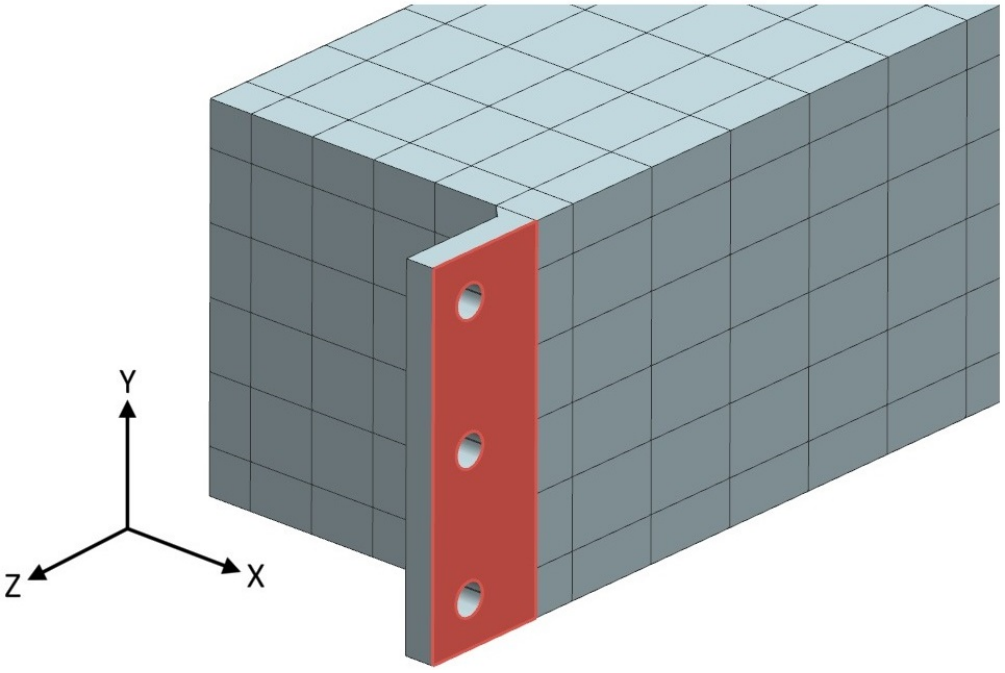

Figure 7.5: Boundary condition guide for complete header box

A mesh refinement study of the new geometry layout was performed on a representative FE model to determine the number of through thickness elements required at the SCL positions. Figures 7.6 and 7.7 show the convergence plots for membrane and membrane plus bending stress respectively at all 429 SCL positions on the header. A careful analysis of these plots show that the SCLs positioned away from structural discontinuities converged very soon as the number of through thickness elements were increased. For the points where SCLs were positioned at a structural discontinuity, such as at the toe of a weld, the results showed convergence in a general sense when five or more through thickness elements were used. The convergence values did however not show significant improvement after this point. Thus, considering the computational cost of performing the large number of FE simulations required in this study, it was decided to limit the number of though thickness elements to seven.

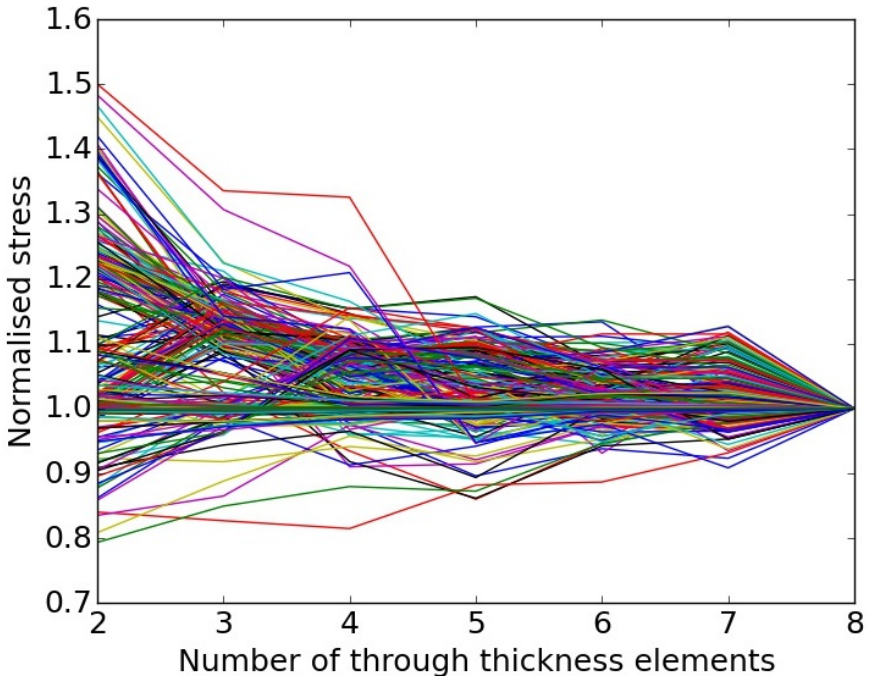

Figure 7.6: Mesh convergence for membrane stress at all SCLs on header

Overall, the results show convergence within 15 % or less was reached when using seven through thickness elements for the SCLs that lay in the corners of the box next to the welds and at the nozzle intersection. For the first ring of SCLs above the nozzle intersection four through thickness elements were required and for all the remaining SCLs, convergence was reached using three through thickness elements. To make this description more clear, all the SCLs which lie on SCP 1, 5, 6, 10, 11, 15, 16, 20, 21, 25, 26, 30, 31, and 32 were given seven through thickness elements. The SCLs on SCP 33 were given four though thickness elements. The SCLs lying on either end of SCP 22, 23, 24, 27, 28, and 29 (these are the SCLs that lie at the welds) were given seven through thickness elements. All the remaining SCLs were given three through thickness SCLs.

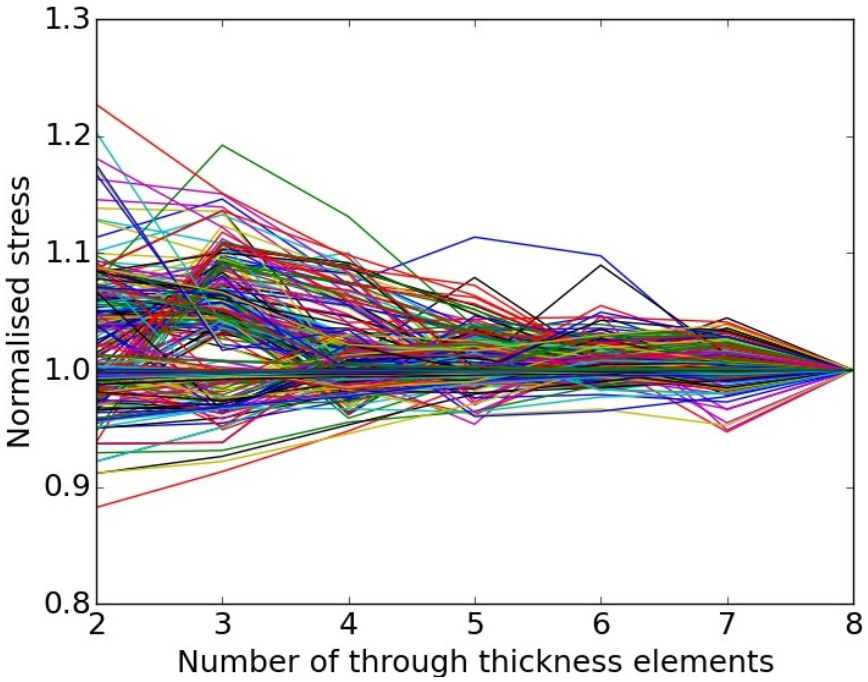

Figure 7.7: Mesh convergence for membrane plus bending stress at all SCLs on header

7.3 Design space

The design space for the meta-models in this chapter builds directly on the design space used for the final meta-model in Chapter 6, which had eight variables. For ease of reference, the overlapping portion will be repeated here in Table 7.1 as part of the description of the design space for the two meta-models in this chapter. The last two variables described were only used in the final meta-model.

Table 7.1: Design space description

Inequality/Equation	Practical description
$100 \text{ mm} \leq x1 \leq 270 \text{ mm}$	The nozzle outer diameter may vary between 100 mm and 270 mm
$20 \text{ mm} \leq x2 \leq 70 \text{ mm}$	The thickness of the two plates orientated perpendicular to the nozzle (called the side plates) may vary between 20 mm and 70 mm
$\frac{1}{1.2} \leq \frac{x3}{x1 + 4w} \leq 1.2$	The inside height of the box may not be less than 1.2 times smaller than the box's inside width and may not be larger than 1.2 times the box's width

$1 \leq \frac{x4}{x2} \leq 2$	The thickness of the two plates parallel to the nozzle (plug and tube sheet) may not be smaller than the side plates' thickness and may not be larger than two times the side plates' thickness
$20 \text{ mm} \leq x4 \leq 80 \text{ mm}$	The thickness of the two plates parallel to the nozzle may vary between 20 mm and 80 mm
$\frac{1}{16a} \leq \frac{x5}{x1} \leq \frac{1}{4a}$ $a = \frac{150 + x1}{210}$	The nozzle thickness may not be more than $16a$ times smaller than the outer diameter of the nozzle and may not be larger than $4a$ times smaller than the nozzle's outer diameter. a is a scaling factor that varies between 1.2 and 2. It has a value of 1.2 when the nozzle outer diameter is equal to 100 mm and increases linearly to 2 when the nozzle outer diameter is equal to 270 mm. This scaling is applied to keep the design space within the bounds of commonly manufactured nozzle sizes
$x5 \geq x2$	The thickness of the nozzle may not exceed the thickness of the side plate
$100 \text{ mm} \leq x6 \leq 350 \text{ mm}$	The nozzle length may vary between 100 mm and 350 mm
$0.4 \leq x7 \leq 0.6$	The equivalent Young's Modulus of the tube sheet may be between 0.4 and 0.6 times that of the main body of the box
$0.75 \leq \frac{x8}{x7} \leq 1$	The equivalent Young's Modulus of the plug sheet may be between 0.75 and 1 times that of the tube sheet

$3(x1) \leq x9 \leq 1000$ mm	The length of the box may vary between 3 times nozzle outer diameter and 1000 mm
$0.5 \leq \frac{x10}{x2} \leq 1$	The thickness of the end plates may vary between 0.5 and 1 times the thickness of the side plates
$0.2 \leq x11 \leq 0.4$	The Poisson's ratio of the tube sheet may vary from 0.2 to 0.4
$0.2 \leq x12 \leq 0.4$	The Poisson's ratio of the plug sheet may vary from 0.2 to 0.4

7.4 Complete header box with basic equivalent material model

The first FE model tested in this chapter was again used to study the performance of the RS models being fit in relation to the number of training points being used. In the previous chapter, this was done by fitting three sub models, each using a different number of training points. The number of training points used for each sub model was calculated based on the number of unknowns in a corresponding 5^{th} order RS fit. The same method was applied here where the number of unknowns for a 10-dimensional 5^{th} order RS fit is 3003. This time however, four sub models were tested instead of three. The additional sub model was included in order to test a case where the ratio between the number of training points and unknowns are reduced further than for the smallest sub models of Chapter 6. It was decided to include this model after the performance comparison results of the previous chapter showed a lower than expected increase in performance in relation to the number of training points being used (this will be discussed further in Chapter 8). A summary of the sub models that were tested is given in Table 7.2.

Table 7.2: Summary of sub models tested

	Training points ratio*	# of training points
Sub model 1	1.5	4550
Sub model 2	3	9100
Sub model 3	6	18200
Sub model 4	9	27300

*ratio of training points to number of unkowns in 5^{th} order RS fit

The required training points were generated using a combination of three independent LHC sets. The first set had 4550 sample points and was used only to train the first model. The second and third sets had 9100 and 18200 sample points and were used to train the second and third sub models respectively. The fourth sub model was trained using the combined sample points of the second and third sets. A fourth independent set of 1365 sample points was generated to be used as a testing set for all the models.

The R-squared values for the model that used the largest number of training points are shown in Table 7.3. These values are based on the results of the testing set. The results for the smaller sub models are not included here, but will be discussed in Chapter 8.

Table 7.3: R-squared values based on testing set

Load case	SVD Regression 1	SVD Regression 2	Combined Model
		3^{th} order models	
Pressure	0.9827	0.9827	0.9827
F_x	0.9869	0.9869	0.9869
F_y	0.9976	0.9976	0.9976
F_z	0.9904	0.9904	0.9904
M_x	0.9929	0.9928	0.9929
M_y	0.9845	0.9845	0.9845
M_z	0.9912	0.9911	0.9912

		4^{th} order models	
Pressure	0.9951	0.9951	0.9952
F_x	0.9970	0.9969	0.9970
F_y	0.9993	0.9988	**0.9993**
F_z	0.9979	0.9979	0.9979
M_x	0.9986	0.9977	**0.9986**
M_y	0.9980	0.9969	0.9980
M_z	0.9983	0.9972	**0.9983**
		5^{th} order models	
Pressure	0.9975	0.9976	**0.9979**
F_x	0.9973	0.9982	**0.9986**
F_y	0.9959	0.9977	0.9984
F_z	0.9976	0.9987	**0.9990**
M_x	0.9947	0.9959	0.9980
M_y	0.9982	0.9949	**0.9989**
M_z	0.9943	0.9952	0.9977

From these results we see that the 4^{th} order RS fits show the best performance for the load cases F_y, M_x and M_z, while the 5^{th} order RS fits perform the best for the remaining load cases.

The quality of these performance values were confirmed visually by comparing the results acquired from the testing set with those predicted by the meta-model. Figures 7.8 and 7.9 show this comparison for the lowest and highest performing load case. The comparisons for the remaining five load cases are available in Appendix E. Each of these plots show 1 171 170 points of comparison.

From the combination of the R-squared values and these visual comparisons, it was concluded that the meta-model constructed was able to approximate the structural behaviour of the complete header box body, which included the new geometric components, accurately and that work could proceed with the final model. This assessment is supported by the fact that the R-squared values for all load cases ranged between 0.9979 and 0.9993 and the lowest performing load case only yielded predictions with an error of more than 10 % in 0.4 % of the test cases.

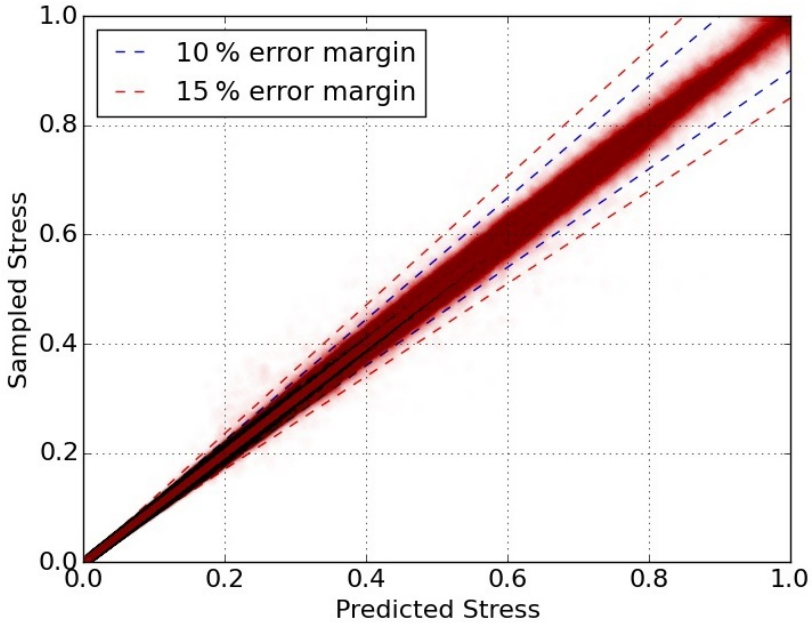

Figure 7.8: Lowest scoring model based on testing set: $R^2 = 0.9979$

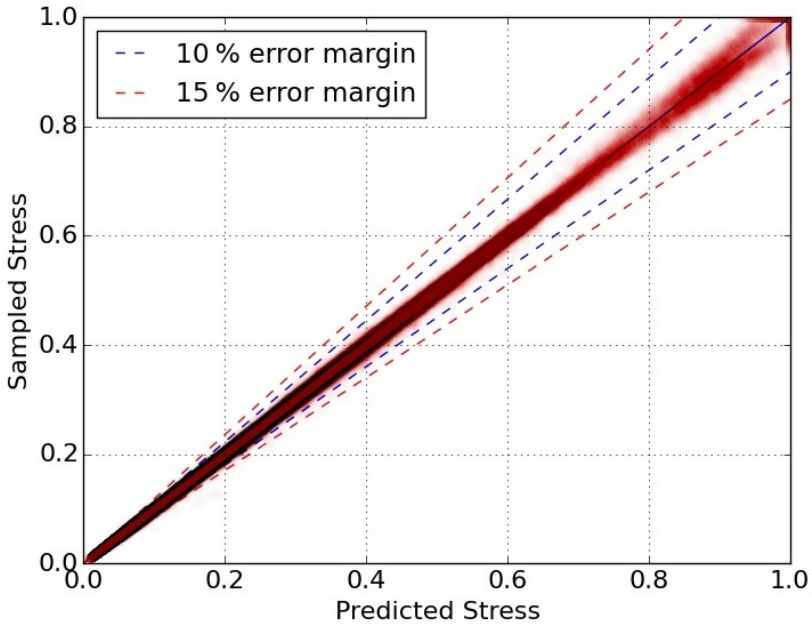

Figure 7.9: Highest scoring model based on testing set: $R^2 = 0.9993$

7.5 Complete header box model

For the final meta-model of this study, two more variables were added. These variables allow for more detailed equivalent material models to be applied to the tube and plug sheets of the final header box by individually varying the Poisson's ratio for each side. These Poisson's ratios, which usually have a value

of 0.3 for ordinary (non-equivalent) materials, according to the guidelines of ASME Division 2 Part 5 (ASME, 2015), were allowed to vary between 0.2 and 0.4, as mentioned in Table 7.1.

The reason that the addition of these two variables were chosen to be the last increment in upgrading the header box model was that they were expected to have only a moderate effect on the behaviour of the model. The reasoning was that if the first model of this chapter could approximate the header box structure well, then a model were only these two variables were added could also be approximated well by applying similar methods. Variables with a higher expected likelihood of adversely affecting the performance of the model were preferred to be added at increments while the overall model still had fewer design variables. This would allow for any troubleshooting operations to be less computationally expensive as there would be fewer simulations to repeat, if required, and less complex RS models to train. An instance where this method proved valuable was mentioned in Chapter 6, where the design space used for the aspect ratio of the header box had to be modified. The testing of the new design space limits applied could be performed relatively inexpensively using the first FE model from that chapter, which only had six variables. For the two subsequent FE models which had seven and eight variables respectively, where only equivalent material characteristics were added, the meta-models performed flawlessly. If only the final FE model of that chapter had been used with all the new variables added at once, the computational expense of these iterations would have been roughly two and a half times more.

Due to the large number of variables included in the final meta-model and the computational expense associated with this, it was decided that only a single set of RS models would be fit to this model. To decide on the number of training points to be used, the performance results of the four sub models described earlier in this chapter were considered. Figure 7.10 shows a plot where the performance values of these models are tracked against the number of training points used to construct them.

These results showed a distinct increase in performance for most load cases when the ratio of training points to unknowns is increased from one and a half to three. After this point however, the overall increase in the performance slows considerably, even for large increases of the number of training points used (it is noted that the graph does not always show a performance increase for each increase in the number of training points. The reasons for this will be discussed in the following chapter). Based on the available computational resources at hand, it was thus decided that the best value would be gained by training the final model with three times more sample points than the number of unknowns in the corresponding 5^{th} order RS model.

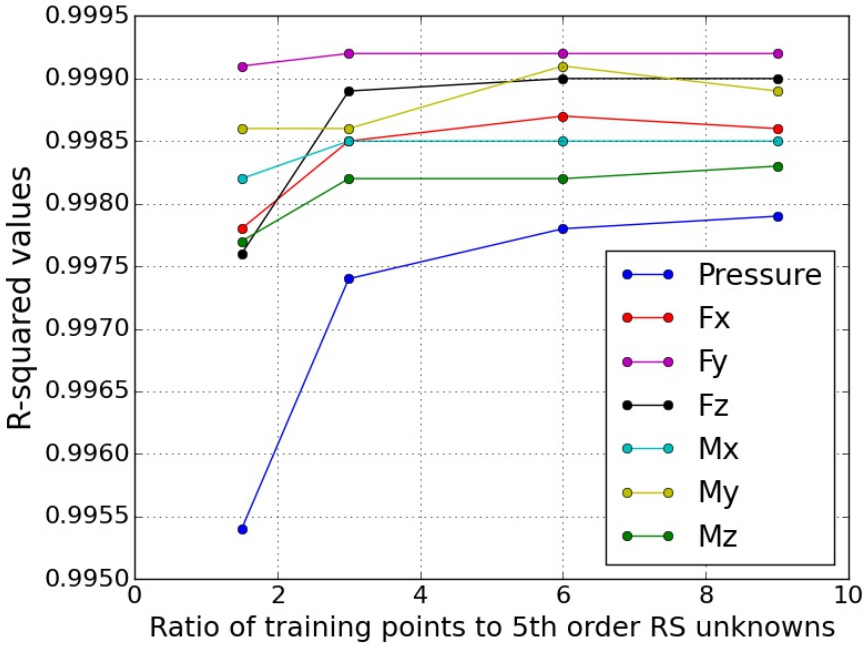

Figure 7.10: R-squared values vs relative size of training set

With the number of unknowns in a 12-dimensional 5^{th} order RS standing at 6 188, the training set was selected to have 18 600 sample points. Additionally, another 2 790 points were sampled to be used for testing purposes. The performance results for the models that were trained are shown in Table 7.4. Once again, these values are based on the results of the testing set.

Table 7.4: R-squared values based on testing set

Load case	SVD Regression 1	SVD Regression 2	Combined Model
		3^{th} order models	
Pressure	0.9834	0.9835	0.9835
F_x	0.9881	0.9881	0.9881
F_y	0.9976	0.9976	0.9976
F_z	0.9912	0.9912	0.9912
M_x	0.9925	0.9925	0.9925
M_y	0.9834	0.9834	0.9834
M_z	0.9905	0.9905	0.9905

		4^{th} order models	
Pressure	0.9954	0.9956	0.9957
F_x	0.9969	0.9969	0.9970
F_y	0.9992	0.9988	**0.9992**
F_z	0.9979	0.9978	0.9979
M_x	0.9984	0.9977	0.9984
M_y	0.9979	0.9970	0.9979
M_z	0.9980	0.9971	0.9980
		5^{th} order models	
Pressure	0.9965	0.9974	**0.9977**
F_x	0.9982	0.9978	**0.9984**
F_y	0.9987	0.9973	0.9988
F_z	0.9987	0.9984	**0.9989**
M_x	0.9984	0.9951	**0.9986**
M_y	0.9989	0.9942	**0.9989**
M_z	0.9981	0.9941	**0.9982**

From these results we see that the 5^{th} order RS fit performs the best for all of the load cases, except for F_y where the 4^{th} order RS performed better. A visual comparison of the lowest and highest performing models are shown in Figures 7.11 and 7.12. The results for the remaining five load cases are available in Appendix F. Each of these plots show 2 393 820 points of comparison.

From all these results, we can see that the RS models approximate the structural behaviour of the complete header box model well, with R-squared values ranging between 0.9977 and 0.9992. Thus a designer can use this meta-model with a high degree of confidence to predict stresses on the entire body of the header box within 10 % of the actual sampled values. Further analysis of the visual comparison plots also show that the critical stresses in each design case, which correspond to the comparison points seen in the top right hand corner of each graph, have an even tighter grouping and that 94.3 % of these predicted critical stresses lie within 5 % of the actual sampled values.

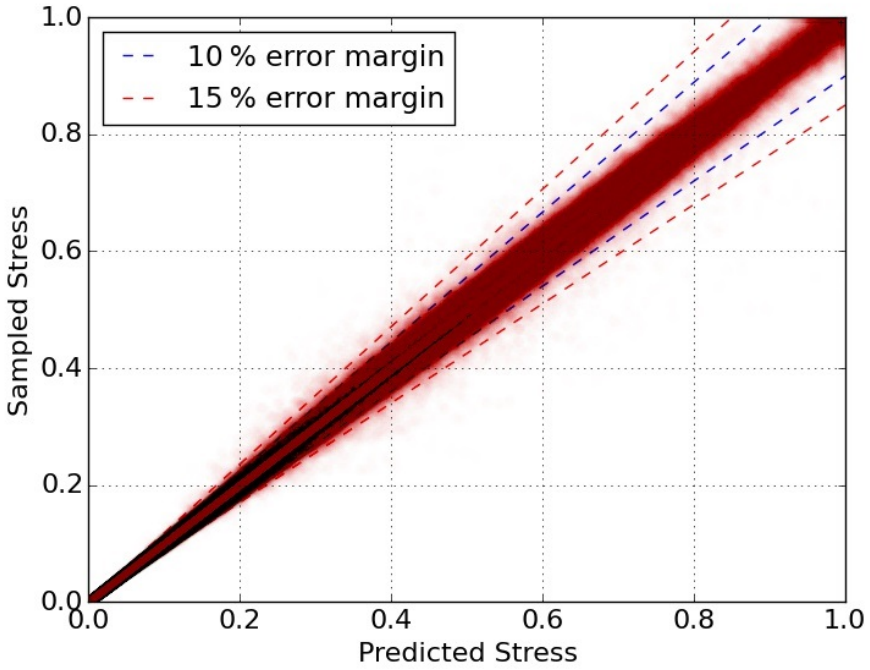

Figure 7.11: Lowest scoring model based on testing set: $R^2 = 0.9977$

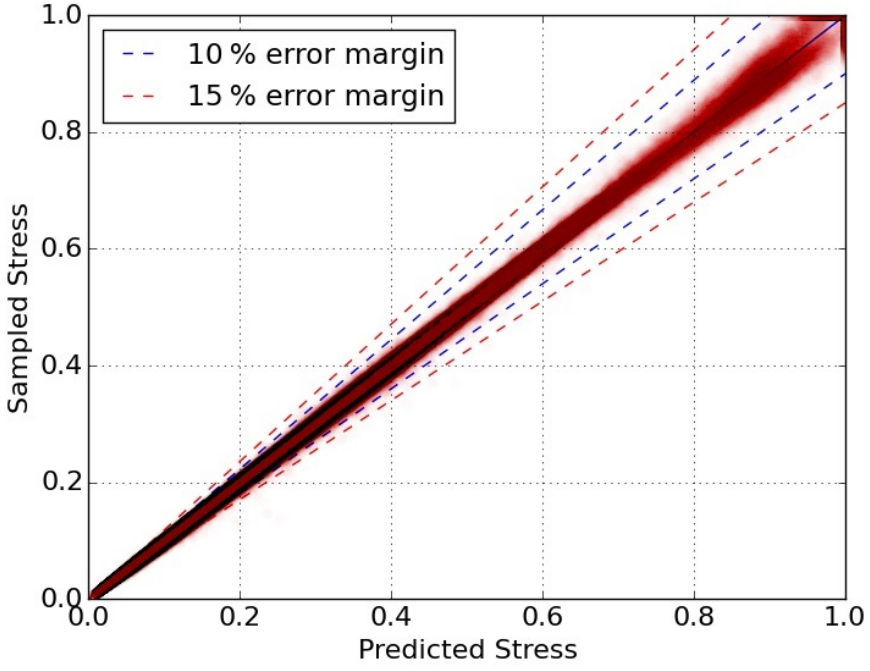

Figure 7.12: Highest scoring model based on testing set: $R^2 = 0.9992$

7.6 Results discussion

Using the final meta-model that was constructed, a designer can now get a complete picture of the structural behaviour of the body of a plug type header box. Two examples of such results are shown in Figures 7.13 and 7.14.

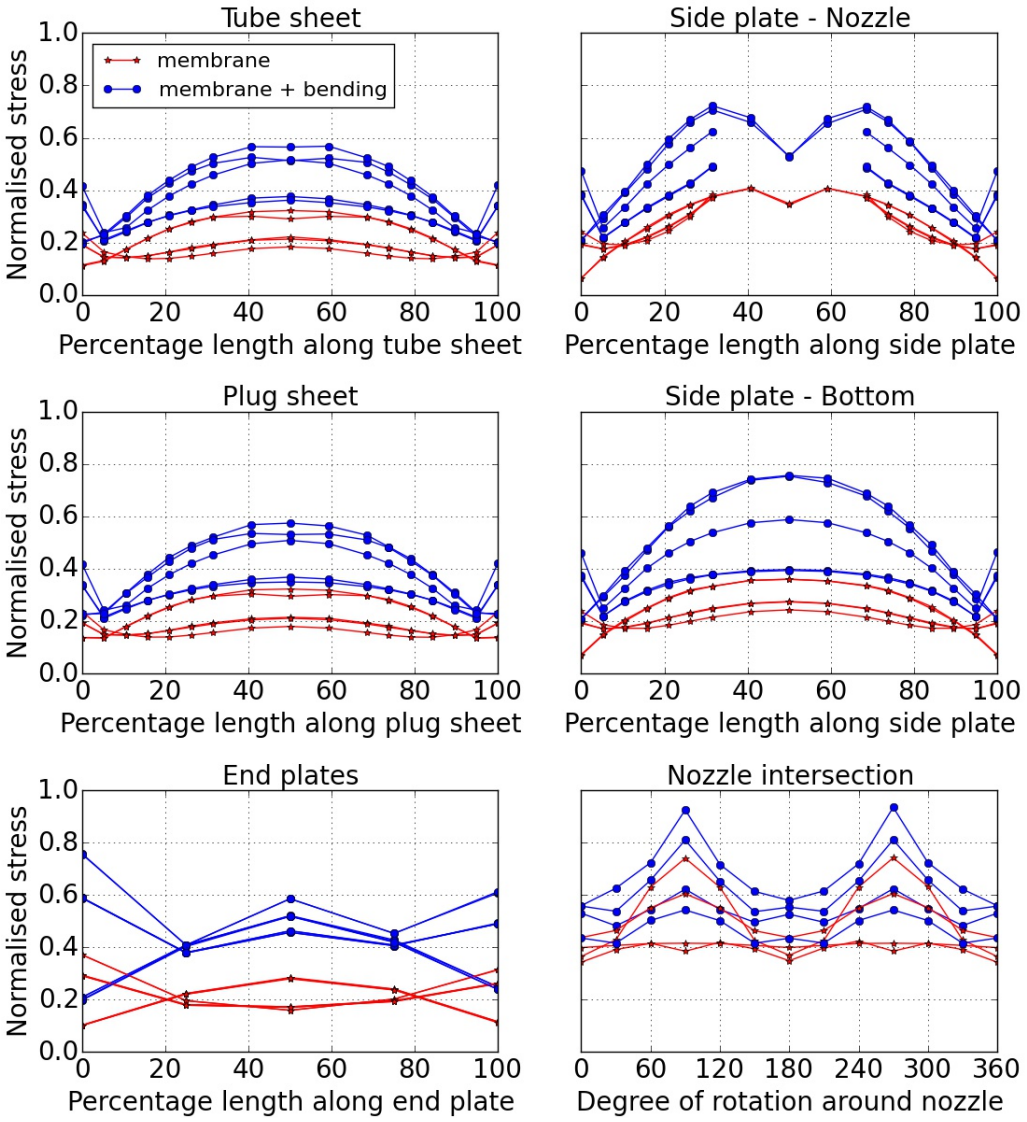

Figure 7.13: Example results predicted by meta-model for load case *Pressure*

From the results in Figures 7.13, which is for the load case *Pressure*, we see how the stresses in the plug sheet, tube sheet and bottom side plate all reach a maximum at the centre of the header box. For the side plate with the nozzle, we see how the stress in the area around the nozzle decrease. For all four of these plates we also see how the stresses tend to decrease closer to the end

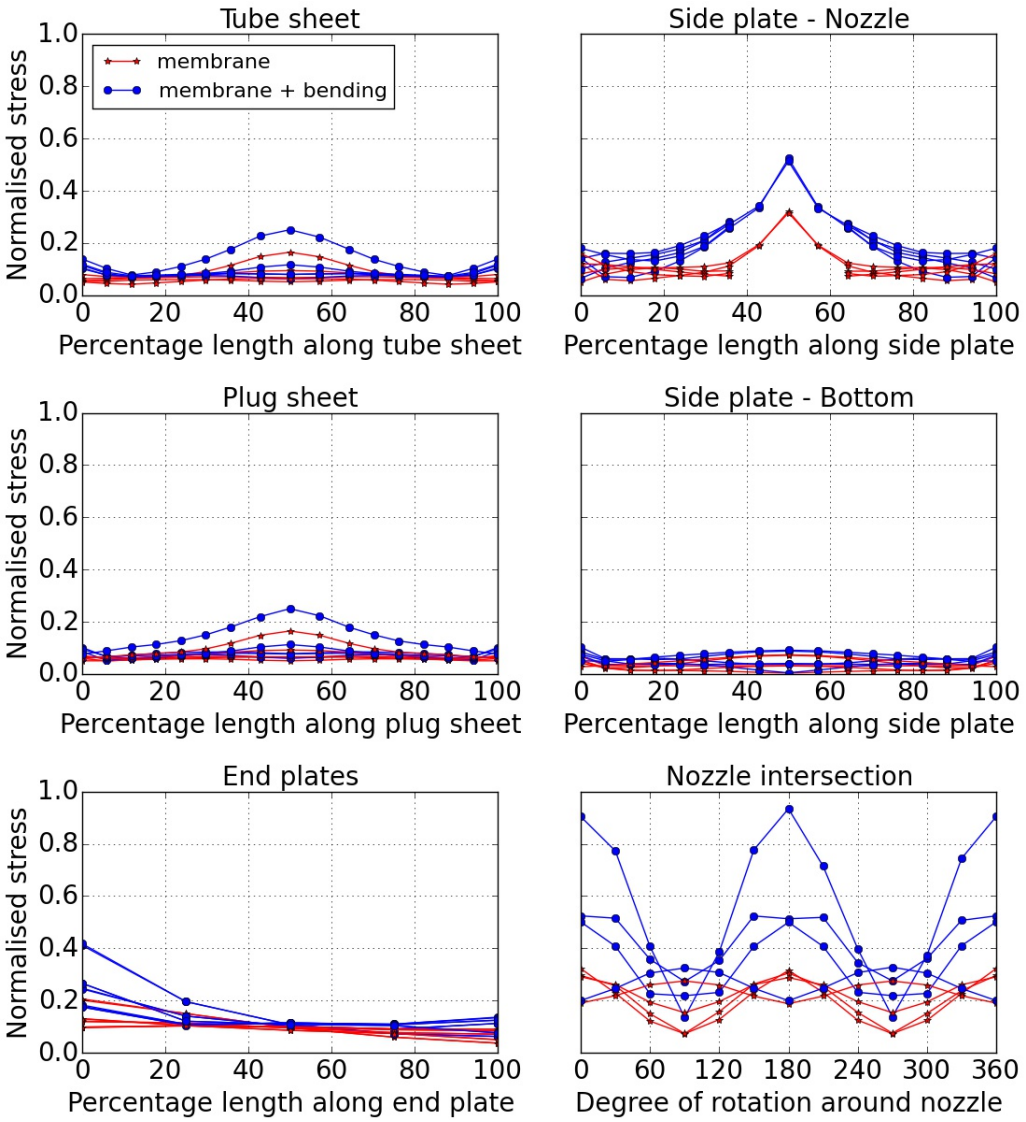

Figure 7.14: Example results predicted by meta-model for load case F_x

plates of the header, most likely due to the stiffness provided by the end plates at the edge of the box. The sudden increase in stress where these plates meet the end plate can be attributed to stress concentrations due to the geometric discontinuity at the edge of the plates. The same increase in stress can also be seen in the results for the end plates at their edges. The results for the nozzle again show the twin peaked form first seen in Chapter 5. The benefit of seeing these nozzle intersection results here is that they can now be placed into context with the stresses on the remaining parts of the header box's body. For the case shown, we can see that the stresses at the nozzle intersection are substantially larger than the stresses in the remainder of the header box body.

In Figure 7.14 we can see how the nozzle load F_x primarily causes stresses at the centre of the four larger sides of the header box. The pattern seen on the end plates can be attributed to the effect of the new boundary conditions applied via the tabs of the header box. Finally, the nozzle stresses again have the twin peaked form. From these results we can clearly see that for this case, the nozzle load applied induced a much larger stress at points around the nozzle intersection than in the remainder of the box. By viewing a more detailed plot of there results, as seen in Figure 7.15, we can see than this peak stress occurs at the base of the nozzle where it meets the side plate (refer to Figure 7.4 for SCP placement guide).

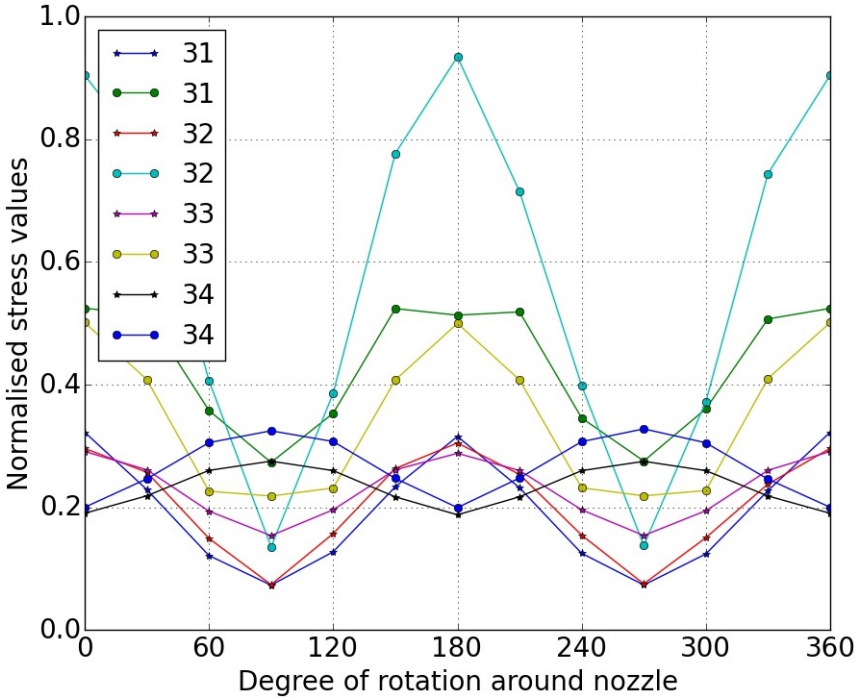

Figure 7.15: Detailed results of stresses at nozzle intersection predicted by meta-model for load case F_x

In its completed form, this meta-model is a powerful interactive tool which provides designers with results about the structural behaviour of the entire body of a plug type header box. In practice, any final design, which incorporates components that are not covered by the guidelines provided in Division 1 of the ASME code, will still have to be validated using an accredited alternative design method, usually by means of a complete FE analysis. With this meta-model however, the current design methods can be greatly enhanced as a user will be able to perform a larger number of design iterations in real time, with results similar to those of a detailed FE analysis. By coupling this capability with a suitable optimisation algorithm, the user will stand a greater chance of finding an optimal design before moving to the costly final step of having it validated by a FE analysis.

Chapter 8

Discussion

8.1 Meta-model performance in relation to training set size

In Chapters 6 and 7 several cases were studied where three or more meta-models (referred to as sub models earlier) were trained to all model the behaviour of a single structure with a given set of design variables. Each of these sub models were however trained using a different number of sample points so that the relationship between the number of training points and the performance of these models could be studied. The results of these studies will be discussed here.

In Chapter 6, three such performance studies were undertaken based on a set of models that were being used to predict how the stresses in the body of a header box are affected by the presence of a nozzle. The details of the three models can be found in Sections 6.5, 6.6 and 6.7.

The number of points used to train each of the sub models in these performance studies was based on the number of unknowns corresponding to the 5^{th} order RS model required for fitting the data (for ease of reference, whenever the term 'the number of unknowns' is used in this section, it will refer to the number of unknowns in the corresponding 5^{th} order RS model). For each of the models at hand, three sub models were trained, using three, six and nine times more training points than the number of unknowns (thus there are three overall models, each with three submodels). The R-squared performance results, compared to the number of training points used, for each of the three overall meta-models are shown in Figures 8.1, 8.2 and 8.3.

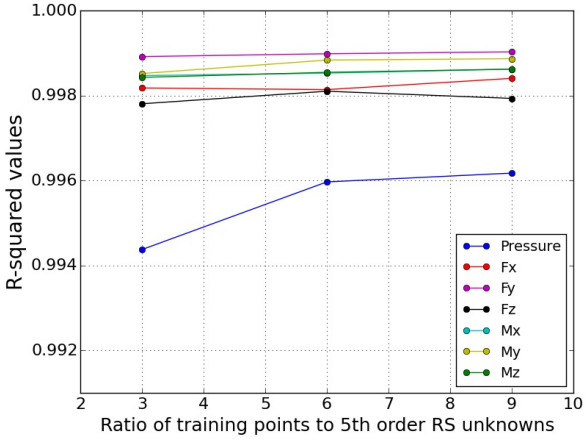

Figure 8.1: *R*-squared values based on testing set vs relative size of training set for partial header box model

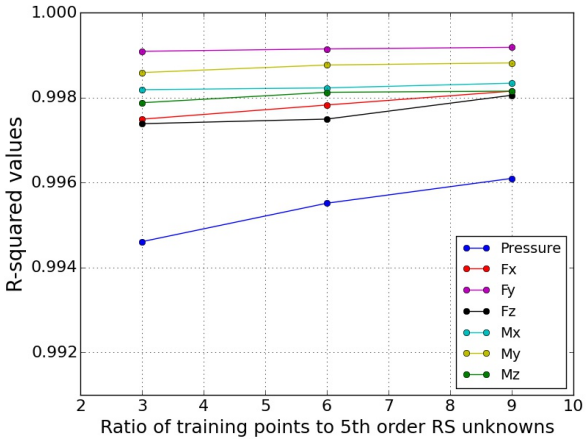

Figure 8.2: *R*-squared values based on testing set vs relative size of training set for partial header box model with experimental equivalent material

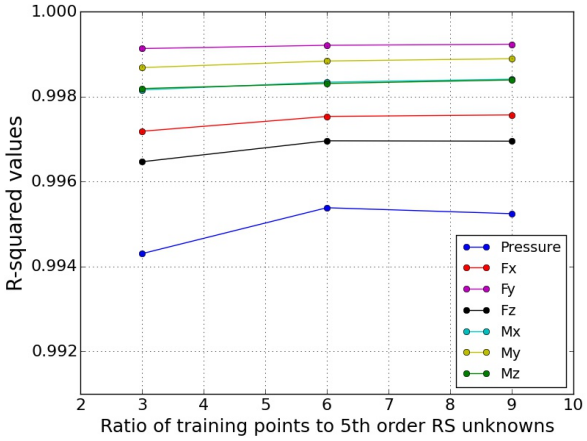

Figure 8.3: *R*-squared values based on testing set vs relative size of training set for partial header box model with basic equivalent material

From these results we can see that there is a general trend of increased performance with the increase in the number of training points, but that it does not affect the performance of all the load cases to the same extent. The load case seeing the largest increase in performance was the *Pressure* load case, while the remaining load cases only saw incremental performance increases. In some cases however, a decrease in performance can be seen with an increased number of training points. While this may appear unexpected, these decreases are not significant in size and can be attributed to the fact that the R-squared values in question are based on an independent and finite set of testing data, which is not fully capable of representing the true function behaviour. These values are thus only approximations of the models' performance and may vary somewhat based on the relationship between the distribution of the training and testing data.

Based primarily on the results of the *Pressure* load case, a greater increase in performance can be seen when enlarging the size of the training set from three to six times the number of unknowns, than when moving from six to nine. In general the overall performance improvement, even for the large increase in the number of training points, is relatively small. This would seem to indicate that a performance plateau has already been reached at or before the point where there are three times more training points than unknowns.

Based on these results, it was decided to include an additional sub model when studying the final model, where only one and a half times more training points than unknowns would be used. The details of the model to which this idea was applied to can be found in Section 7.4. The results of this new performance comparison study are shown in Figure 8.4.

From these results, a definite performance increase can be seen when the number of training points are increased from one and a half to three times the number of unknowns. Beyond this point however, the same performance behaviour as before is observed, where only a marginal performance increase is obtained, even for a large increase in the number of training points.

These results were confirmed by the plot shown in Figure 8.5, which tracks the percentage test results that the four sub models were able to predict within 5 % of the sampled values. Here again we see a distinct performance increase when the number of training points are increased from one and a half to three times the number of unknowns. After this point however, only a slow performance increase can be seen, even for a significant increase in the number of training points.

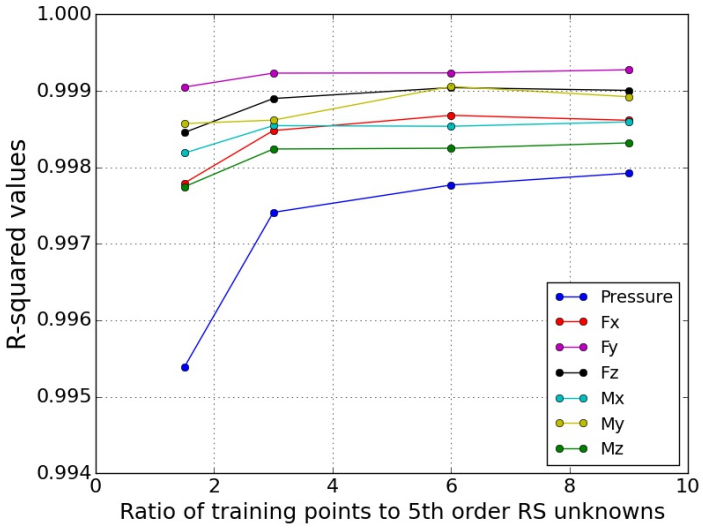

Figure 8.4: R-squared values based on testing set vs relative size of training set for complete header box model with basic equivalent material

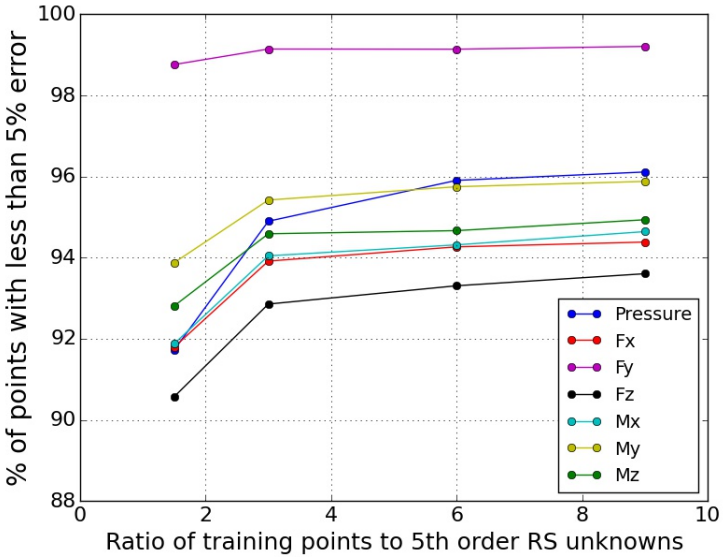

Figure 8.5: Percentage of points with error less than 5 % vs relative size of training set for complete header box model with basic equivalent material

These results would suggest that when constructing meta-models of this type, computational effort will be best spent using up to three times more training points than unknowns. After this point, a very large increase in the number of training points will be required in order to significantly improve the performance of these models.

8.2 Value of performing multiple regressions

In this study two separate SVD regression analyses were performed while fitting the RS models used to approximate the structural behaviour of the header box. In each case, a different tolerance was used to determine the number of non-zero singular values the solution matrix **X** had and thus the rank of the matrix. When using a SVD regression, this influences the size of the portion of the **U**, **V** and **S** matrices that are employed as part of the regression calculations and in turn possibly influence the quality of the models being fit (refer to Sections 3.2.1 and 5.3).

The point at which a singular value is deemed effectively equal to zero, for the 1^{st} SVD regression analysis, was taken as 2^{-53} times the largest singular value. For the 2^{nd} SVD regression analysis, this limit was taken as 2^{-52} times the largest singular value times the largest of the number of rows or columns.

Table 8.1 shows the relevant rank calculations for the solution matrices linked to the meta-models whose results were discussed in Chapters 5, 6 and 7. Take note that while many individual RS models were fit during the course of constructing a single meta-model, they were all fit using one of three solution matrices in each case. This is because all the RS fits are based on the same universal set of design parameters (dimensions and non-dimensional parameters). The only variation of the solution matrix is based on the different polynomial expansions applied to the design parameter, based on the order of the RS model being fit.

From the results, we can see that the tolerance used for the 1^{st} set of SVD regression analyses, which was smaller than that for the 2^{nd} set of SVD regression analyses, classified more matrices as having a full or high rank. Thus, a larger portion of the **U**, **V** and **S** matrices were often employed as part of these calculations (refer to Section 3.2.1 for technical details). For the 2^{nd} set of SVD regression analyses, the opposite was true where only a few of the 3^{rd} order solution matrices achieved full rank and the remaining solution matrices were classified as rank deficient. These results also show that the rank of the matrices, for the first and second tolerance, are affected by both the model order and the number of variables being considered and that an increase of either of these factors resulted in a general decrease of matrix rank.

Based on the 'no free lunch' theorem, neither of these approaches could be assumed to always work better than the other for all models being fit. Thus, they were both tested so that the performance of each could be measured. While it is not practical to reproduce here all the comparative performance results for the models trained in this study using these two approaches, a representative exert is given in Tables 8.2 and 8.3 to aid the discussion. These are the R-squared performance results for the final models in Chapters 6 and

Table 8.1: Rank calculations for solution matrices used during study

Order of RS fit	Full rank value	Matrix rank (Tolerance 1)	Rank status	Matrix rank (Tolerance 2)	Rank status
Initial partial header box model 7 variables - 2 500 sample points					
3^{rd}	120	120	Full rank	120	Full rank
4^{th}	330	330	Full rank	323	Rank deficient
5^{th}	792	787	Rank deficient	649	Rank deficient
Partial header box with no equivalent material model 6 variables - 4 500 sample points					
3^{rd}	84	84	Full rank	84	Full rank
4^{th}	210	210	Full rank	192	Rank deficient
5^{th}	462	446	Rank deficient	330	Rank deficient
Partial header box with experimental equivalent material model 7 variables - 7 200 sample points					
3^{rd}	120	120	Full rank	120	Full rank
4^{th}	330	330	Full rank	273	Rank deficient
5^{th}	792	729	Rank deficient	457	Rank deficient
Partial header box with basic equivalent material model 8 variables - 11 700 sample points					
3^{rd}	165	165	Full rank	164	Rank deficient
4^{th}	495	495	Full rank	367	Rank deficient
5^{th}	1287	1132	Rank deficient	595	Rank deficient
Complete header box with basic equivalent material model 10 variables - 27 300 sample points					
3^{rd}	286	286	Full rank	282	Rank deficient
4^{th}	1001	1001	Full rank	694	Rank deficient
5^{th}	3003	2667	Rank deficient	1127	Rank deficient
Complete header box model 12 variables - 18 600 sample points					
3^{rd}	455	455	Full rank	449	Rank deficient
4^{th}	1820	1820	Full rank	1091	Rank deficient
5^{th}	6188	4925	Rank deficient	1728	Rank deficient

7 respectively. These results correspond to the portions in Table 8.1 which are labelled 'Partial header box with basic equivalent material model' and 'Complete header box model'.

Table 8.2: R-squared values based on testing set for partial header box with basic equivalent material model

Load case	SVD Regression 1	SVD Regression 2	Combined Model
		3^{th} order models	
Pressure	0.9764	0.9764	0.9764
F_x	0.9900	0.9900	0.9900
F_y	0.9977	0.9977	0.9977
F_z	0.9893	0.9893	0.9893
M_x	0.9925	0.9925	0.9925
M_y	0.9961	0.9961	0.9961
M_z	0.9903	0.9902	0.9903
		4^{th} order models	
Pressure	0.9929	0.9931	0.9930
F_x	0.9976	0.9970	**0.9976**
F_y	0.9992	0.9978	**0.9992**
F_z	0.9969	0.9967	**0.9970**
M_x	0.9984	0.9959	**0.9984**
M_y	0.9989	0.9965	**0.9989**
M_z	0.9984	0.9946	**0.9984**
		5^{th} order models	
Pressure	0.9883	0.9951	**0.9952**
F_x	0.9829	0.9947	0.9954
F_y	0.9640	0.9932	0.9939
F_z	0.9898	0.9957	0.9962
M_x	0.9718	0.9891	0.9916
M_y	0.9766	0.9905	0.9919
M_z	0.9599	0.9844	0.9882

Table 8.3: R-squared values based on testing set for complete header box model

Load case	SVD Regression 1	SVD Regression 2	Combined Model
		3^{th} order models	
Pressure	0.9829	0.9829	0.9829
F_x	0.9881	0.9881	0.9881
F_y	0.9976	0.9976	0.9976
F_z	0.9912	0.9912	0.9912
M_x	0.9925	0.9925	0.9925
M_y	0.9834	0.9834	0.9834
M_z	0.9905	0.9905	0.9905
		4^{th} order models	
Pressure	0.9952	0.9955	0.9955
F_x	0.9969	0.9969	0.9970
F_y	0.9992	0.9988	**0.9992**
F_z	0.9979	0.9978	0.9979
M_x	0.9984	0.9977	0.9984
M_y	0.9979	0.9970	0.9979
M_z	0.9980	0.9971	0.9980
		5^{th} order models	
Pressure	0.9964	0.9974	**0.9976**
F_x	0.9982	0.9978	**0.9984**
F_y	0.9987	0.9973	0.9988
F_z	0.9987	0.9984	**0.9989**
M_x	0.9984	0.9951	**0.9986**
M_y	0.9989	0.9942	**0.9989**
M_z	0.9981	0.9941	**0.9982**

When looking at the results for the different order models in these two cases, we see that for the 3^{rd} order models, which yielded a similar rank value for both tolerances, the results are near identical. For the 4^{th} order models, where the rank numbers differ somewhat more, we start to see more of a distinction between the results, but the difference is not large. Finally, looking at the 5^{th} order models, where the rank numbers differ substantially, we see clear variations in the results predicted by the two regression analyses. However, the results do not favour either one of these as always being more accurate.

In the case of the 5^{th} order results in Table 8.2 we see that the performance results of the two regression analyses differ significantly and that the 2^{nd} set of SVD regression analyses performs better. When looking at the same results in Table 8.3 , however, the opposite is true with the 1^{st} set of SVD regression analyses performing better and with a smaller difference in results than previously seen. It would thus appear that there is no fixed pattern with which to determine whether using a low or high tolerance value for determining matrix rank will yield better performing results. The results thus need to be compared on a case by case basis to identify the best performing models.

8.3 Modelling limitations

Traditionally, when constructing a meta-model, the most expensive part of the work is collecting the data required for training a model. Many times this data may be limited and substantial effort is spent testing and finding the best possible models with which to approximate a system or structure's behaviour.

Owing primarily to the use of the automation tool set and software developed for this study, the time required to construct, simulate and post-process the detailed three dimensional FE analyses used to generated the training data for this study was vastly reduced. This allowed for much larger training sets to be generated than usual.

Additionally, in order to model the overall behaviour of the structures considered in this study, tens of thousands of individual meta-models had to be trained in each case to predict the stresses down to their component levels all across the structure. In the case of the final model in Chapter 7, 36 036 such meta-models had to be trained. This requirement, coupled with the larger than usual training set being used, led to new limitations being encountered with regard to the type and number of mathematical models that could be tested while approximating the data. These limitations lead to some initial plans of using more advanced machine learning algorithms such as SVR and Kriging to approximate the data being abandoned in favour of simpler RS models, as the RS models were less computationally expensive to train. To put this decision

into context, consider the following. When the idea of training SVR and Kriging models was tested, the computational expense of training these models was found to be between one and two orders of magnitude greater than that required to fit RS models. Coupling this information to the fact that roughly 75 % of all the computational resources used during the course of this study was devoted just to training RS models, it becomes clear that the alternative would not have been feasible. Considering how well the RS models were able to approximate the behaviour of the models discussed in this study, it may be reasonable to surmise that more advanced algorithms may not be required for structural meta-models of this type.

A procedure commonly employed in conjunction with RS modelling is trimming, which is typically applied by means of step-wise regression. This is a process whereby redundant terms in the RS expansion or terms poorly characterised by the data are removed from the model to make it less complex. Due to the large number of models that had to be trained in this study, it was however also not practical to implement step-wise regression as it is an iterative process of training models, removing terms thought to be redundant and then retraining the model to ensure that they still performed as expected.

8.4 Overcoming limitations to scaling in future work

Inevitably, future work in this field of research will involve building more complex models of plug type header boxes and other pressure vessels with more variables that can be controlled. If the procedures used thus far are to be linearly scaled up for such endeavours, it will require an increase in the number of FE analyses to be performed to gather data for training and testing purposes and more complex models will have to be trained. At some point, direct scaling of these methods will be limited by the availability of computational resources. Careful consideration should therefore be given in the future to finding methods that either reduce the number of required sample points or reduce the computational expense of the process in some other way. A few ways of possibly achieving this are discussed below.

Finding variables that do not affect the stresses in certain regions of the header box. An example of this could for instance be that the thickness of the end plates does not affect the stresses occurring at the nozzle intersection. The terms which relate to the end plate thickness can then be removed from the polynomial expansion of the RS model describing a stress at the nozzle intersection, thus reducing the complexity of the model being trained and the associated computational expense.

Identifying variables that have lower order behaviour. For the RS models fit in this study, complete polynomial expansions with all available interaction terms between the variables were used. This meant that when a 5^{th} order RS model was fit, all the variables were modelled as having 5^{th} order behaviour and interaction terms of 4^{th} order and lower. If variables can however be identified that only showcase low order behaviour, such as 2^{nd} or 3^{rd} order, then only these relevant terms need to be included in the RS models. This will reduce the number of unknowns and thus also the number of training and test points required. Additionally, this will also reduce the computational expense of fitting the RS models.

Improve methods for training RS models. Due to the nature of the models constructed, a somewhat unique situation presents itself with regards to the RS models used to approximate the data. As explained earlier in this chapter, while thousands of RS models are trained to construct the components of each meta-model, only a limited number of solution matrices are used. This is because every RS model that is trained relies on the same set of design parameters and the solution matrix only changes when a different order RS expansion is applied to it. Thus for each of the meta-models that were trained in this study where 3^{rd}, 4^{th} and 5^{th} order models were tested, there were only three solution matrices present.

When solving a least squares regression, the solution takes on the form

$$\boldsymbol{b} = (\mathbf{X}^T\mathbf{X})^{-1}\mathbf{X}^T\boldsymbol{y} \tag{8.1}$$

Traditionally, inverting the term $\mathbf{X}^T\mathbf{X}$ is deemed too computationally expensive. In its place alternative methods have been developed to avoid this step and still solve for $\boldsymbol{b}$. However, when only a single solution matrix is used to solve for a large number of RS models advantage can also be taken of the established practise of factorising the system once and then solving multiple times.

The same advantage is available when using SVD regression, where the $\mathbf{U}$, $\mathbf{V}$ and $\mathbf{S}$ matrices need only be calculated once, before being used multiple times. This method was implemented to a certain extent in Chapter 7 and resulted in significant time savings while training the RS models.

When working with SVD, a further step can also be taken to inexpensively test multiple tolerances for the limit used to define a non-zero singular value. In this study, two separate tolerance values were tested for this limit, resulting in different rank values being calculated for the solution matrices and producing different performance results in most cases. The most expensive part of performing a regression via SVD is performing the decomposition to get the

U, **V** and **S** matrices. Once these are calculated however, it becomes trivial to test different tolerance limits, as this effectively only involves using different portions of the **U**, **V** and **S** matrices in the matrix calculations used to calculate $\boldsymbol{b}$ (refer to Section 3.2.1).

8.5 Recommendation for future work

A valuable addition to this research would be to construct a case specific equivalent material meta-model for flat sided pressure vessels. While the equivalent material models in the ASME code are useful, they were originally created with shell-and-tube heat exchangers in mind, where the perforated plate is a round disk. These equivalent material models do not take into account the complete structural effect of heat exchanger tubes and plugs connected to the perforate plates and can thus be made more accurate. Having such a model will expand the capabilities of the meta-models created in this study and enable them to relate more closely to the real world characteristics of these pressure vessels.

Finally, while the research in this study focussed primarily on single chamber plug type header boxes, the same methods can be employed to expand this work and model the structural behaviour of multi-chamber header boxes. The developed methods for constructing these meta-models are however not limited to plug type header boxes and have been formulated in such a manner that they can easily be adjusted to model a wide variety of pressure vessels and other structures.

Chapter 9

Conclusion

The purpose of this study was to construct a full scale meta-model which accurately predicts the structural behaviour of a plug type header box in real time. The first step in the process was to establish a method for performing large numbers of FE simulations, required for generating the data needed to train a meta-model. This was achieved by creating a software tool set which automated the process of setting up, simulating and post-processing the results of a FE analyses. This vastly reduced the time required to generate training data and allowed for much larger training sets to be used in this study than are commonly found when creating meta-models of this kind.

Using this tool set, a less complex meta-model was constructed initially that only modelled the stresses in the region where a nozzle meets the side plate of a header box. This model was successfully used to test the concept of modelling the structural behaviour of a header box and was also used as a test bed for refining the methods employed in the process of constructing meta-models for this study.

Building on this success, a set of more complex meta-models was constructed that predict what structural effects a nozzle has on the body of a header box. The results of these models showed that certain widely used design practices are incorrect in assuming that the presence of a nozzle on a header box always weakens the side plate it is attached to. Additionally, the results also showed that the presence of a header box nozzle affects the stresses experienced by the plates which surround the side plate the nozzle is attached to and that these plates may experience either increased or decreased stresses depending on the dimensions of the nozzle. This too stands in contrast to the commonly used assumption in current design practices that the presence of a nozzle has no effect on any plates adjacent to the side plate it is connected to. Using the models created, a designer will however be able to accurately assess the extent to which the body of a header box is affected by the presence of a nozzle and be able to adjust the relevant stress calculations accordingly.

While constructing these meta-models, full advantage was taken of the ability to generate very large sets of training data, thanks to the automation tool set developed for this study. Instead of generating a single set of training data for every structure being modelled, two training sets were generated and used in different combinations to construct three meta-models for every structure, each time utilising a different number of training points. The results of these models were then used to track how the performance of meta-models of this kind are affected by the number of points used to train them. This information can be employed as a guideline in future studies for deciding on the number of training points to be used.

The final phase of this study was to construct a model of a complete header box structure. This was completed in two stages, starting with a somewhat less complex model, which included all the relevant geometry of a complete header box but did not have as detailed equivalent material capabilities as the final meta-model. This model was again employed to study how the performance of these meta-models are affected by the size of the training set used and the results were used to refine the guidelines already established.

A unique obstacle encountered while constructing the meta-models in this study was that tens of thousands of individual mathematical models had to be trained to construct each meta-model described. This was due to the fact that stresses were being modelled at hundreds of points across the header box bodies and at each point twelve linearised stress components had to be modelled for each of the seven load cases considered. Due to the computational expense associated with training this large number of models, the only feasible approach found was to use RS models to approximate the data, as they are far less expensive to train than other more advance machine learning algorithms such as SVR or Kriging. To still approximate the data accurately, high order RS models had to be employed, which in turn meant that the challenges associated with training the high-dimensional, high order RS models also had to be dealt with. All of these problems were however addressed and appropriate steps were taken to mitigate the risks involved with fitting high order RS models, in order that accurate meta-models could still be constructed without having to reduce the scale of detail and complexity included in the models.

Finally, based on the knowledge accumulated over the course of this study, a complete plug type header box meta-model was created which includes twelve dimensions and material parameters that can be varied. This meta-model can be used to predict the linearised membrane and membrane plus bending stresses occurring across the entire body of the box. Testing showed that the final meta-model achieved the desired goal of providing accurate stress results in real time. Using this model, designers are now able to explore plug

type header box designs, search for optimal designs and identify the overall structural effects associated with altering individual dimensions, all without the limitations usually imposed by cost and time. The field of knowledge surrounding the design of these pressure vessels can benefit greatly from this research, opening up the doors for the implementation of new design methods in the future.

Appendices

Appendix A

Initial test problem - Additional comparison plots

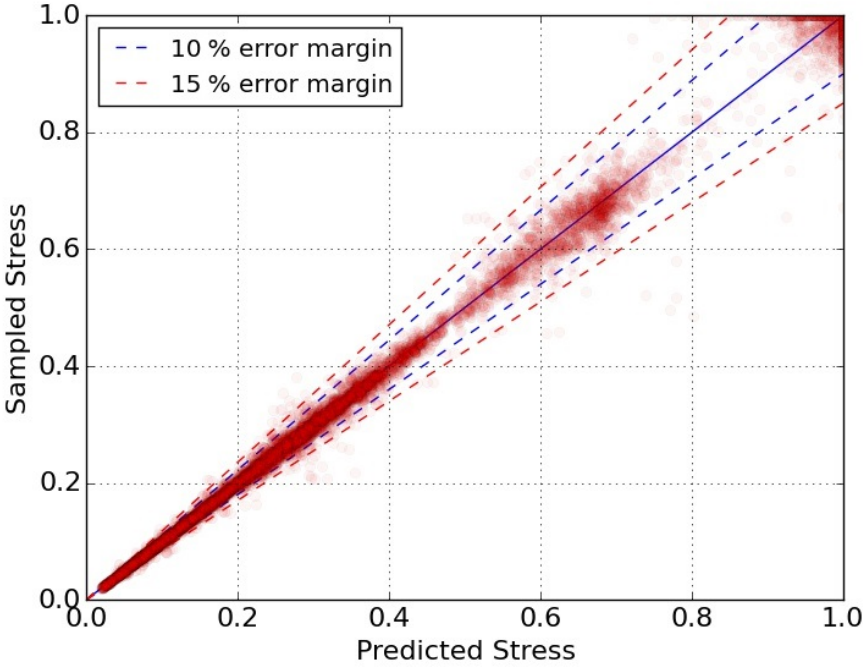

Figure A.1: Sampled vs predicted stress for load case F_x
R-squared based on testing set: 0.9927

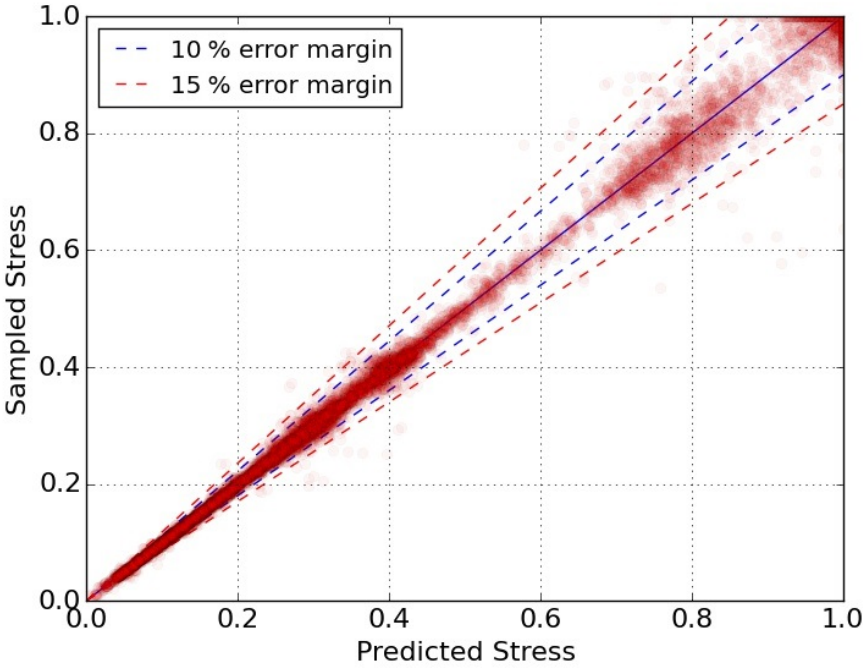

Figure A.2: Sampled vs predicted stress for load case F_z
R-squared based on testing set: 0.9932

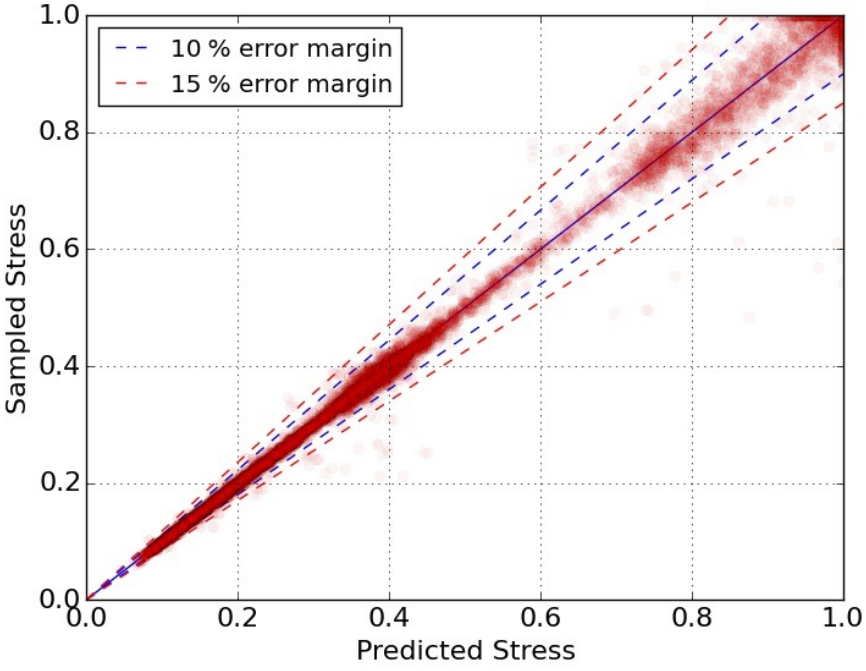

Figure A.3: Sampled vs predicted stress for load case M_x
R-squared based on testing set: 0.9932

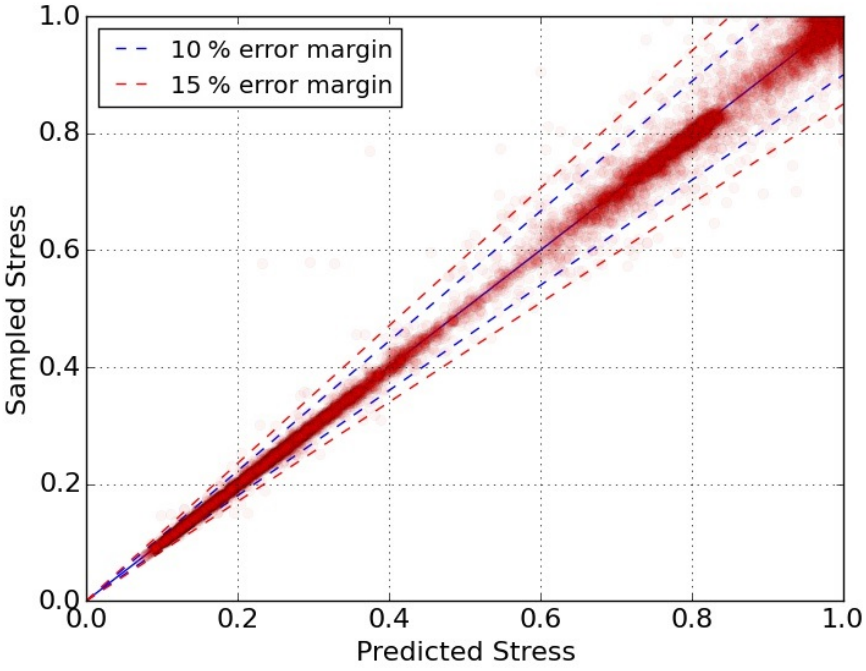

Figure A.4: Sampled vs predicted stress for load case M_y
R-squared based on testing set: 0.9944

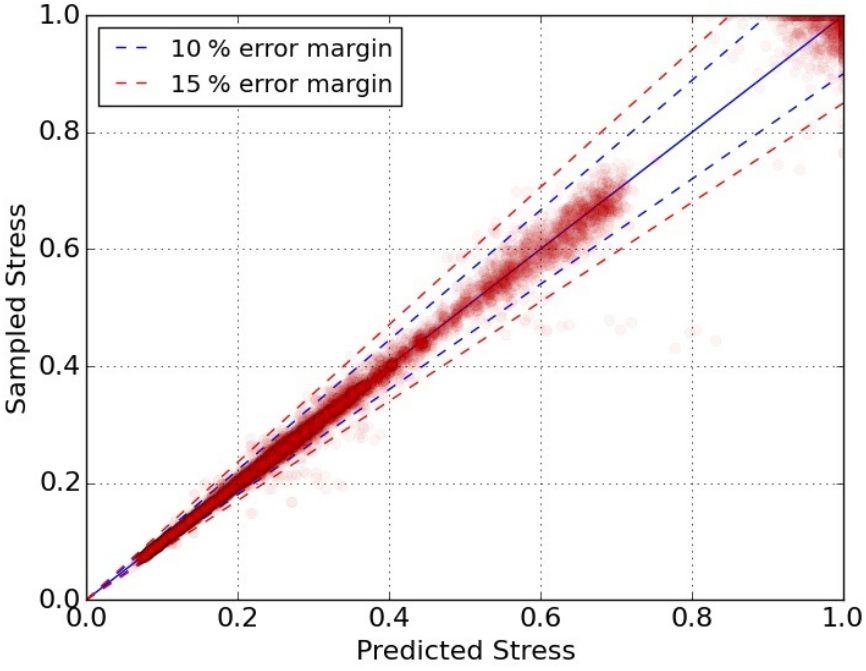

Figure A.5: Sampled vs predicted stress for load case M_z
R-squared based on testing set: 0.9928

Appendix B

First partial header box model - Additional comparison plots

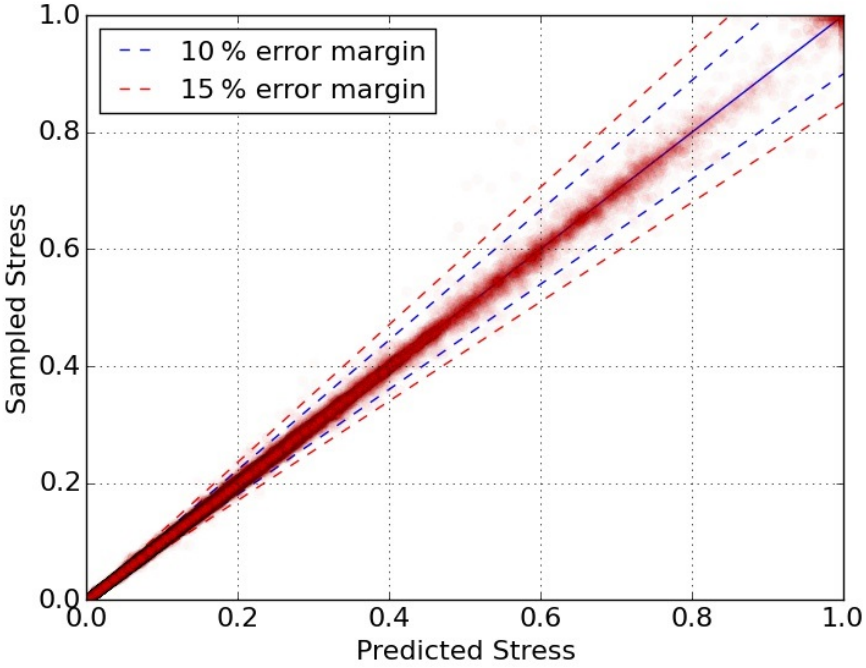

Figure B.1: Sampled vs predicted stress for load case F_x
R-squared based on testing set: 0.9984

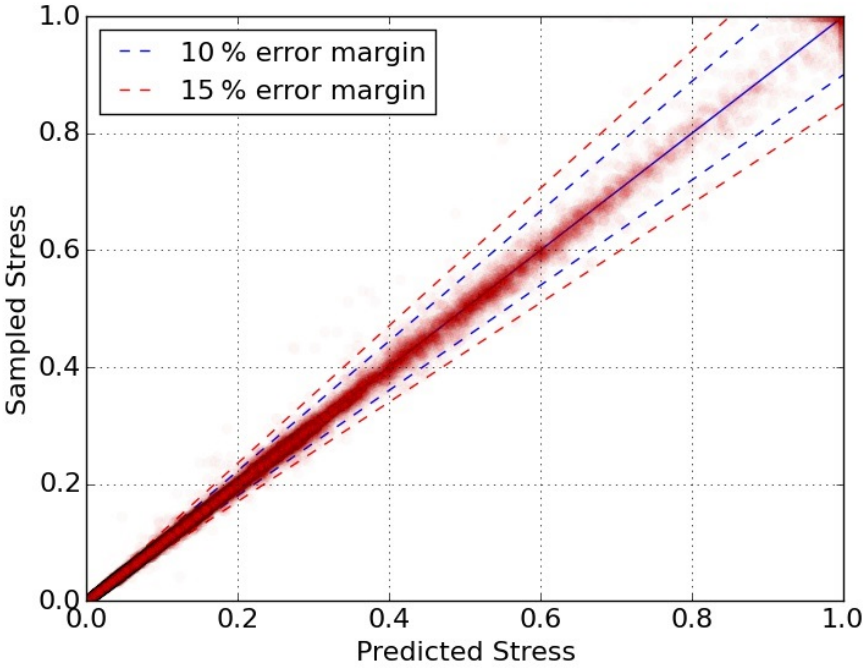

Figure B.2: Sampled vs predicted stress for load case F_z
R-squared based on testing set: 0.9979

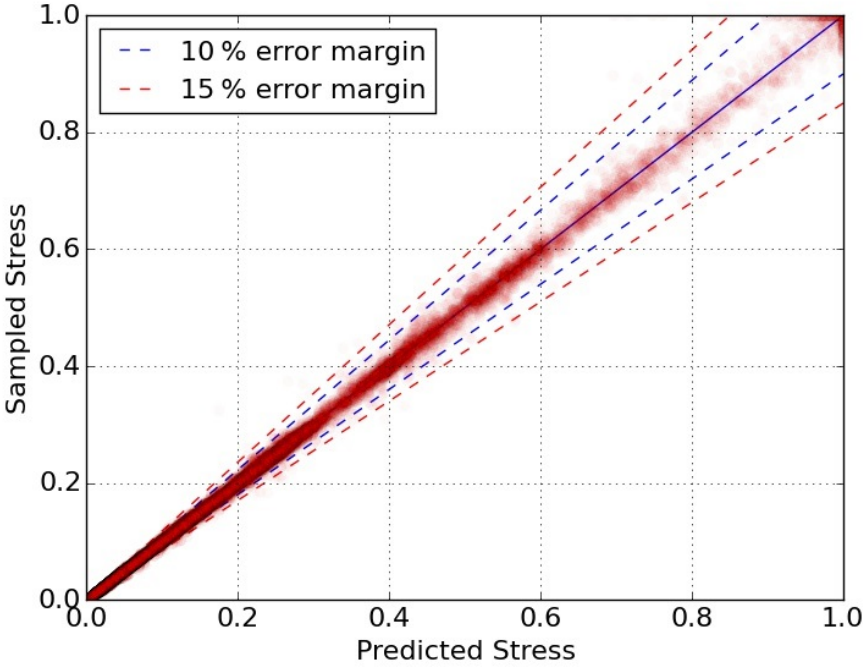

Figure B.3: Sampled vs predicted stress for load case M_x
R-squared based on testing set: 0.9986

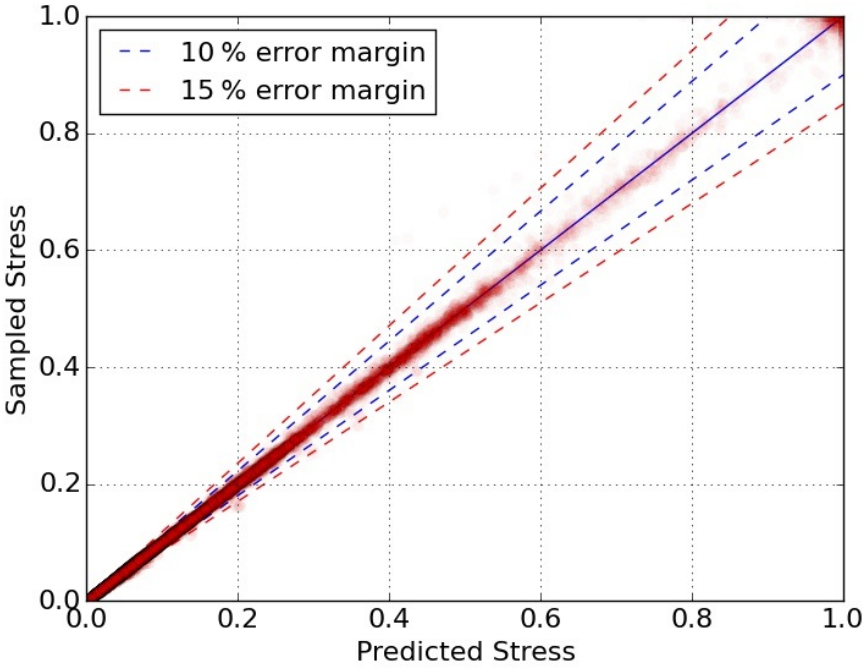

Figure B.4: Sampled vs predicted stress for load case M_y
R-squared based on testing set: 0.9989

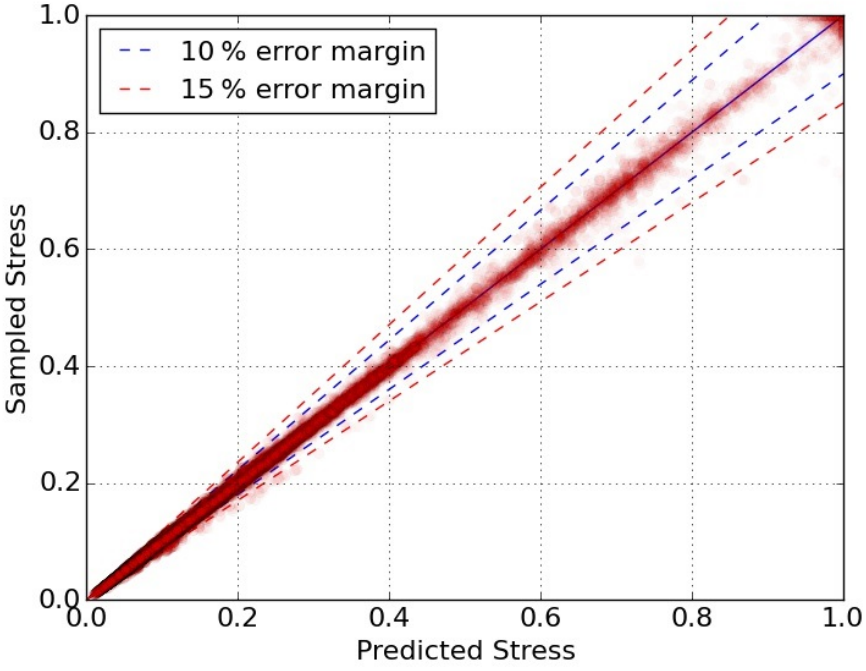

Figure B.5: Sampled vs predicted stress for load case M_z
R-squared based on testing set: 0.9986

Appendix C

Partial header box with experimental equivalent material - Additional comparison plots

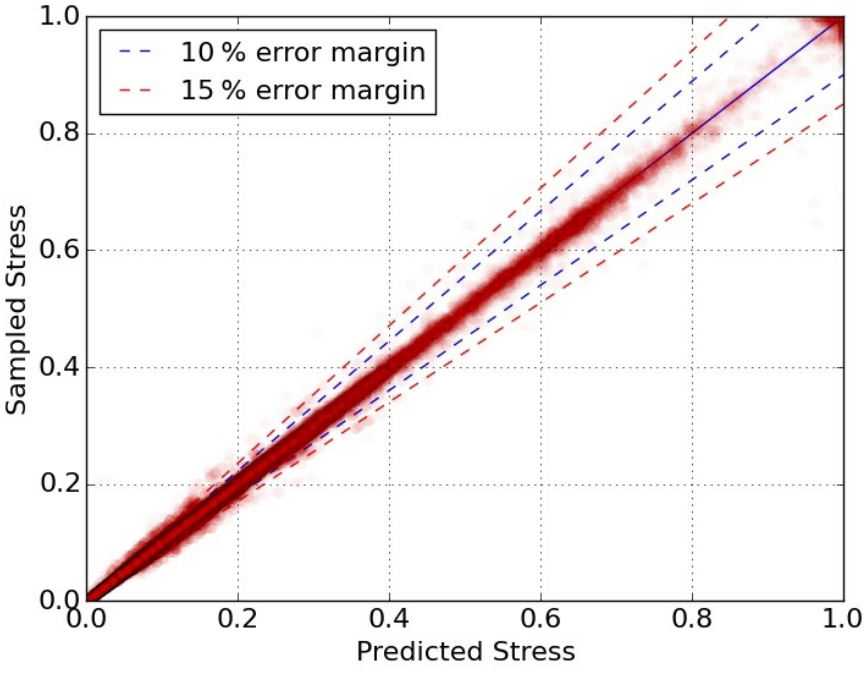

Figure C.1: Sampled vs predicted stress for load case F_x
R-squared based on testing set: 0.9982

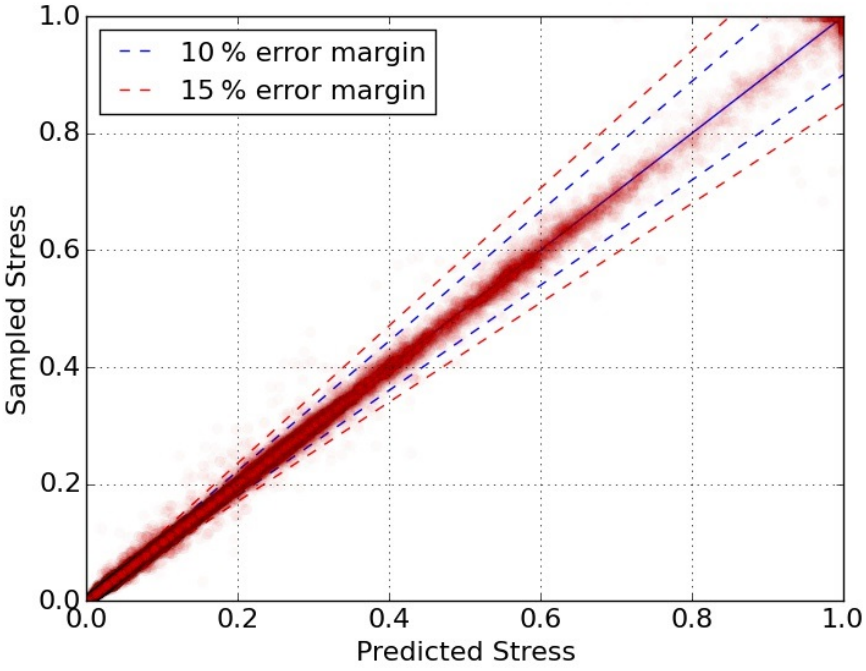

Figure C.2: Sampled vs predicted stress for load case F_z
R-squared based on testing set: 0.9981

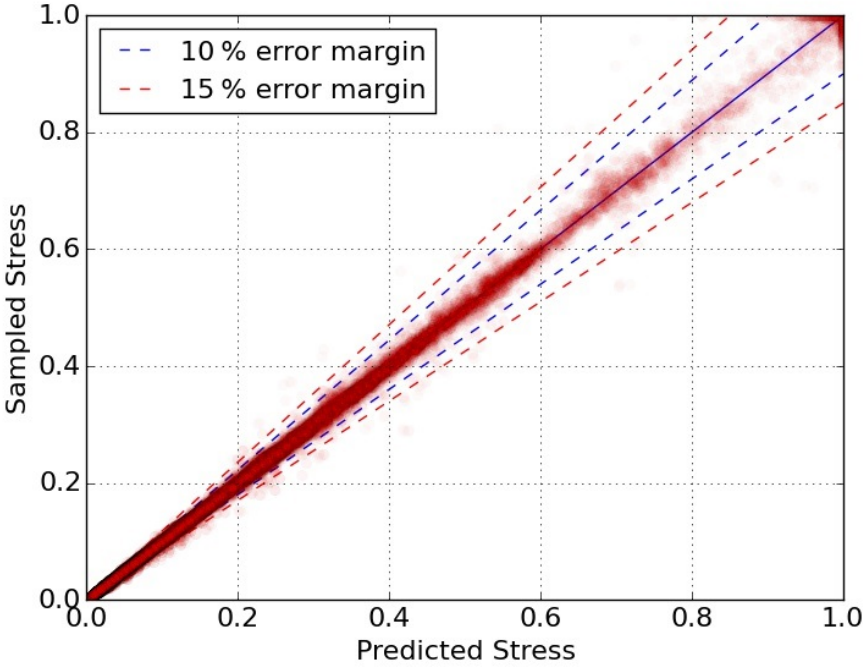

Figure C.3: Sampled vs predicted stress for load case M_x
R-squared based on testing set: 0.9983

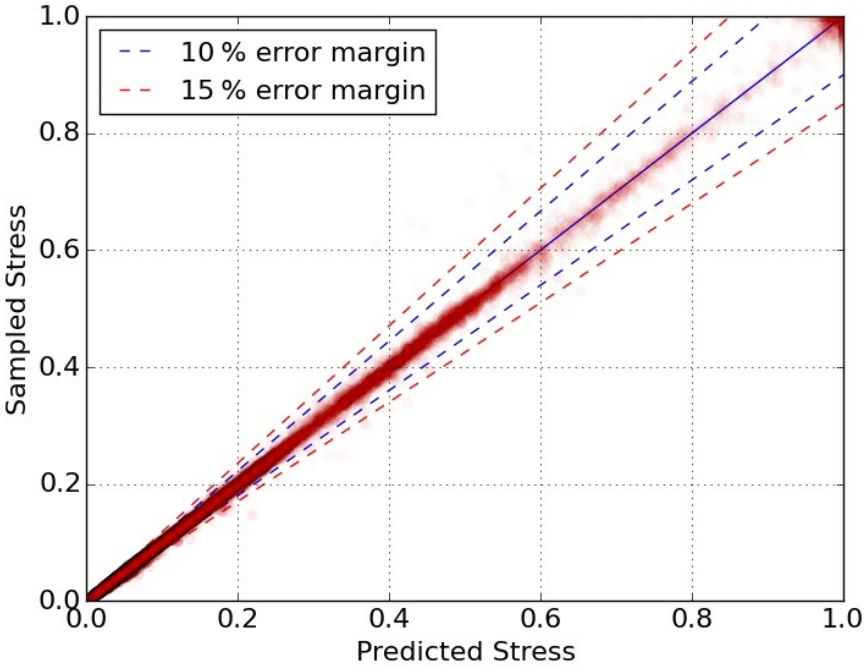

Figure C.4: Sampled vs predicted stress for load case M_y
R-squared based on testing set: 0.9988

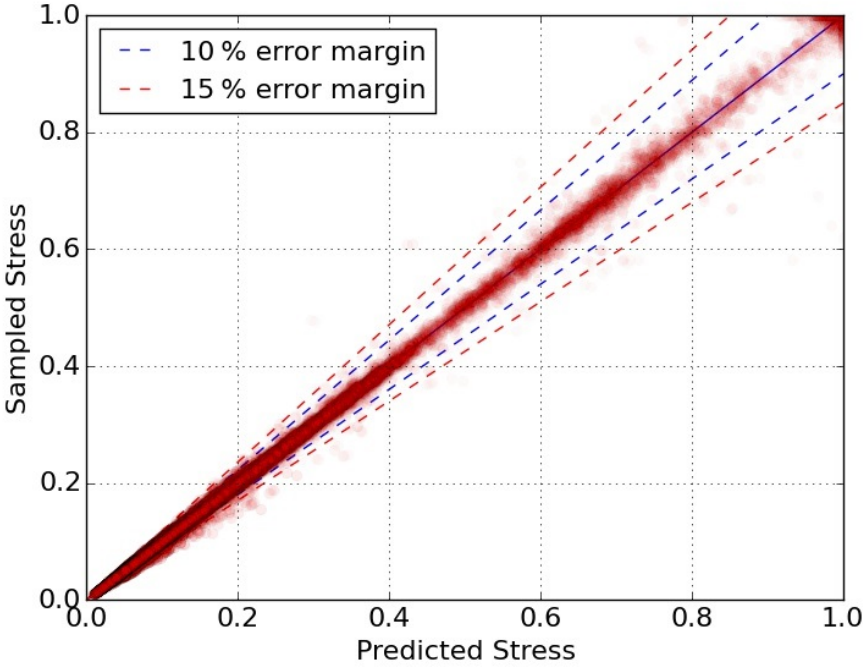

Figure C.5: Sampled vs predicted stress for load case M_z
R-squared based on testing set: 0.9982

Appendix D

Partial header box with basic equivalent material - Additional comparison plots

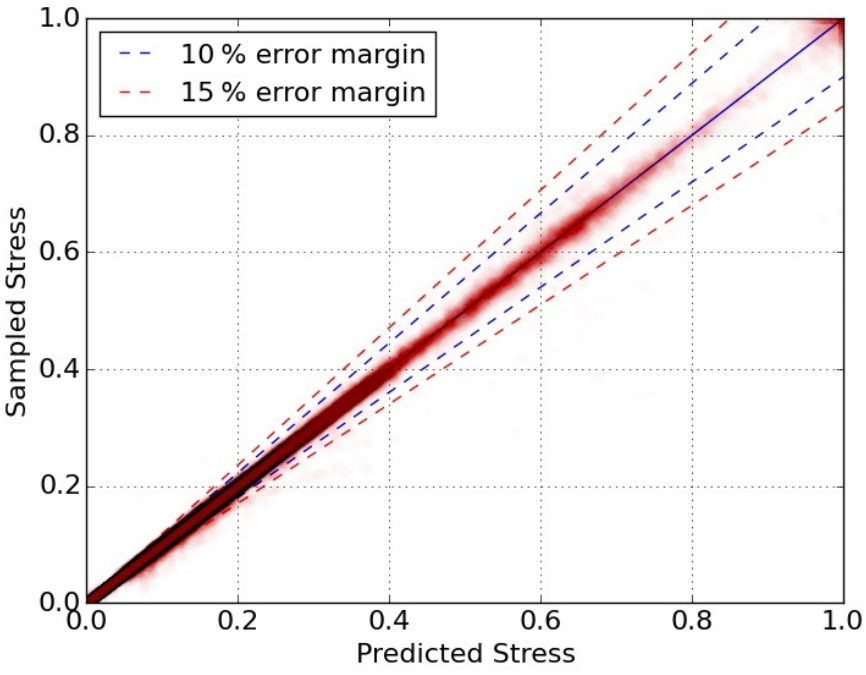

Figure D.1: Sampled vs predicted stress for load case F_x
R-squared based on testing set: 0.9976

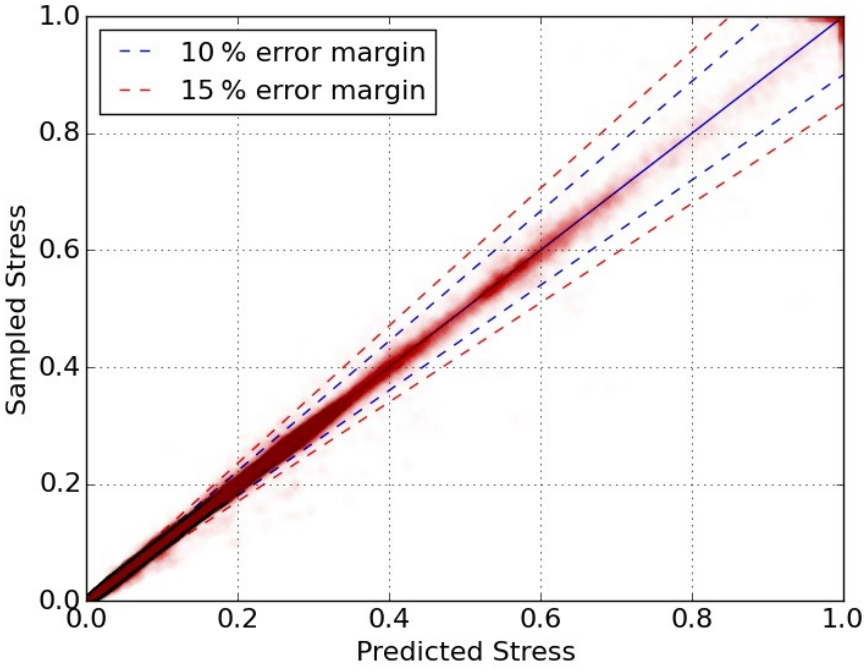

Figure D.2: Sampled vs predicted stress for load case F_z
R-squared based on testing set: 0.9970

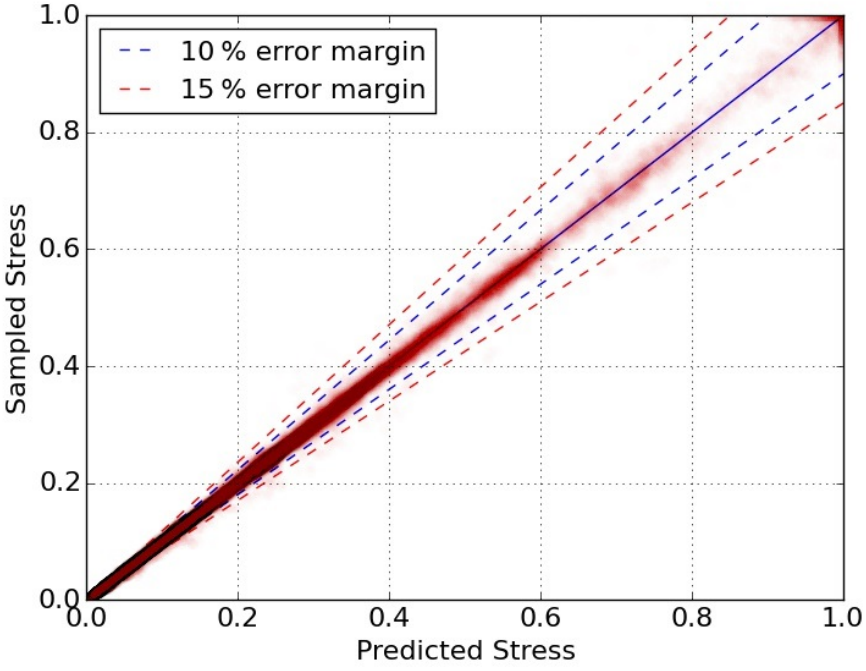

Figure D.3: Sampled vs predicted stress for load case M_x
R-squared based on testing set: 0.9984

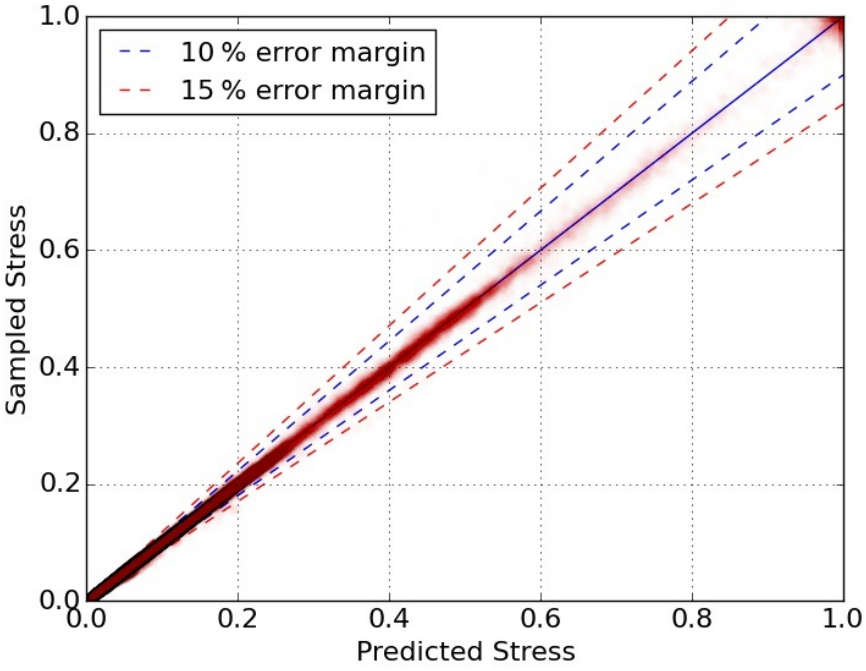

Figure D.4: Sampled vs predicted stress for load case M_y
R-squared based on testing set: 0.9989

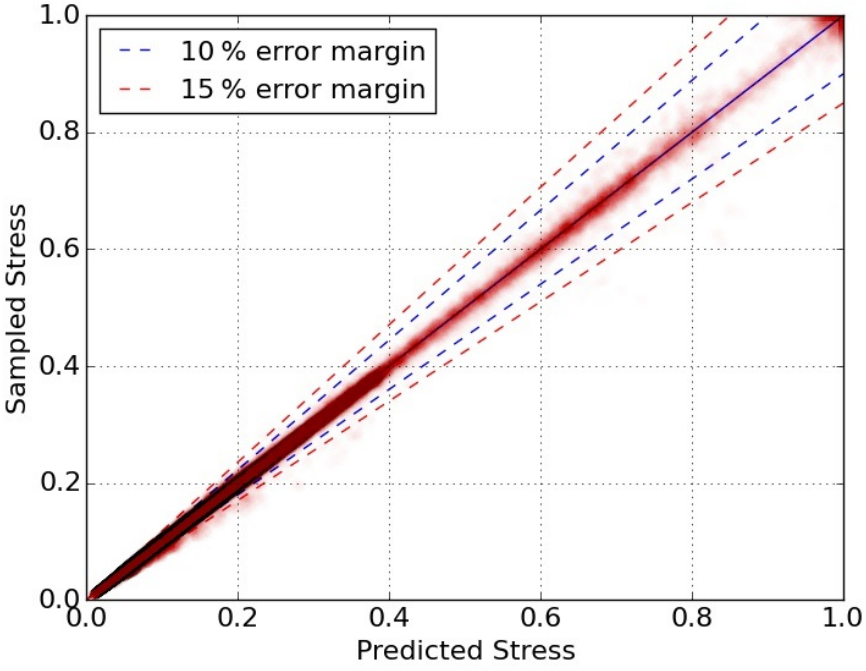

Figure D.5: Sampled vs predicted stress for load case M_z
R-squared based on testing set: 0.9984

Appendix E

Complete header box with basic equivalent material model - Additional comparison plots

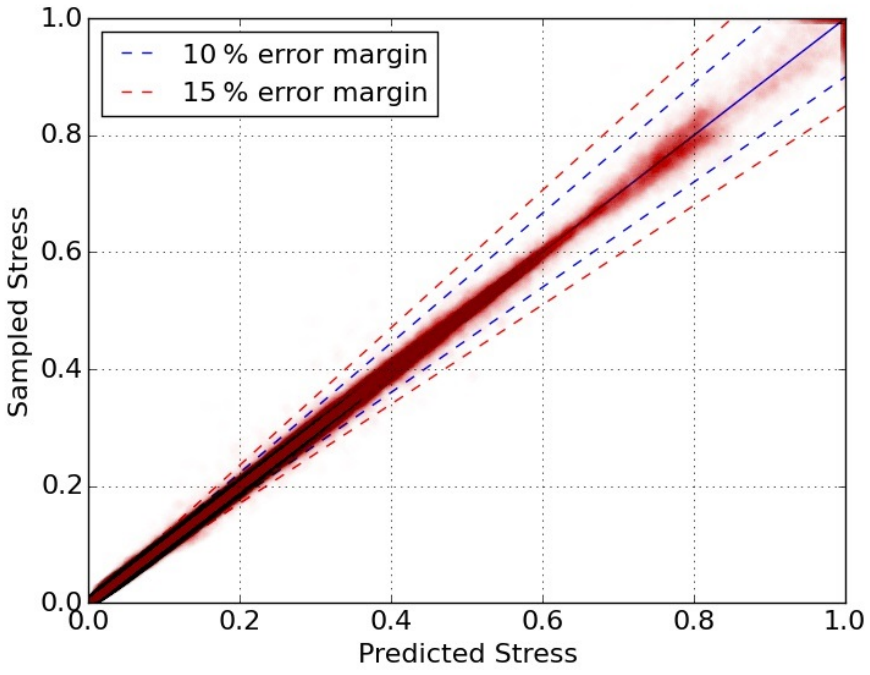

Figure E.1: Sampled vs predicted stress for load case F_x
R-squared based on testing set: 0.9986

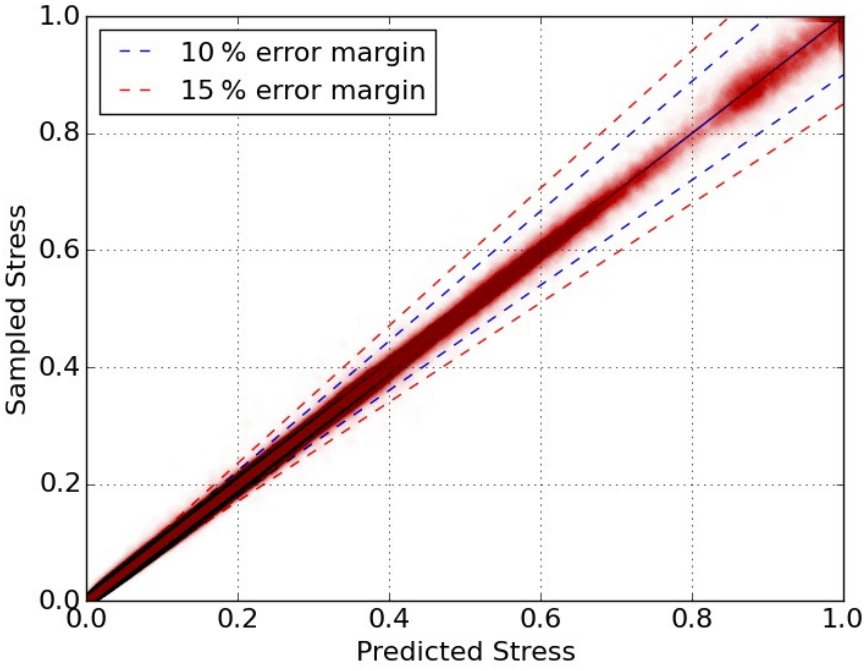

Figure E.2: Sampled vs predicted stress for load case F_z
R-squared based on testing set: 0.9990

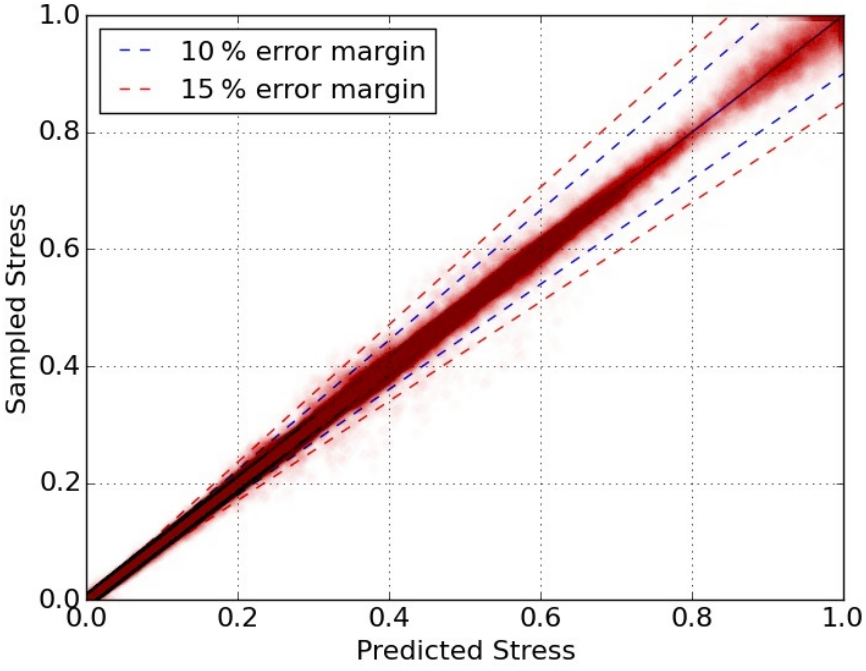

Figure E.3: Sampled vs predicted stress for load case M_x
R-squared based on testing set: 0.9986

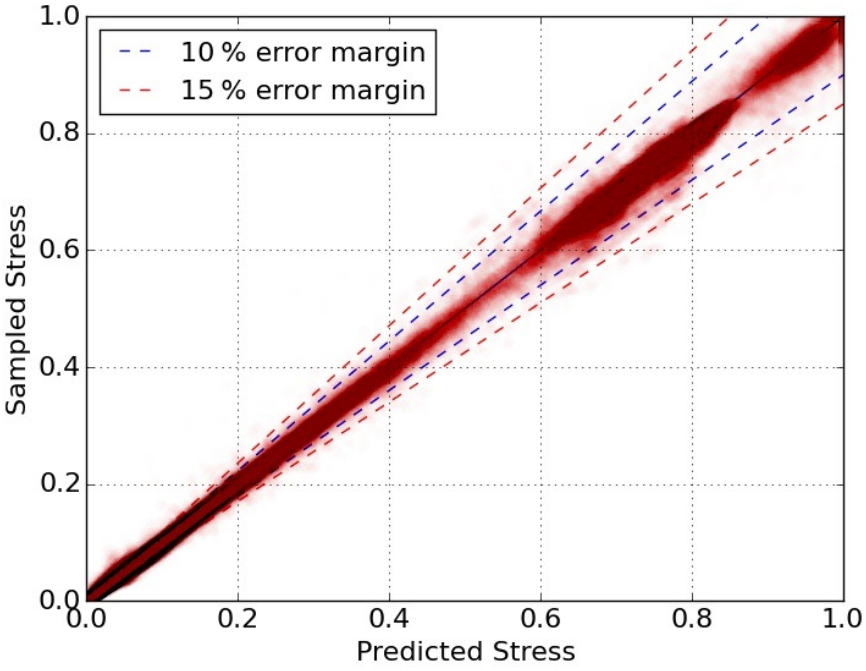

Figure E.4: Sampled vs predicted stress for load case M_y
R-squared based on testing set: 0.9989

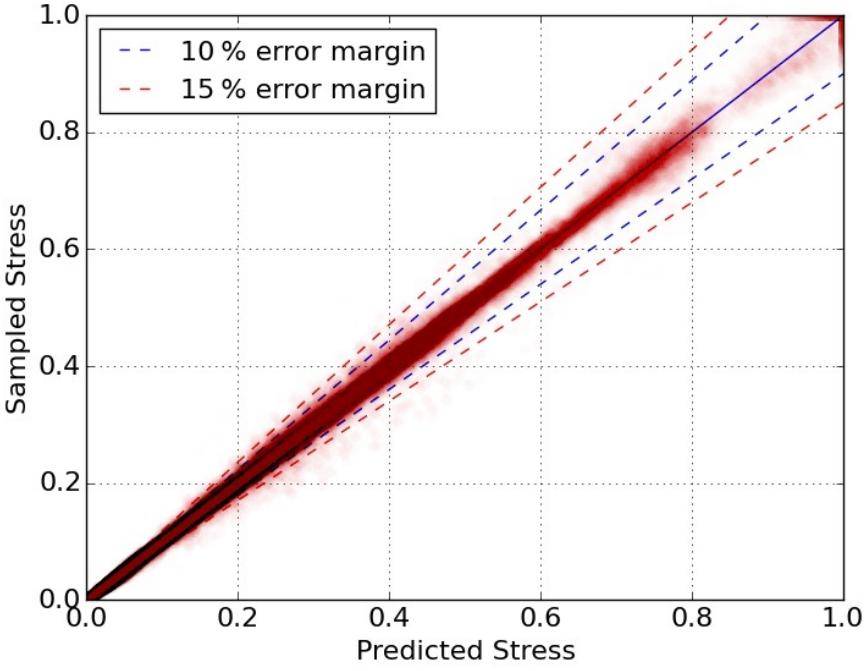

Figure E.5: Sampled vs predicted stress for load case M_z
R-squared based on testing set: 0.9983

Appendix F

Complete header box model - Additional comparison plots

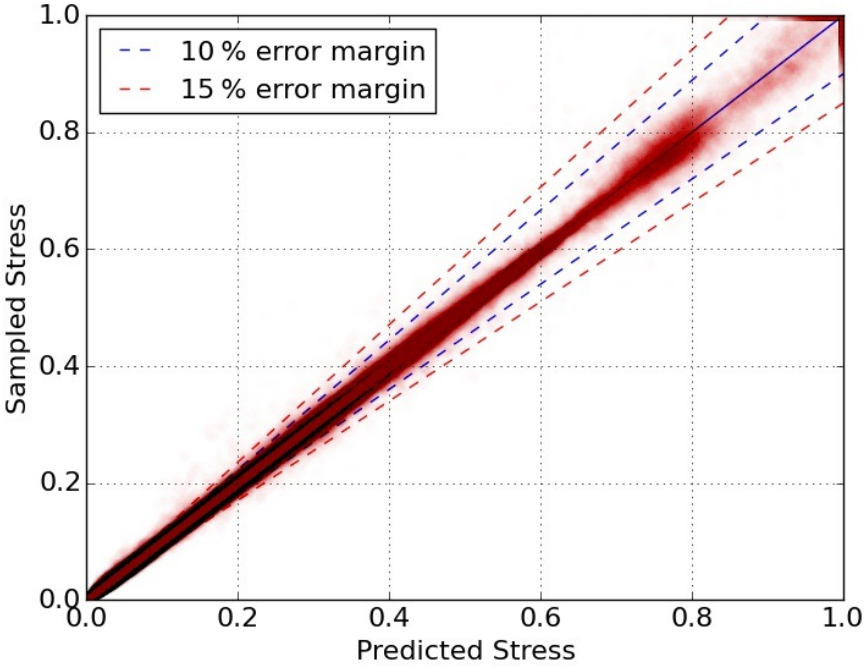

Figure F.1: Sampled vs predicted stress for load case F_x
R-squared based on testing set: 0.9984

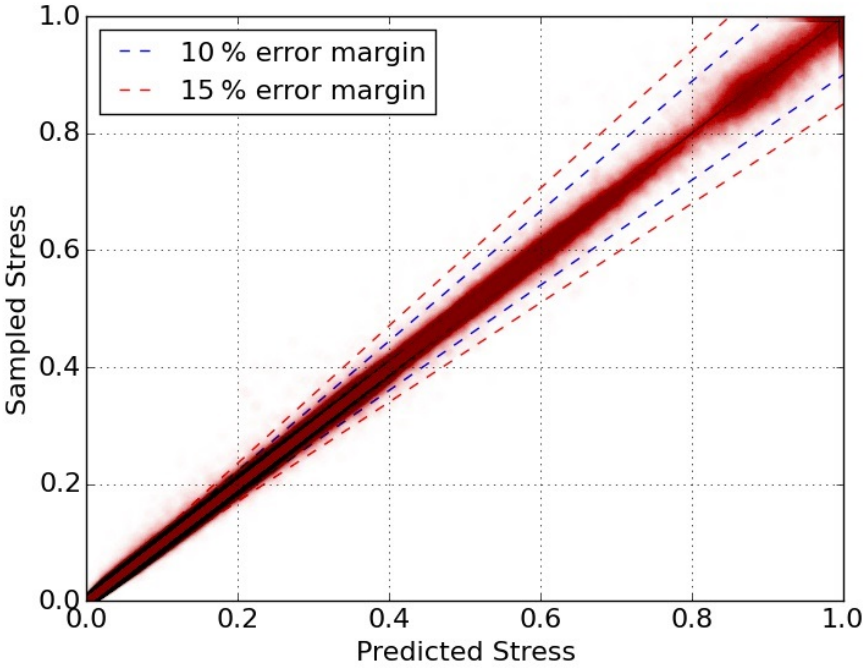

Figure F.2: Sampled vs predicted stress for load case F_z
R-squared based on testing set: 0.9989

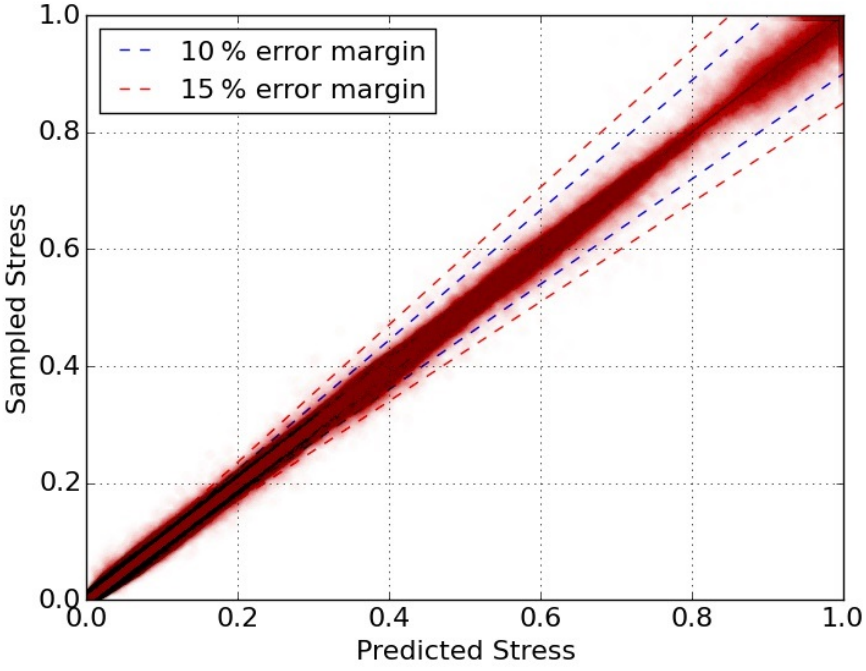

Figure F.3: Sampled vs predicted stress for load case M_x
R-squared based on testing set: 0.9986

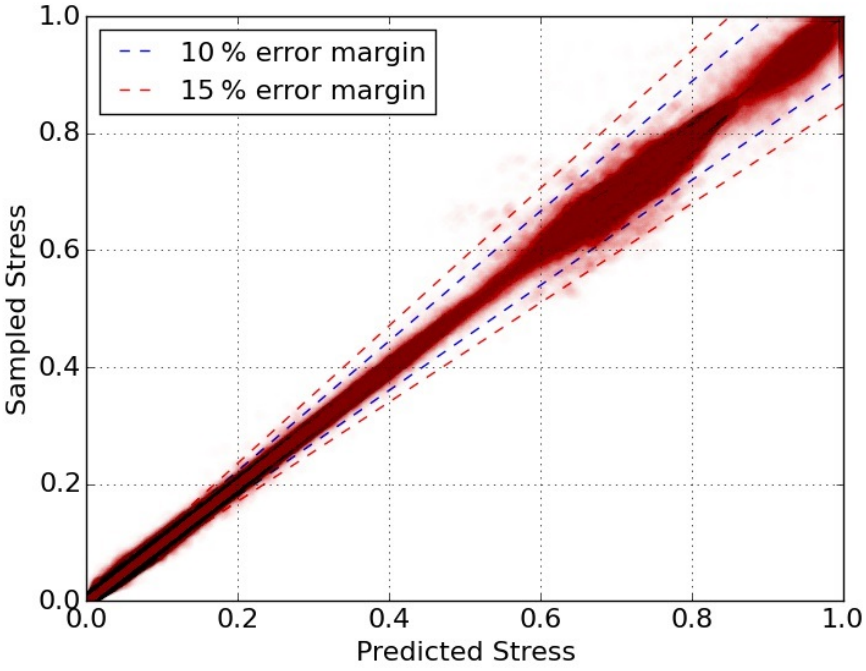

Figure F.4: Sampled vs predicted stress for load case M_y
R-squared based on testing set: 0.9989

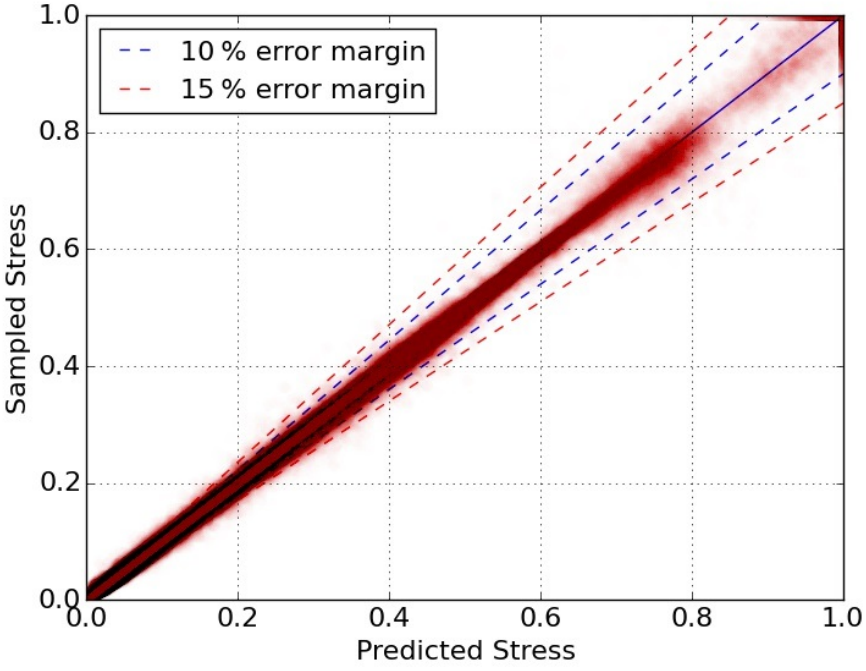

Figure F.5: Sampled vs predicted stress for load case M_z
R-squared based on testing set: 0.9982

Appendix G

Partial header box with basic equivalent material - Additional results plots

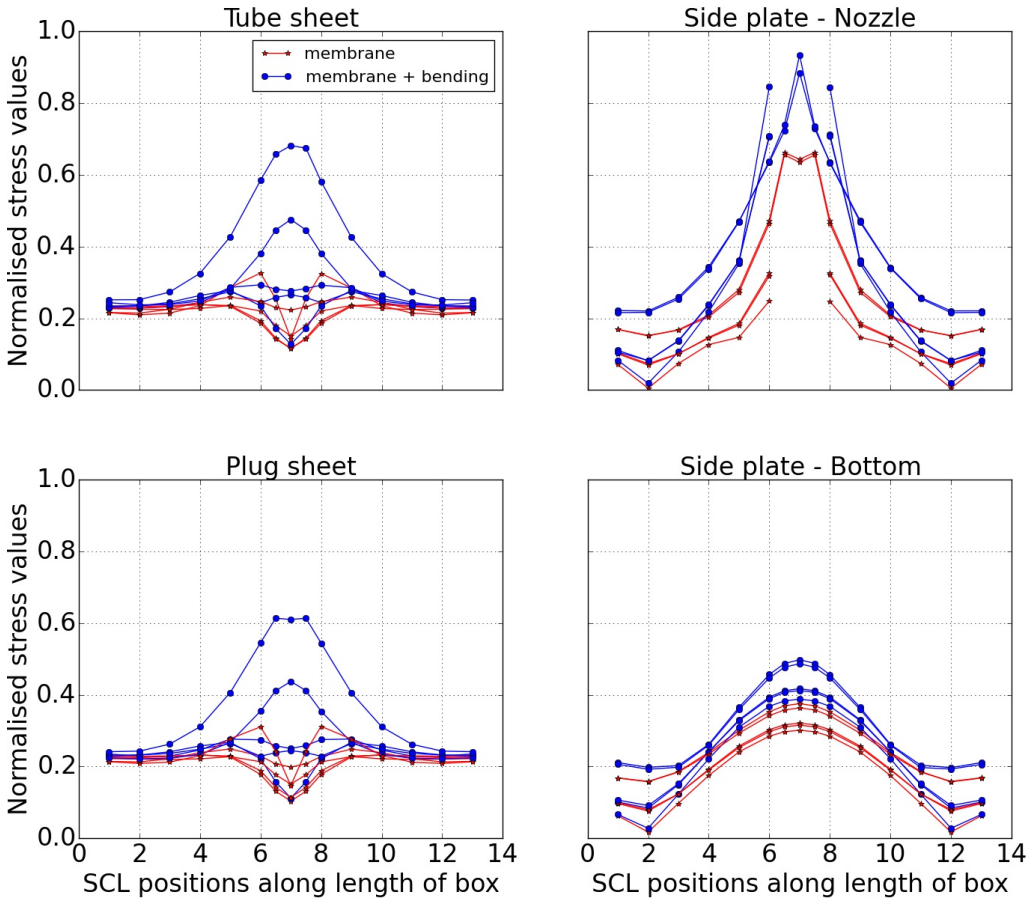

Figure G.1: Example results predicted by meta-model for load case F_y

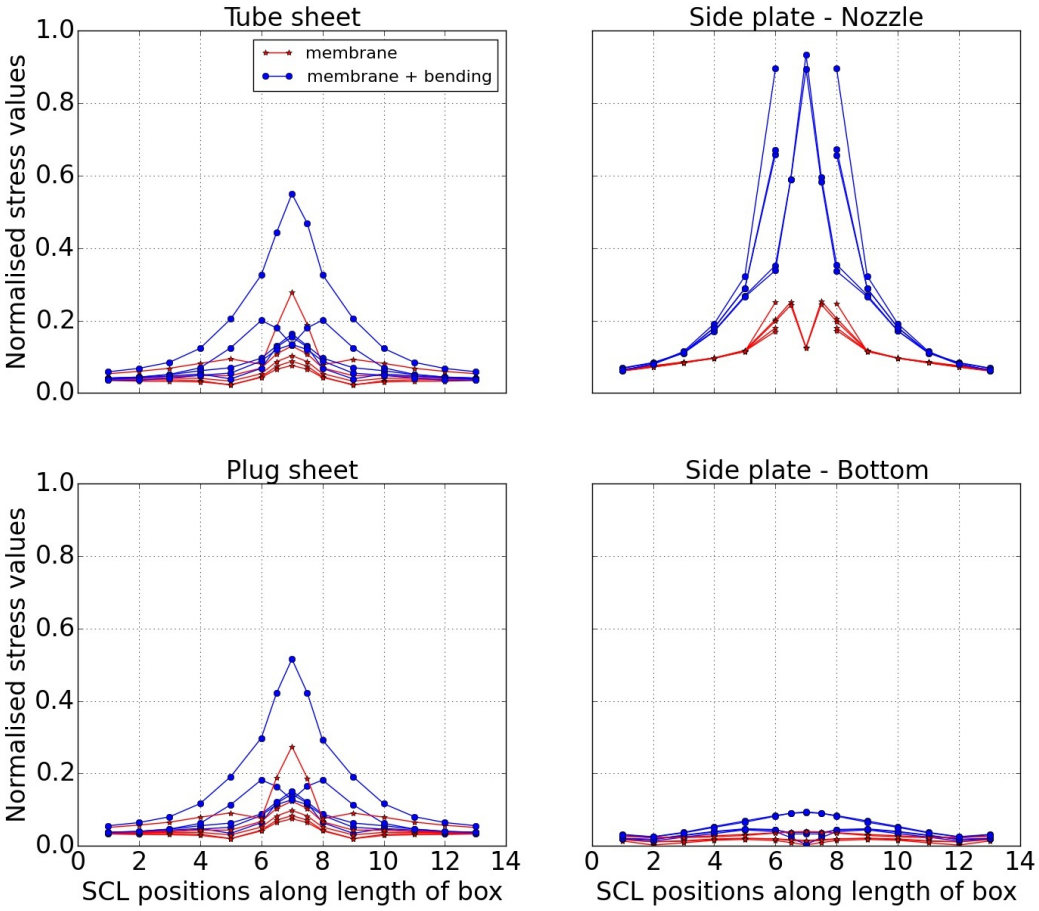

Figure G.2: Example results predicted by meta-model for load case F_z

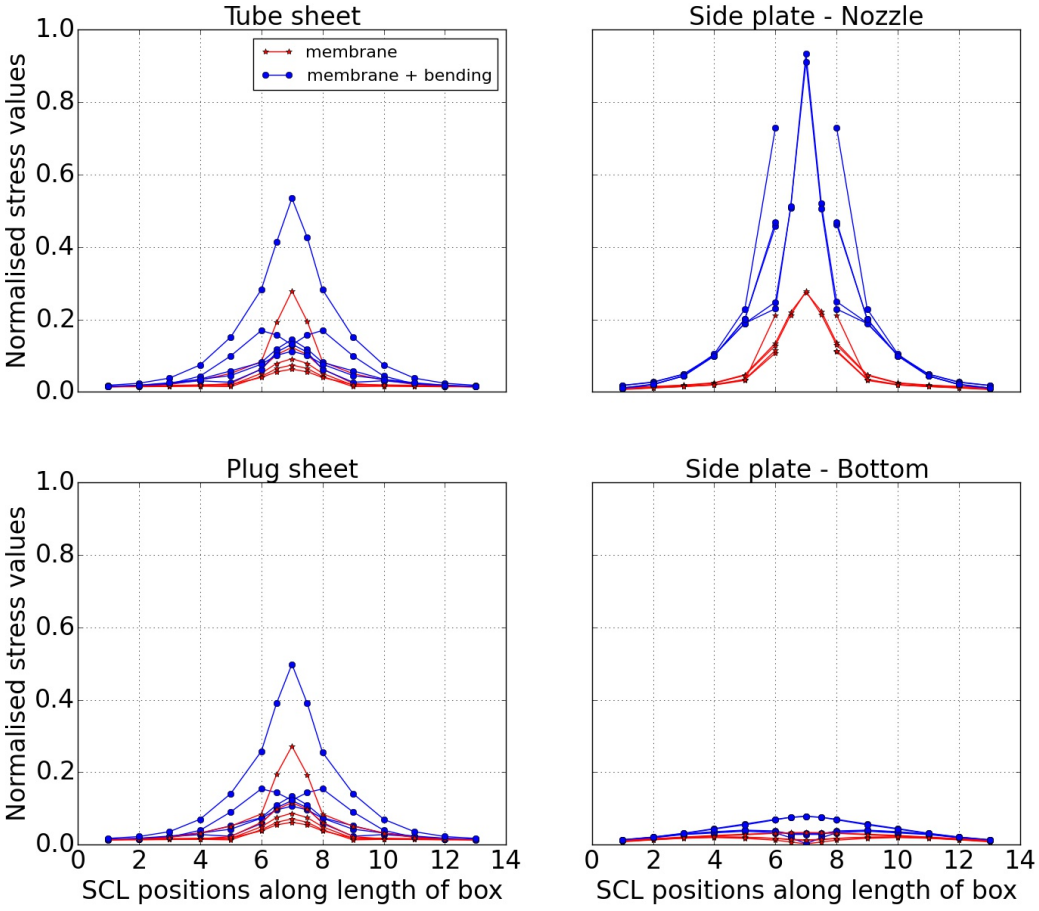

Figure G.3: Example results predicted by meta-model for load case M_x

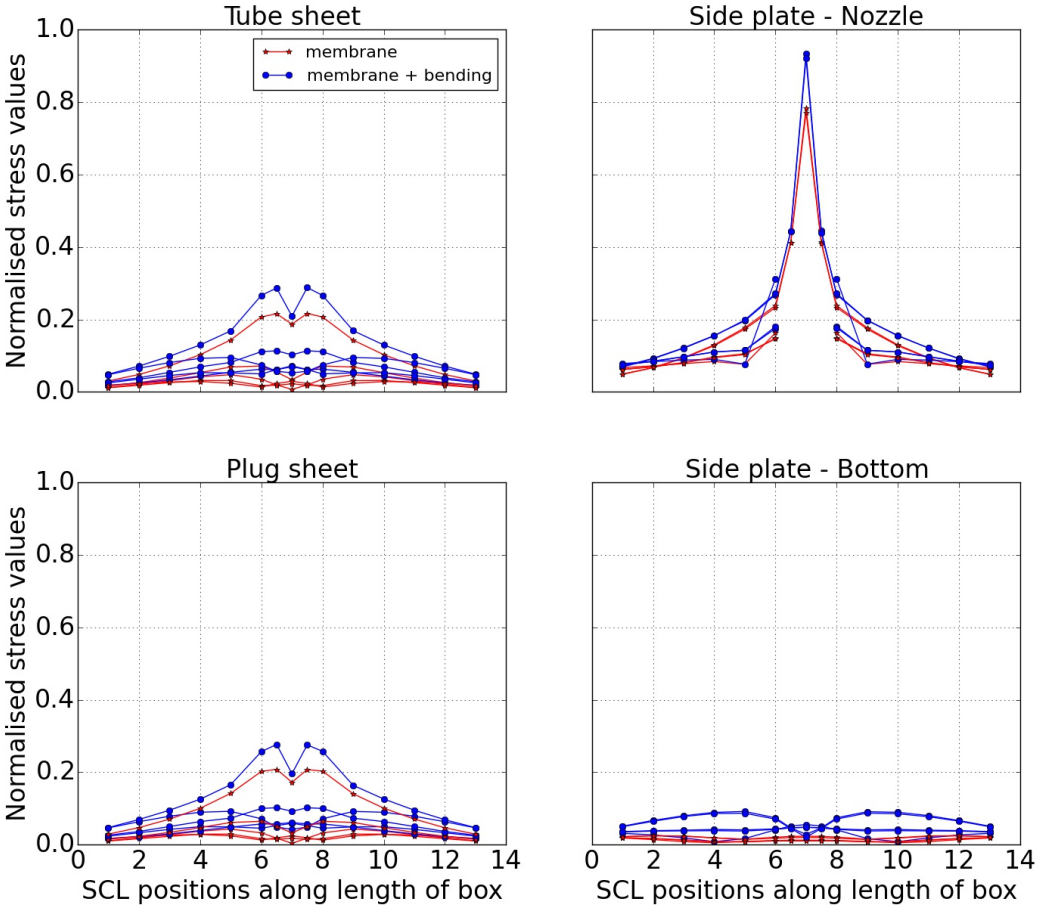

Figure G.4: Example results predicted by meta-model for load case M_y

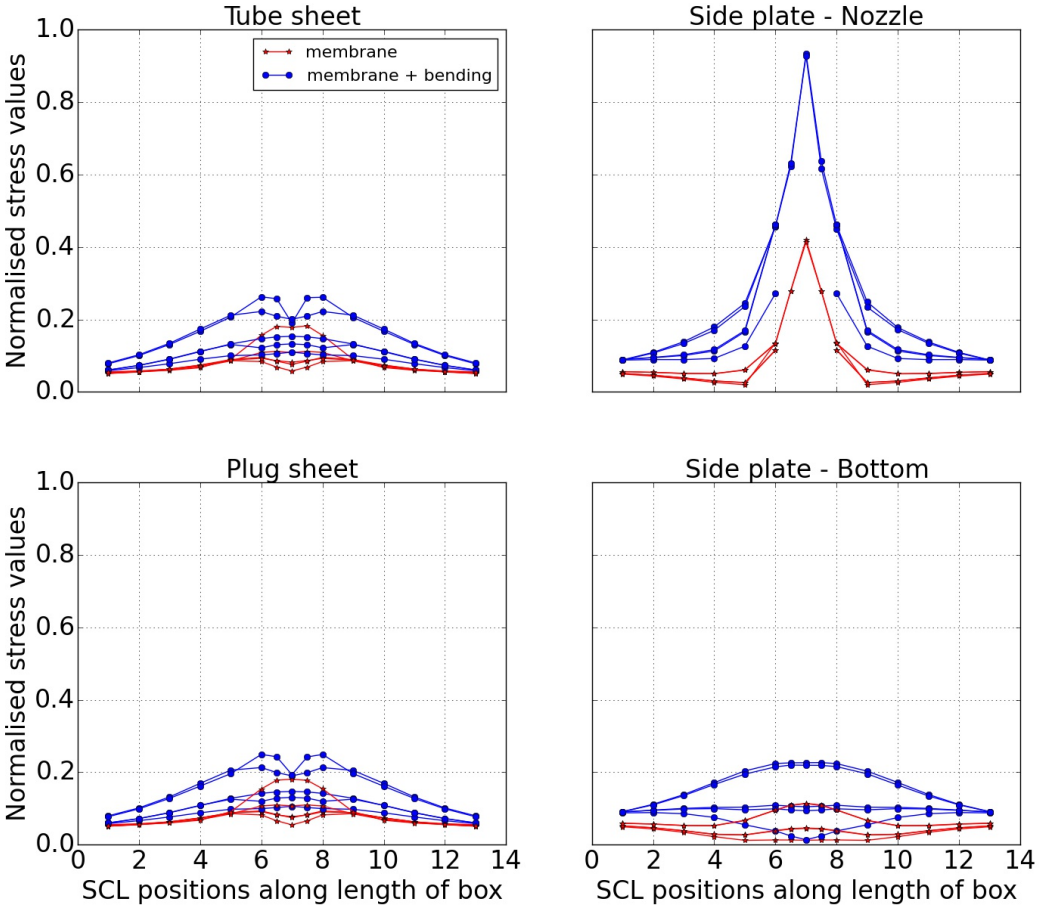

Figure G.5: Example results predicted by meta-model for load case M_z

List of References

Abu-Mostafa, Y.S. (2012). Learning From Data.
Available at: `http://work.caltech.edu/slides/slides13.pdf` (date accessed 08/23/2017).

Ackers, M.S. (2012). *Performance and Thermo-Mechanical Thermo Mechanical Cost Evaluation of API 661 Air-Cooled Air Cooled Heat Exchangers*. Masters Thesis, Stellenbosch University.

API (2013). Air-Cooled Heat Exchangers for General Refinery Service petrochemical and natural gas industries. Tech. Rep., American Petroleum Institute.

ASME (2015). Rules for Construction of Pressure Vessels. In: *ASME Boiler & Pressure Vesssel Code*. The American Society of Mechanical Engineers, New York.

ASME (2017). Rules for Construction of Pressure Vessels. In: *ASME Boiler & Pressure Vesssel Code*. The American Society of Mechanical Engineers.

Becker, J.W. (2013). INVESTIGATION INTO THE BENEFITS OF USING ASME BPVC SECTION VIII DIVISION 2 IN LIEU OF DIVISION 1 FOR PRESSURE VESSEL DESIGN. In: *ASME District F - Early Career Technical Conference*, vol. 12, pp. 223–256. ASME, Birmingham, Alabama.

Beyers, W.A., Zapke, A. and Venter, G. (2015). Improved Cover Type Header Box Design Procedure. *R & D Journal of the South African Institution of Mechanical Engineering*, vol. 31, no. 1, pp. 76–85.

Bohling, G. (2005). Resources for C&PE940, Data Analysis in Engineering and Natural Science.
Available at: `http://people.ku.edu/~gbohling/cpe940` (date accessed 08/23/2017).

Broomhead, D. and Lowe, D. (1988). Multivariable Functional Interpolation and Adaptive Networks. *Complex Systems*, vol. 2, no. 3, pp. 321–355.

Cavazzuti, M. (2013). *Optimization Methods: From Theory to Design*. Springer, Berlin; New York. ISBN 9783642311864.

Centre for High Performance Computing (2017). Lengau High Performance Computer.
Available at: `https://www.chpc.ac.za/index.php/resources/lengau-cluster` (date accessed 08/23/2017).

Golub, G. and Reinsch, C. (1970). Singular Value Decomposition and Least Squares Solutions. *Numer. Math.*, , no. 14, pp. 403–420.

Gutierrez-Osuna, R. (2015). Intelligent sensor systems - Validation. Available at: `http://research.cs.tamu.edu/prism/lectures/iss/iss_l13.pdf` (date accessed 08/23/2017).

Harvey, D. (2013). Image and Video Exchange. Available at: `http://community.asdlib.org/imageandvideoexchangeforum/` (date accessed 08/23/2017).

Hung, Y. (2013). Optimal Experiment Design, Latin Hypercube. In: Dubitzky, W., Wolkenhauer, O., Cho, K. and Yokota, H. (eds.), *Encyclopedia of Systems Biology*, pp. 1583–1585. Springer, New York.

Kassner, M. (2011). Insight: OpenSource Gaze Tracking. Available at: `http://fab.cba.mit.edu/classes/MIT/864.11/people/Moritz_Kassner/insight.html` (date accessed 08/23/2017).

Lin, J.G. (2006). MODELING TEST RESPONSES BY MULTIVARIABLE POLYNOMIALS OF HIGHER DEGREES. *Society for Industrial and Applied Mathematics Journal of Scientific Computing*, vol. 28, no. 3, pp. 832–867.

Martin, J.D. and Simpson, T.W. (2004). ON THE USE OF KRIGING MODELS TO APPROXIMATE DETERMINISTIC. In: *International Design Engineering Technical Conferences and Computers and Information in Engineering Conference*. ASME, Salt Lake City.

McKay, M., Beckman, R. and Conover, W. (1979). A comparison of three methods for selecting values of input variables in the analysis of output from a computer code. *Technometrics*, vol. 21, no. 2, pp. 239–245.

Myers, R., Montgomery, D. and Anderson-Cook, C. (2009). *Response Surface Methodology*. Wiley & Sons, Hoboken.

Nel, H.-J., Nurick, A., Nel, A.L. and Lombaard, F. (2012). DESIGN OF UNPARTITIONED, PLUG TYPE HEADER BOXES FOR AIR-COOLED HEAT EXCHANGERS IN REFINERY SERVICE. In: *Proceedings of the ASME 2012 Pressure Vessels & Piping Conference*. Toronto.

Prinsloo, L. (2011). *A critical evaluation of the design of removable cover-plate header boxes for air-cooled heat exchangers*. Masters Thesis, University of Pretoria.

Siemens (2017). Siemens NX 10.0. Available at: `https://support.industrysoftware.automation.siemens.com/general/nx.shtml` (date accessed 08/23/2017).

Simpson, T., Mauery, T., Korte, J. and Mistree, F. (2001). Kriging Models for Global Approximation in Simulation-Based. *American Institute of Aeronautics and Astronautics*, vol. 39, no. 12, pp. 2233–2241.

South African Board of Standards (2012). SANS 347 : 2012 SOUTH AFRICAN NATIONAL STANDARD Categorization and conformity assessment criteria for all pressure equipment.

South African Dept of Labour (1993). Occupational Health and Safety Act.

Tubetech GmbH (n.d.). Air-cooled heat exchangers. Available at: `http://www.tubetech.de/sites_en/expert_aircooledhe_en.html` (date accessed 08/23/2017).

University of Stellenbosch (2017). Rhasatsha High Performance Computer. Available at: `http://www.sun.ac.za/hpc` (date accessed 08/23/2017).

Vapnik, V.N. (1995). *The Nature of Statistical Learning Theory*. Springer, New York.

Viana, F.A. (2013). Things you wanted to know about the Latin hypercube design and were afraid to ask. In: *10th World Congress on Structural and Multidisciplinary Optimization*. Orlando.

Wise, J.N. (2008). *Optimization of a Low Speed Wind Turbine using Support Vector Regression*. Masters Thesis, Stellenbosch University.

Zeng, Z.J., Guo, Y.Z. and Gao, J.J. (1990). A new mechanical model for rectangular structures subjected to internal pressure. *International Journal of Pressure Vessels and Piping*, vol. 42, no. 2, pp. 237–246. ISSN 03080161.